Title
Plasmonic Nanoantennae for Single-molecule Sensing and Gene Regulation

Author
FU, CHI-CHENG

Publication Date
2012

Peer reviewed|Thesis/dissertation

Plasmonic Nanoantennae for Single-molecule Sensing and Gene Regulation

by

Chi-cheng Fu

A dissertation submitted in partial satisfaction of the
requirements for the degree of
Joint Doctor of Philosophy
with the University of California, San Francisco
in
Bioengineering
in the
Graduated Division
of the
University of California, Berkeley

Committee in charge:
Professor Luke P. Lee, Chair
Professor Randall Lee
Professor Ming C. Wu

Fall 2012

Abstract

Plasmonic Nanoantennae for Single-molecule Sensing and Gene Regulation

by
Chi-cheng Fu

Joint Doctor of Philosophy in Bioengineering
with University of California, San Francisco

University of California, Berkeley

Professor Luke P. Lee, Chair

Biophotonics denotes the utilization of light to study biology and has provided many new tools and insights for life science. For example, molecular imaging by light microscopes with fluorescent probes has gained considerable attention owing to its high sensitivity and multiplexing capabilities. Optical tweezers employing focused laser beams can individually trap micrometer-sized objects and measure biomolecular interactions. Optogenetics has demonstrated photonic control of genetically modified cells and opened up new avenues for manipulating biological events in live cells and animals. Although conventional biophotonic techniques often satisfy the requirements of cell biologists, the diffraction of light inevitably restricts their applicability to single biomolecules (e.g. proteins, DNA, and RNA) with characteristic sizes on the nanometer scale. Based on the localized surface plasmon resonance, plasmonic nanoantennae-mediated molecular sensing, manipulation and fabrication offer a promising way to overcome the diffraction limit of light by leveraging highly confined and strong electromagnetic hot-spots. Creatively utilizing interactions between hot-spots, biomolecules, cells and materials generates novel biological applications both *in vitro* and *in vivo*.

Here, I first present a method, named nanoplasmonic optoporation, for precise gene regulation by the creation of transient nanopores in cell membranes. Induced by the irradiation of near-infrared light, the enhanced surface plasmon resonance of gold particles allows us to photothermally create ~40 nm nanopores with a ~30 min lifetime. Sequential molecular delivery into somatic cells is demonstrated with single-cell precision, as well as at the larger centimeter-scale of conventional cell culture. Nanoplasmonic-mediated gene regulation in stem cells is demonstrated with higher efficiency than conventional transfection methods.

Second, graphene nanopores are created and integrated with an optical antenna with a single fabrication step, light-induced gold nanorods melting. Nanometer-sized heating source created by photothermal effect of gold nanorods resting on a graphene membrane created nanoscale pores with hemispherically shaped nanoantennas. The approach yields the significant advantage of parallel nanopore fabrication compared to the conventional sequential process using an electron beam. The atomically-thin nature of graphene, together with nanoplasmonic properties of integrated antennas, makes this unique nanopore a potential platform for high resolution and

high throughput nucleic acid analysis in single-molecular level. The optical function of an integrated plasmonic nanoantenna is demonstrated by multifold fluorescent signal enhancement during the translocation of single DNA molecules through a graphene nanopore. Graphene nanopores integrated with optical antennae could offer a new avenue for simultaneous electrical and optical enhanced DNA sequencing in the future.

Third, a simple, high-sensitive, and robust method for the detection of microRNA cancer markers has been demonstrated by oligonucleotide-conjugated plasmonic nanoparticles. Due to surface plasmon resonance effects, single metallic nanoparticles provide an extremely strong light scattering signal that lowered the detection threshold and improved sensitivity for the detection of single microRNAs. In addition, dimer-type probes were designed to induce red-shift in their scattering when hybridized with target microRNAs. It is possible to achieve single-molecular detection by simply counting red-shifted nanoparticles. To further apply this method for point-of-care diagnosis, a portable total internal reflection illumination system was designed and integrated with nanoplasmonic-based sensors.

In the end of this thesis, I conclude with the outlook of nanoplasmonic integrated nanofluidics for medical diagnostics and *in vivo* nanoplasmonic manipulation of genetic circuits. Nanoplasmonic integrated nanopores are promising for the precise control of nano-scaled environments for DNA or RNA analysis. On the other hand, another source of excitement comes from applications of multiple plasmonic nanomaterial-controlled gene circuit engineering. Nanoplasmonic gene regulation mediated by photothermal effects might provide multiple manipulations with high spatial and temporal resolution. Studying nanoplasmonic-mediated sensing and delivery could provide new avenues for understanding how biological systems function at the molecular level.

Table of contents

CHAPTER 1

Introduction to Nanoplasmonic Biophotonics

1.1 Conventional Biophotonics versus Nanoplasmonic Biophotonics

In a broad sense, the term *biophotonics* denotes the utilization of light (photons) to study biology (Fig. 1.1a). Culminated in a research area that intersects biology, chemistry, physics and engineering, biophotonics has allowed many developments of optical science and technology to bring new insights into life sciences, for both fundamental and clinical interests. For instance, transmission light microscopy, combined with various contrast enhancement methods (e.g. phase contrast or differential interference contrast), is widely adopted for the observation of tissues, cells and organelles. Spectroscopy (e.g. absorption, luminescence, infrared or Raman spectroscopes) permits measurements of sample concentration and identification of material contents.[1] Fluorescent probes (e.g. organic dyes, quantum dots and fluorescent nanodiamonds) enabled molecular imaging and have gained considerable attention owing to their single molecular-level sensitivity and multiplexing capabilities.[2-6] Together with fluorescent protein reporters, fluorescence microscopy and high-throughput fluorescence-activated cell sorting techniques now routinely perform real-time monitoring of gene expression and regulation in single cells.[2,7] Other than for the purpose of biological materials characterization, the term *biophotonics* can also refer to optical techniques that physically or genetically control specimens. In fact, since the first demonstration of laser in the 1960s , progress in laser development not only touched our lives through improved microscopy or spectroscopy techniques, but also by allowing unprecedented manipulation and actuation of materials of a diverse range. Just to name a few, photodynamic therapy is now widely used to guide and activate chemical compounds for drug release.[8] Additionally, optical tweezers employing highly focused laser beams can individually trap micrometer-sized objects.[9] Such actuator also makes possible the measurements of force generated by biomolecular interactions in piconewton-scale for studying single-molecule biophysics. More recently, optogenetic control was shown to allow manipulation through guided light.[10,11] It opened up new venues for handling of biological events in live cells. One common theme for both light-enabled imaging and actuation is that the photonic system in question must allow for light collection and manipulation within the length and time scale of biological interest.

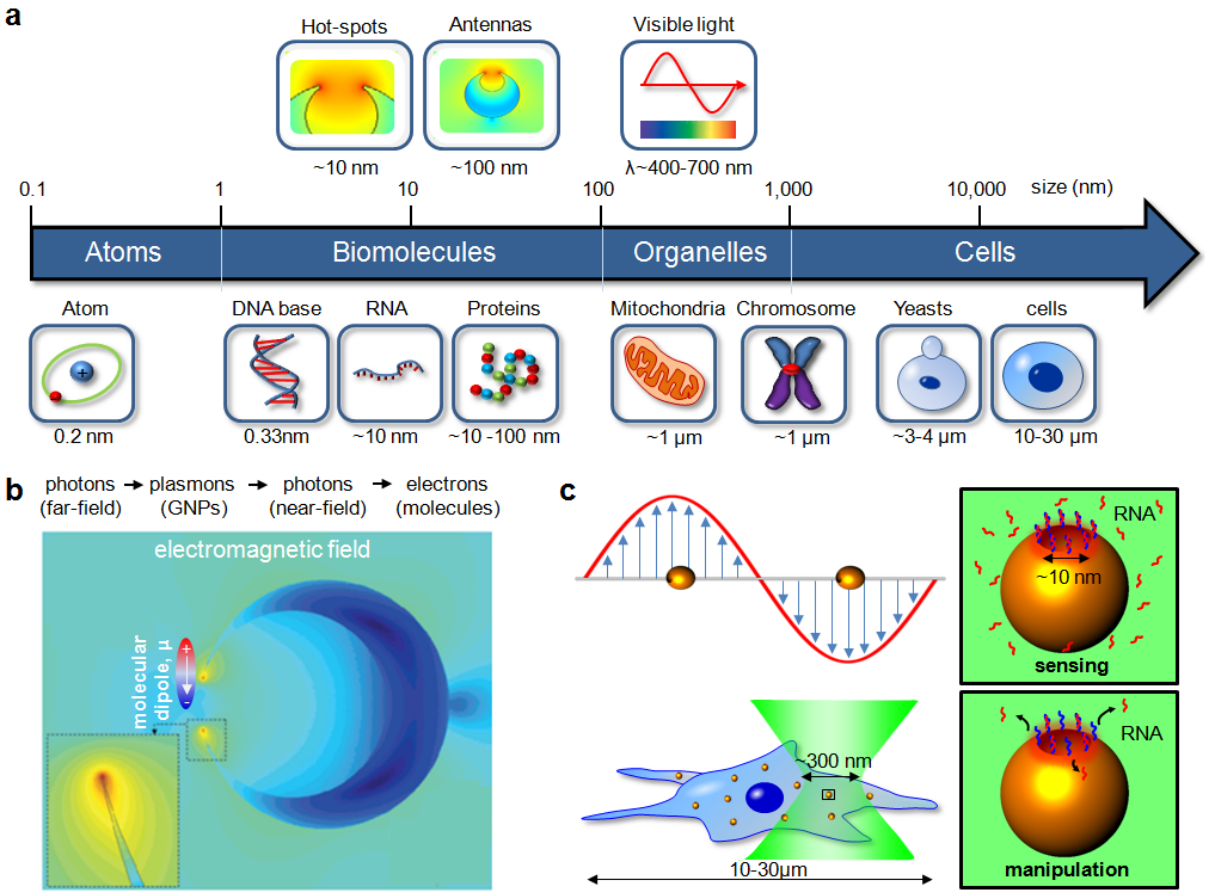

Figure 1.1 Nanoplasmonic biophotonics for biomolecular sensing and manipulation. **a,** Relative scale of cells, biomolecules, wavelength of light and plasmonic hot-spots. Note that the wavelength of visible light is 1-2 orders of magnitude larger than biomolecules and hot-spots. **b,** Schematic illustration of localized surface plasmon resonance on gold nanocrescent, enhancing a electromagnetic field of incident light. The bottom-left inset has shown the hot-spot on the tip of the nanocrescent.[12,13] **c,** The top-left inset shows the relative scale of nanoantennas versus wavelength of light. In bottom inset, light-absorbed plasmonic nanoantennas (e.g. gold nanocrescents, yellow dots) are promising probes and vectors for sensing and manipulating biomolecules (e.g. RNA) with nm-scaled resolution both *in vivo* and *in vitro*.[14-16]

However, in the quest of elucidating the inner workings of the essential constituents of life, a problem inevitably arises when seeking to probe smaller biological structures within the wavelength scale of the illumination light. A fundamental resolution limit, which is around half of the wavelength ($\lambda/2{\sim}300\ nm$) for visible light, sets a barrier on how optical energy can be focused. Although conventional biophotonic techniques often meet cell biologists' requirements, this diffraction limit of light fundamentally restricts the applicability of biophotonic tools to nanometer scale where reside active key biological ingredients such as proteins, binding molecules and genetic materials (DNA and RNA) (Fig. 1.1a). Without a mean to reach the

subwavelength scale, progress in biological science and technology is impeded by the traditional biophotonic techniques.

Few attempts have been tried to address this issue, with the development of nano-optic measurement techniques such as the scanning near-field microscopy and the super-resolution microscopy.[17-19] While these novel nanotools have broken the diffraction limit in terms of imaging capability, their use of sophisticated bulky optical systems might not always be suitable for molecular or cellular biological studies, especially *in vivo*. For examination and manipulation at the molecular level, a more suitable alternative for biology is *nanoplasmonics*, through the techniques that rely on subwavelength optical fields enhanced by collective charge oscillation (or plasmons) of a metal nanostructure (or a nanoantenna, Fig. 1.1a).[14-16] Nanoplasmonic devices based on the localized surface plasmon resonance (LSPR) offer a promising way to overcome the diffraction limit of light at the same time generate novel *in vitro* and *in vivo* biological applications.[14,20-23] *Nanoplasmonic Biophotonics* is therefore this emerging biophotonic area that seeks to develop optical techniques to probe and manipulate biological matter based on a new paradigm, which creatively uses tightly focused subwavelength optical energy found at the vicinity of metallic nanostructures.

Shaped through bottom-up chemical synthesis or top-down lithographic fabrication, plasmonic antennas generate highly confined electromagnetic near-fields patterns (hot-spots).[14] These hot-spots have characteristic size in the tens of nanometers, useful for biological molecules of comparable size (e.g. DNA, RNA and proteins). In fundamental terms, the synergy between a light harvesting plasmonic photonic device and a target biomolecule of interest can be broken down as follows (Fig. 1.1b): (1) far-field photons scatter around nanostructures and result in near-field electromagnetic patterns; (2) the collective oscillation of electrons from metals (plasmons) are means to increase the local density of photons; (3) the increased number of near-field photons, in turn, permeate biomolecules and interact with them through their electronic polarization (i.e. the strongest being the molecular dipole).[24,25] As is reviewed in this text, creatively utilizing plasmon-tailored optical energy while interacting with biomolecules has shed many new insights in both biology and optics owning to its promises at probing, imaging and manipulation of single and individual biomolecules, both *in vitro* and *in vivo* (Fig. 1.1c).[14,20,21,23,26]

The goal in this chapter is to describe the fundamentals and applications of nanoplasmonics as related to the fields of biology and medicine. We will start with a review of the fundamentals of nanoplasmonics by examining the optical properties of metallic nanoparticles. An explanation of how to tune the LSPR of nanoparticles through their size, shape and coupling strategies to match the absorption of target molecules will be given. A solid understanding of the foundations will better equip the reader with the knowledge required in the face of emerging nanofabrication techniques and computer simulation methods, useful to produce novel structures that leverage the unique photophysical properties of nanoscale metallic structures.

The applications will be organized by the way plasmon resonance is used. First, LSPR-based detections can be sensitivity to local environment. For example, based on the refrative-index induced LSPR-shift, nanoplasmonic molecular rulers have been used to study the process of

DNA hydrolysis by monitoring the length of conjugated DNA molecules around single nanoantennas.[27,28] In plasmon resonance energy transfer (PRET) method, a transfer of plasmonic energy from nanoantennas to surrounding biomolecular acceptors allows scientists to probe molecular absorption spectra in nanometer scale both *in vitro* and *in vivo*. [29-32]

Second, nanoplasmonic applications can be based on local enhancement of physicochemical properties. Hot-spots-mediated surface enhancements have gained considerable attention in recent years because they are able to lower the detection thresholds and also improve temporal resolution. For instance, metal enhanced fluorescence (MEF), based on strong coupling between antennas and fluorophores, have been applied to reduce fluorescence excited state lifetimes (i.e. increase emission rate) and simultaneously increase fluorescence emission intensities.[33-37] Another popular surface enhanced technique is based on surface-enhanced Raman scattering (SERS). This method offers more than ten orders of magnitude of enhancement, allowing Raman scattering from single molecules to be detected.[26,38-46] Both MEF and SERS are widely applicable to biomedical diagnoses and imaging both *in vitro* and *in vivo*.

Last but not least, nanoplasmonic antennas have also recently been shown to act like sub-wavelength energy harvesters through light-to-heat (photothermal effect) and light-to-force (nanoplasmonic trapping) conversion. This has promise to facilitate many biological manipulation by precisely delivering molecules through the guide of light. As a possible application, DNA and RNA molecules, conjugated with plasmonic nanoantennas, can be release to regulate gene expression in live cells via localized photothermal effect.[22,25,47-49] Similarly, localized strong hot-spots enable trapping of sub-wavelength materials. The diameter of confinement in nanoplasmonic trapping is approximately ten times smaller than that in conventional optical optics. Trapping of single biological particles and molecules in nanometer scale will be reviewed.[50-55]

1.2 Fundamentals of Nanoplasmonics

History of nanoplasmonic materials

The use of gold colloids in medicinal recipes dates back to at least the ancient China, Egypt and India (few millennia BC). Likewise, colloidal suspensions of gold-silver alloys in decorative pieces such as ceramics or stained glass were also found in the works of ancient Chinese, Roman, or Medieval artisans.[56,57] Figure 1.2 shows a few examples of metal colloids in old time ceramics, medieval stained glass and Faraday's microscope slides. Whether for their potential as a therapeutic agent or vivid optical properties discernible to the naked eye, gold nanoparticles have long been an object of fascination from our antecedents to our contemporaries. Obviously, the ancient doctors and glassmakers did not have much knowledge of electrodynamics, surface chemistry nor nanofabrication infrastructure. Today, with the advent of nano-optics and nano-fabrication, we are at a better position to systematically examine the unique photophysical properties of metallic nanostructures, named nanoplasmonics.

Overview of the Electrodynamics of Nanoplasmonics

A *plasmon* is the basic unit of a collective charge oscillation (plasma) in a noble metal. The optical response of metal derives from the field contribution of a large amount of conduction electrons in oscillation under the external driving force of an illumination. The applications of *plasmonics* are inspired by the unique optical properties of metal structures that happen near a *plasmon resonance*, where free and bound electrons oscillate well with incident light. plasmon resonance happens in bulk and dot-like metallic particles. In *nanoplasmonics*, the attention is placed on the ability of subwavelength metallic nanostructures to collect and focus optical energy beyond the diffraction limit of light via the *localized surface plasmon resonance* (LSPR).[23] These metallic structures have a characteristic size a that is smaller than the wavelength λ of incident light.

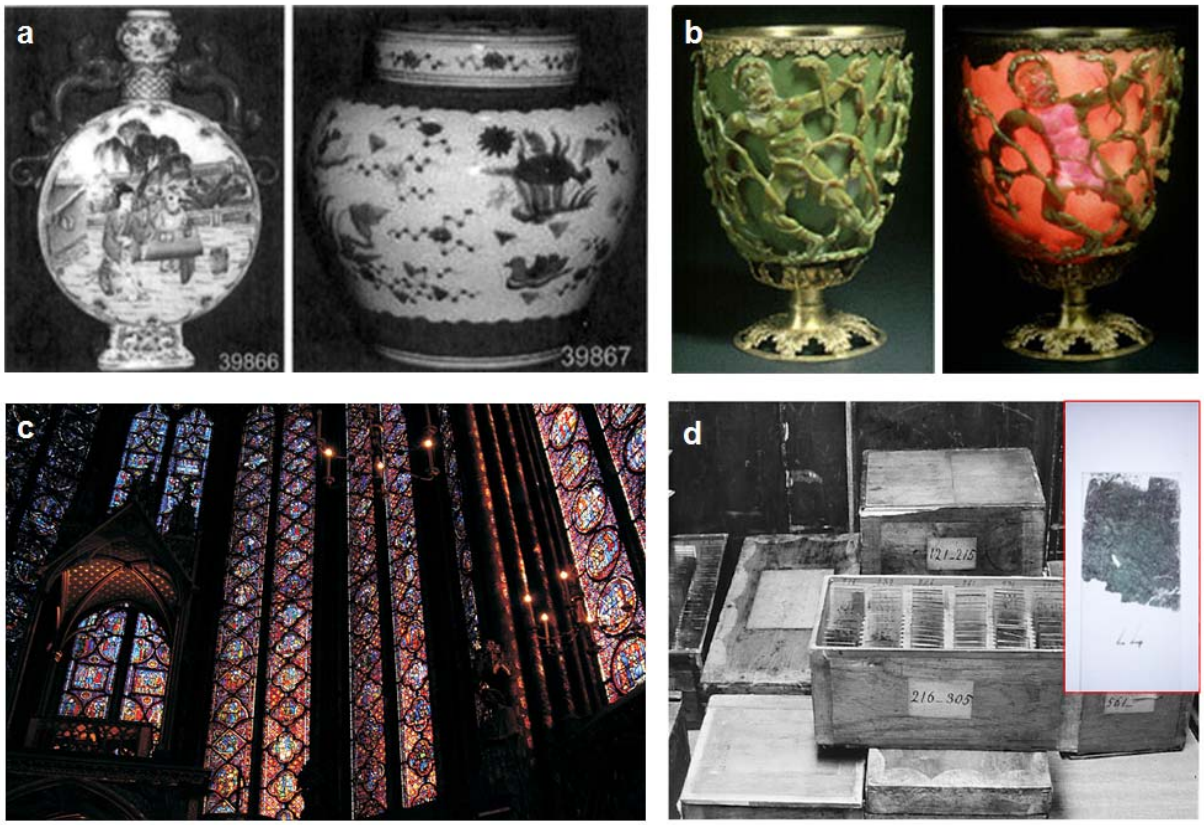

Figure 1.2 Examples of nanoplasmonic materials used by our antecedents.[56,57] **a,** Gold nanoparticles were used in the paint of some ancient Chinese ceramics to bring out bright and sharp reddish colors. **b,** The beautifully crafted Roman Lycurgus Cup, depicting the death of the king of Thracians from Homer's *Illiad,* displays striking shades of bright red and dark green. **c,** The stained glass in windows of medieval cathedrals such as la Sainte-Chapelle or Notre-Dame de Paris, contains gold and silver colloids. **d,** The collection of Michael Faraday's microscope slides is often referred as one of the first studies of gold colloids. The inset shows one of Faraday's slides partially coated with metal nanoparticles.

Conceptually, a nanoplasmonic structure is antenna-like: it converts the received optical energy to near-field and far-field counterparts.[58,59] Therefore, it has a big absorption and scattering cross-sections (Fig. 1.3a and 3b). The near-field represents the evanescent portion of the optical energy that tends to stay near the nanostructure (exponentially decays away from object boundary interfaces in the nanoscale lengths) whereas the far-field is the propagating part capable of traveling to a longer distance (propagation wave). A quantitative understanding of the relationship between light and metallic nanostructures is essential. The optical response of a nanoplasmonic probe is prescribed by size, shape and frequency dependent dielectric constant $\varepsilon(\omega)$ of material.[14,23,25,26] It translates the collective charge oscillation into polarizable electromagnetic field patterns. The Drude-Lorentz model is often introduced to describe such optical response of plasmonic materials to provide a first-order picture. In terms of applications, a stress is placed on the importance of being able to rationally design electromagnetic fields near a given nanoplasmonic structure. The starting point to quantitatively describe the electromagnetic field patterns is through the pedagogical Mie theory of light scattering of an arbitrary spherical particle. The rigorous Mie scattering gives a full vectorial analytical description of the multipolar electromagnetic field patterns dressing a sphere under illumination (Fig. 1.3c).[59] However, since the multipolar description of scattering is quite involved, a more intuitive quasi-static dipole approximation is often used as a quick analysis. This is often a good estimate for size of particles less than 10 nm, i.e. in the *Rayleigh limit*. For an arbitrary shape deviating from a Mie sphere, or a complex assembly of shapes involving strong interparticle coupling, a combination of numerical techniques are available and can be used to obtain a rigorous quantitative prescription for nanoplasmonic designs.

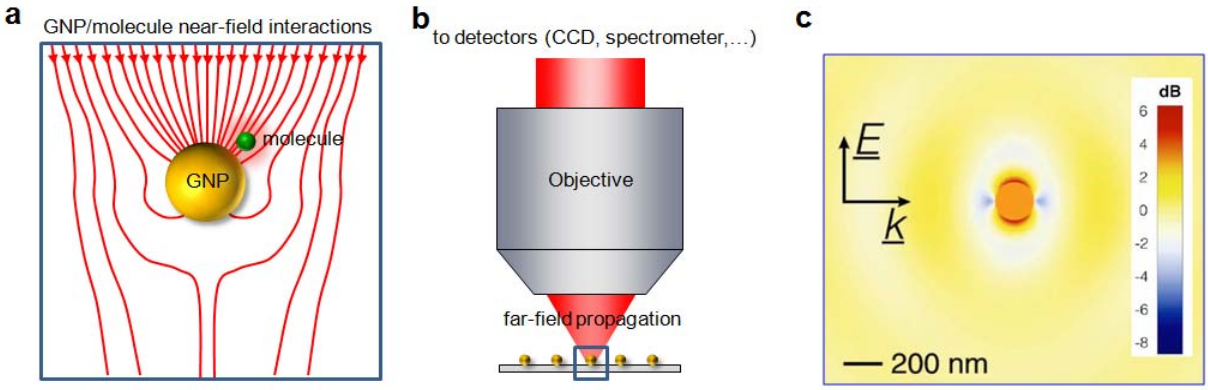

Figure 1.3 Fundamentals of nanoplasmonics.[59] **a,** Schematic illustration of localized surface plasmon resonance on gold nanoparticles (GNP, yellow dots), focusing a electromagnetic field (red line) and inducing nanolens effects. Optical properties of molecules (e.g. scattering and fluorescence emission) can be enhanced by near-field interactions with plasmonic nanoparticles. **b,** Schematic illustration of coupling near- field plasmonic nanoparticles /molecules interactions to far-field detection. **c,** Electric field amplitude surrounding a gold nanoparticle with an incident light based on Mie theory. Probing biomolecular interactions is localized by hot-spots of nanoplasmonic antennas.[58]

Dielectric Constant of Noble Metal

The frequency-dependent dielectric constant $\varepsilon(\omega)$ (or relative permittivity) describes the ability of a material to displace its electromagnetic field,

$$\boldsymbol{D}(\omega) = \varepsilon_0 \boldsymbol{E}(\omega) + \boldsymbol{P}(\omega) = \varepsilon_0 \varepsilon(\omega) \boldsymbol{E}(\omega)$$

where ε_0 is the vacuum permittivity, $\boldsymbol{E}$ and $\boldsymbol{D}$ denote respectively the electric and the displacement fields, and $\boldsymbol{P}$ is the polarization vector. The dielectric constant $\varepsilon(\omega) = \varepsilon_1(\omega) + i\varepsilon_2(\omega)$ is generally a complex function with a real part and imaginary part related to the amplitude and phase difference between the electric and its displaced fields.[25] It is used to characterize the propagation and attenuation of electromagnetic energy inside a medium (e.g. meal and water). Note that the well-known refractive index m of a material is related to relative permittivity ε and relative permeability μ through $m = \sqrt{\varepsilon\mu}$.

The optical response of a noble metal is determined by the dynamics between the incident field and the polarization of charged constituents inside the material.[25] Consider an incident electromagnetic wave that penetrates a metal with a skin depth δ. As a conductor, metals contain overlapping energy bands inside which a large number of free valence and bound interband electrons can easily move. This combined optical response of the free and bound electrons of a metal is described by a dielectric function $\varepsilon_M(\omega)$. As the incident electric plane wave $\boldsymbol{E}=\boldsymbol{E}_0 e^{-i\omega t}$ drives the electrons inside the metal to oscillate at a frequency ω, a time-varying electron displacement $\boldsymbol{r}=\boldsymbol{r}_0 e^{-i\omega t}$ causes local polarization via $\boldsymbol{P} = -ne\boldsymbol{r}$ with n and e denoting respectively the electron density and the fundamental charge unit. To a first-order approximation where the bound electrons are neglected, the optical response of bulk metal is described through a damped harmonic oscillator of the free electrons,

$$m_e \frac{\partial^2 \boldsymbol{r}}{\partial t^2} + m_e \Gamma \frac{\partial \boldsymbol{r}}{\partial t} = -e\boldsymbol{E}_0 e^{-i\omega t}$$

where m_e denotes the effective mass of an electron and Γ is the damping constant related to the rate of collisions of electrons. With oscillation occurring at the plasma frequency ω_P, the solution to the oscillator gives the Drude–Lorentz dielectric constant of metal,

$$\varepsilon_M(\omega) = 1 - \frac{\omega_P^2}{\omega^2 + i\Gamma\omega} = 1 - \frac{\omega_P^2}{\omega^2 + \Gamma^2} + i\frac{\Gamma\omega_P^2}{\omega(\omega^2 + \Gamma^2)} = \varepsilon_1 + i\,\varepsilon_2$$

Permittivity data (or dielectric function) obtained from direct measurements such as those by Johnson and Christy is often used in real calculations and simulations (Fig. 1.4a).[60,61] In terms of applications, gold (Au) and silver (Ag) are popular materials of choice for their strong plasmon resonance in the visible and near infrared. Gold is sometimes preferred for biological applications since it is well characterized, chemically stable, biological safe and can be easily functionalized with DNAs and other molecules.

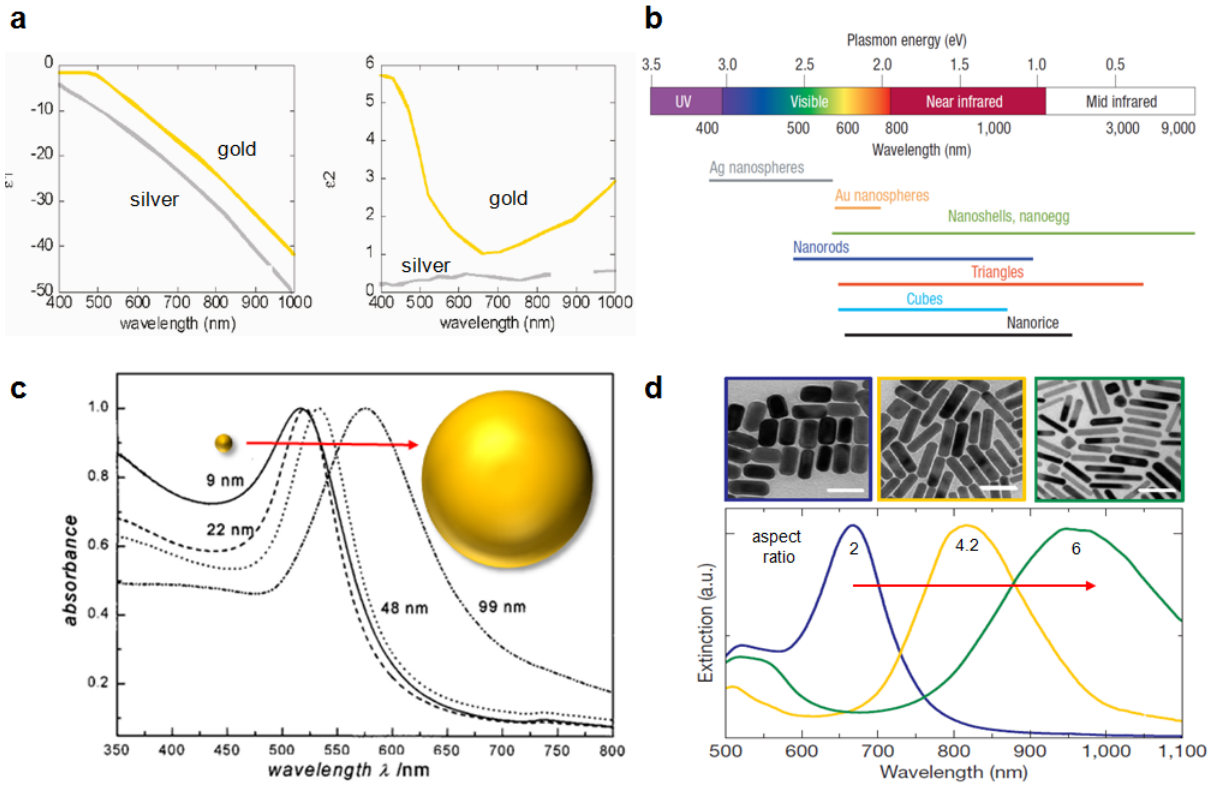

Figure 1.4 **a,** Real (left) and imaginary (right) parts of dielectric function of silver and gold.[60,61] **b,** A wide range of surface plasmon resonance peak is tuned by material, size and shape of nanoantennas.[14,20] **c,** Normalized absorption spectra of GNPs with various diameter.[62,63] **d,** SEM images of gold nanorods with various aspect ratio (top), along with corresponding extinction spectra (normalized by peaks, bottom).[64]

The Rigorous Field Distributions of a Metallic Sphere from Mie Theory

In 1908, Gustav Mie solved the light scattering and absorption problem of a sphere rigorously, using a full vector electrodynamics approach.[59] Consider a sphere of arbitrary radius a with a material permittivity ε_M and permeability μ_M buried in a surrounding medium characterized by ε_D and μ_D. In Mie theory, the incident, scattered, and internal electromagnetic fields (both inside and outside the sphere) are expanded as a linear superposition of weighted multipoles (monopole, dipole, quadrupole, etc.). As such, the scattered electromagnetic fields around a sphere can be solved, as shown in Fig. 1.3c. From a functional point of view, the plasmonic sphere can act as an optical nanolens since it distorts the flow of incident electromagnetic energy at specific frequencies.

The Simplified Field Distributions of a Small Metallic Sphere

For a small subwavelength particle ($a < 10nm$), the wave retardation of the incident

electromagnetic wave can be neglected.[24,25,60] The metallic nanosphere roughly experiences an uniform incident plane wave $\boldsymbol{E} \approx \boldsymbol{E_0}$ when its size is bigger than the mean path length and smaller than the skin depth. A sphere in this regime is known as a Rayleigh sphere. The electrostatic (or quasi-static) approximation can be used to simplify the electromagnetic problem. In this picture, the electric field pattern of a dipole inside $\boldsymbol{E}_M$ and outside $\boldsymbol{E}_D$ of the metal sphere are given respectively by

$$\boldsymbol{E}_M = \frac{3\varepsilon_D}{\varepsilon_M(\omega) + 2\varepsilon_D}\boldsymbol{E}_0$$

$$\boldsymbol{E}_D = \boldsymbol{E}_0 + \frac{3\boldsymbol{n}(\boldsymbol{n}\cdot\boldsymbol{p}) - \boldsymbol{p}}{4\pi\varepsilon_0\varepsilon_D}\frac{1}{r^3}$$

where $\boldsymbol{n}$ is an unit direction vector and r is the radius of particles. The dipole moment is expressed as $\boldsymbol{p} = \alpha\varepsilon_0\varepsilon_D\boldsymbol{E_0}$, with an induced polarizability α in the form of the well-known Clausius-Mossotti expression ,

$$\alpha = 4\pi a^3 \frac{\varepsilon_M(\omega) - \varepsilon_D}{\varepsilon_M(\omega) + 2\varepsilon_D}.$$

The field strength of this plasmonic dipole radiation pattern is affected by the size of the sphere and the material permittivity of the metal at different frequencies. In Fröhlich condition (the frequency satisfying $Re\{\varepsilon_M(\omega)\} = -2\varepsilon_D$), nanoplasmonic particles have strongest dipole.

Extinction, Scattering and Absorption cross-sections

The extinction cross-section represents the energy removed from the incident beam of light due to absorption and scattering events.[24,25,60] The light-scattering power of a particle is expressed in terms of the scattering cross-section σ_{sca}, which represents a hypothetical area for which a photon is scattered in an outward direction. The mutual relationship between the scattering, extinction and absorption cross-sections is $\sigma_{ext} = \sigma_{abs} + \sigma_{sca}$. For a small sphere in the Rayleigh regime, with polarizability α, the scattering and extinction cross-sections can be calculated as,

$$\sigma_{sca} = \frac{k^4}{6\pi\varepsilon_0^2}|\alpha(\omega)|^2 = \frac{8\pi k^4 a^6}{3}\left|\frac{\varepsilon_M(\omega) - \varepsilon_D}{\varepsilon_M(\omega) + 2\varepsilon_D}\right|^2$$

$$\sigma_{abs} = \frac{k}{\varepsilon_0}\, Im\{\alpha(\omega)\} = 4\pi k a^3 Im\left\{\frac{\varepsilon_M(\omega) - \varepsilon_D}{\varepsilon_M(\omega) + 2\varepsilon_D}\right\}$$

where $k = 2\,\pi/\lambda$. The scattering and absorption cross-section shows a maximum due to plasmon resonance when $Re\{\varepsilon_M(\omega)\} = -2\varepsilon_D$. For Fröhlich condition with water permittivity $\varepsilon_D \approx 1.7$, according to the dielectric function of silver and gold (Fig. 1.4a), the resonant peak for spherical gold nanoparticles in water is around 520nm (visible spectrum) and that of silver particles is in

the UV, at around 400nm (Fig. 1.4b).[25,60] These equations also indicates that the cross-sections and resonance peaks of scattering and absorption scale to particle size, *a*. Redshift occurs as the particle grows bigger (Fig. 1.4c). Furthermore, increasing ε_D results in redshift in plasmon resonance wavelength as well. That implies polarization is sensitive to the permittivity ε_D of local environment and can be used for local sensing.

With extremely large absorption and scattering cross-sections, metallic nanoparticles can be observed using simple and low-cost illumination setups such as a dark-field microscopy. Under white light illumination, gold nanoparticles appear as very bright spots, similar to fluorescent dyes but free of quenching and photobleaching. The light-scattering signal from a 60nm gold nanoparticle is roughly equal to fluorescent emission from 3×10^5 fluorescein dyes. In addition, silver nanoparticles can scatter light 2000-times more efficiently than same size of polystyrene particles.

Complex Nanoplasmonic Geometries

For a single metallic sphere, the parameters describing its optical performance can be prescribed very well by Mie Theory with dielectric function of metal. However, beside size and material composition of a nanoplasmonic particle, its shape can also affect photophysical properties (Fig. 1.4).[25,60] As progress in fabrication of metal nanostructures lead to a proliferation of plasmonic geometries such as nanospheres , nanorods , nanotriangles , nanocrescents , just to name a few, plasmonic particles cover different portion of the scattering spectrum and can perform usefully in diverse applications (Fig. 1.4b). To design complex nanoplasmonic antennas, many theories and simulation methods are developing. Nanorods, for instance, can be modeled analytically by Gans Theory to explain thier field distribution and redshift. In such description, spheres are elongated into ellipsoids through an aspect ratio length over diameter (b/a) to explain to explain thier redshift (Fig. 1.4d). Moreover, to quantitatively describe the optical response of arbitrary complex metallic structures, various electromagnetic numerical methods can be employed: Discrete-Dipole Approximation, Finite-Difference-Time-Domain, T-matrix, or Transformation Optics. Each one has strength and weakness in terms of accuracy, intuitiveness, easiness of application and computational power.

Complex nanostructures can consist of a potpourri of strongly interacting plasmonic particles. .[25,27,60,65] In linear structures with strong interparticle coupling (e.g. GNP-GNP dimers) scattering fields are obtained not only through superposition of individual responses but also from the mutual interaction between scatters along a highly polarizable axis. Plasmon dimer pairs couple strongly depending on their gap size. A spherical dimer redshifts and enhances its near-fields monotonically with decreasing gap size. In coupled structures where interparticle near-fields overlap significantly, additional resonances are also possible due to the strong interactions between localized plasmon modes (Fig. 1.5a). Another pairing effect is the plasmonic Fano resonance which results from the constructive or destructive interference between a spectrally overlapping broad resonance and a narrow discrete one. A plasmonic nanoparticle exhibits a tunable Fano resonance with varying degree of interparticle distance (Fig. 1.5b). A large and unique spectral shift induced can be applied in chemical and biological sensing.

Metallic nanostructures can interact with molecules through their electronic dipole (for instance with fluorophores and Raman reporters) to enhance their emission signals.[26,33-37,40-42] Also the sensing volume (defined by the size of hot-spots) is greatly reduced. Various nanogap metallic structures have achieved large magnitude in fluorescence and Raman enhancements. However, most of nanogap structures have been produced by expensive and sophisticated nanofabrication techniques such as electron beam lithography and focused ion beam techniques. Lowering the fabrication threshold and developing microfluidic integratable enhancement substrate would widen their applicability and accessibility for biomedical applications. For example, Lee's group recently developed simple methods to fabricate large-scale high-density nanogap structures on low-cost polymer substrates (Fig. 1.5c).[66,67] By just leveraging the stiffness mismatch of materials, metal deposition and subsequent heating above the glass transition temperature of polymer sheets cause the substrates to retract and non-shrinkable metallic materials to buckle. The enhancement of intensity of hot-spot is due to small nano-gaps. The nanometer-sized gaps with effectiveness in surface enhanced sensing have been demonstrated. In addition, these metallic structures can be easily integrated into polymer-based microfluidic devices or deformed into complex 3D geometries.

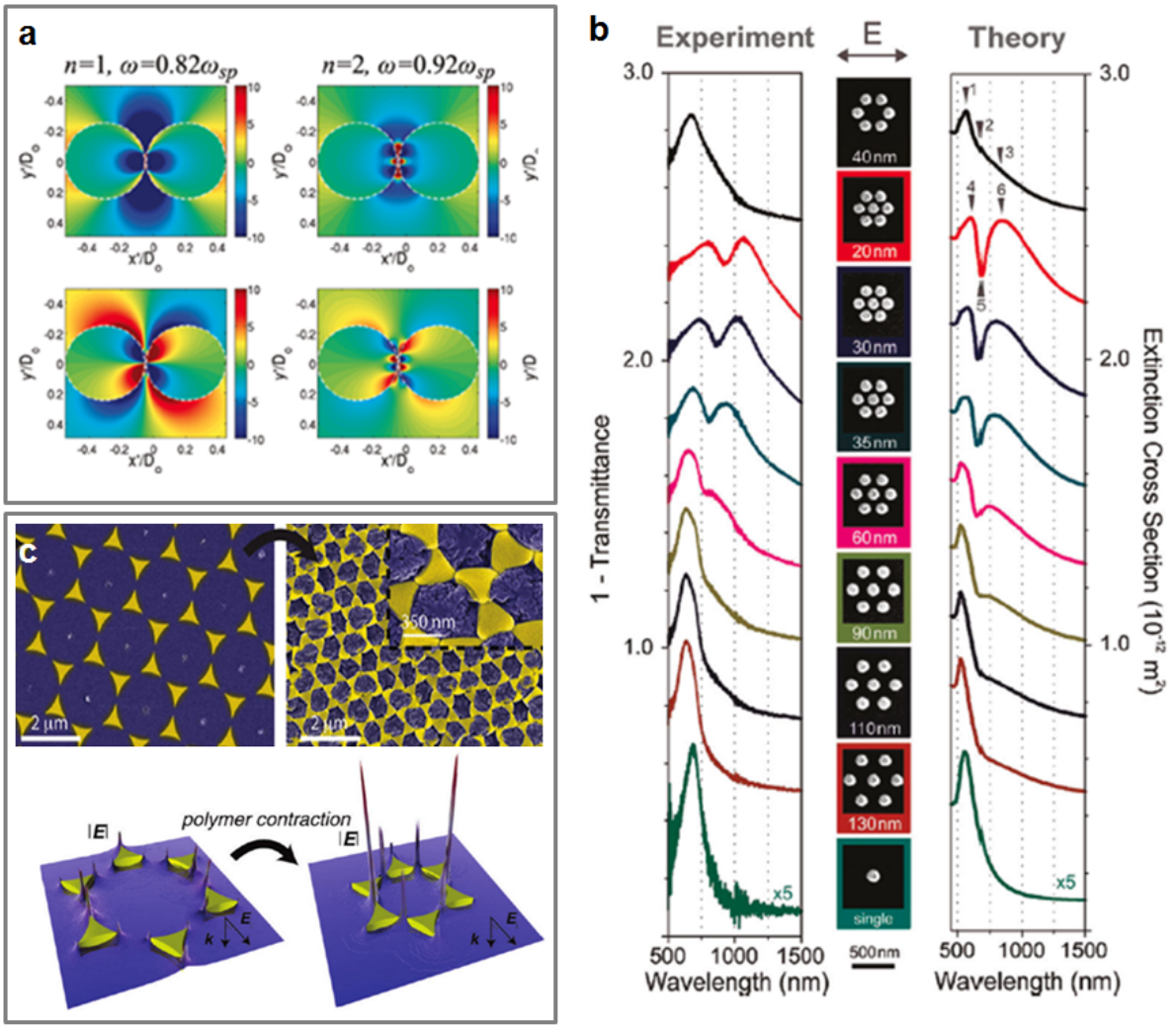

Figure 1.5 Simulation and design of plasmonic coupling and hot-spots. **a,** Near-field enhancement of touching sphere as calculated semi-analytically through the use of Transformation Optics.[26] **b,** Demonstration of Fano resonances in a variety of plasmonic disk oligomers patterned lithographically. The measured and theoretically transmission spectra shows the tuning of the asymmetric Fano resonance with different interparticle separations.[68] **c,** Top, SEM images of gold nanoprisms on polymer substrates before (left) and after (right) contraction. Bottom, a finite element simulation of electric field amplitude around nanoprisms and nanogaps.[69]

1.3 Nanoplasmonic Molecular Ruler

One of the key avenues to understanding how biomolecules interact at the single molecular level is through the measurement of their intramolecular distance. Fluorescence resonance energy transfer (FRET) is a technique widely adopted for this purpose and is popular due to its single molecular sensitivity and easiness of specific targeting. However, FRET is unsuitable for

measurement of large conformational changes since the performance is often hampered by its short detection range (~5nm). To improve the detection range, long-range molecular rulers, based on shifts in single-antenna LSPR, are used to overcome these limitations.[27,28,65,70,71] In nanoplasmonic molecular rulers, the LSPR extintion peaks is a function of the local refractive index change Δn of the environment at the vicinity of the nanoantennas. Thus, molecular interactions on the surface of metal can be locally probed by monitering scattering spectrum shift of nanoantennas $\Delta\lambda$, as given by

$$\Delta\lambda_{max} = m\Delta n\left[1 - exp(\frac{-2d}{l_d})\right]$$

where m is the bulk refrative-index of the enviroment, Δn is the chage in refrative index due to molecular interactions around antennas, d is the effective thickness of absorbate layer, and l_d is the characteristic evanescent field length into the sample (normally in order of 10-nm).

One typical experimenal setup of a nanoplasmonic molecular ruler is shown on Fig. 1.6a. A glass plate coated with nanoantennas was mounted on a dark-field optical microscope for experiment. Excitation of the sample was made through a dark-field condenser lens (NA. 1.2–1.4) with a broadband white light lamp. The scattered intensity of single nanoantennas was collected by a microscope objective lens (NA ~0.65, smaller than that of dark-field condenser lens) and detected by a true color charge-coupled device (CCD) camera. After obtaining the images, the corresponding scattering spectrum can also be measured by a spectrometer.

To test molecular interactions induced scattering spectrum sift, 20-nm Au nanoparticles were conjugated with 54-bp (length ~18nm) double-stranded DNA (dsDNA) molecules (Fig. 1.6b).[28] DNA hydrolysis cased by Bal31 exonuclease was monitored in real-time by tracking shift in plasmon resonance wavelength of individual probes, corresponding to dsDNA length. An average wavelength shift of ~1.24 nm/bp was observed and the range of detection was close to 20nm, longer than the effective distance of FRET (Fig. 1.6c). In addition to long-range detection, nanoplasmonic rulers are photostable, free of photobleaching and blinking over organic dyes, thereby allowing long-term monitoring of single biomolecular interactions with high temporal resolution. It has been demonstrated that photostable gold nanoparticles ensure long-term (short-term as well) detection of DNA foot-printing and nuclease activity. On the other hand, coupling-type plasmonic rulers have been applied to various applications in biology, such as protein induced DNA bending and DNA cleavage by restriction enzymes.

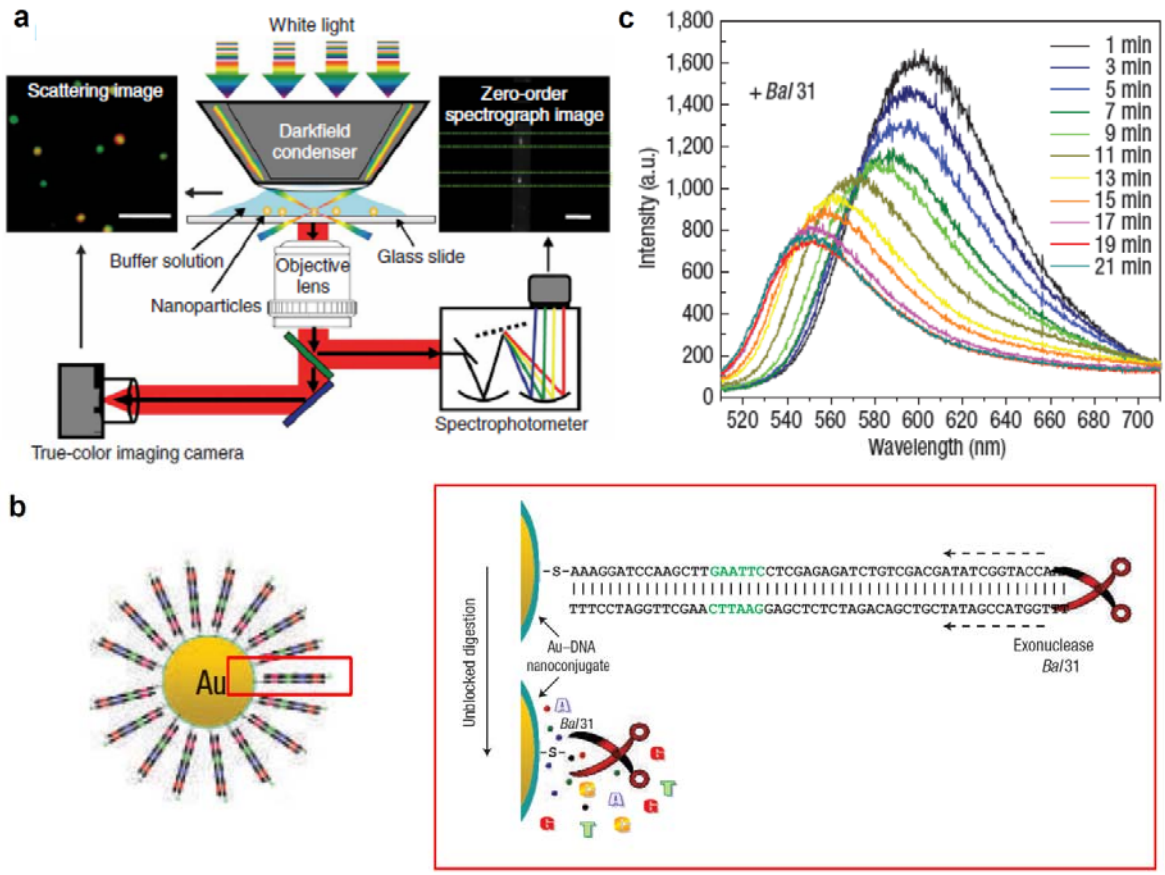

Figure 1.6 Nanoplasmonic molecular rulers for real-time monitoring biomolecular interactions.[28,31] **a,** Experimental system configuration for dark-field imaging and recording scattering spectrum of single nanoantennas. **b,** Design of Au–DNA nanoplasmonic molecular rulers for real-time monitoring dsDNA hydrolysis by Bal31 exonuclease. **c,** Time-dependent scattering spectra from single plasmonic ruler during DNA hydrolysis.

1.4 Plasmon Resonance Energy Transfer

Absorption spectroscopy utilizing the interaction of light and molecules has been used for a long time. However, serving as a molecular biophotonic tool, conventional absorption spectrometers have a major limitation. The spatial resolution of optical systems cannot break the diffraction limit of light. Therefore, it is hard to obtain absorption spectrum for single (or few) molecules. As suggested recently, the plasmon energy from nanoplasmonic particles can be transferred to surrounding biomolecular acceptor, allowing nm-scaled measurements of molecular absorption spectra. When the plasmon resonance peak overlaps well with biomolecule absorption peaks, the PRET effect contributed to specific quenching dips on the Rayleigh scattering spectra of biomolecule-conjugated nanoantennas (Fig. 1.7a). [29-32]

For example, when nanoantennas conjugated with reduced cytochrome c, dramatic quenching was observed in their scattering spectrum and the positions of dips matched well with absorbance peaks of adsorbed molecules (Fig. 1.7b and 1.7c).[31] This label-free nanoplasmonic method

provides an ultrasensitive biomolecular absorption spectroscopy techniques for probing a small number of biomolecules. In addition to *in vitro* measurements, PRET-based spectroscopy techniques have been applied in real-time monitoring expression of cytochrome c in living cells.[29] During ethanol-induced apoptosis, HepG2 cells released cytochrome c molecules from the mitochondria to the cytoplasm, resulting in specific dips in the scattering spectra of the intercellular antennas. More recently, by conjugating with metal specific ligands, PRET probes can be used for the detection of metal ions (e.g. Cu), which plays important roles in molecular biology, cell biology and environmental research (Fig. 1.7d).[32] Beside several orders of magnitude in improvement of sensitive, this method showed high selectivity, depending on the conjugated ligands.

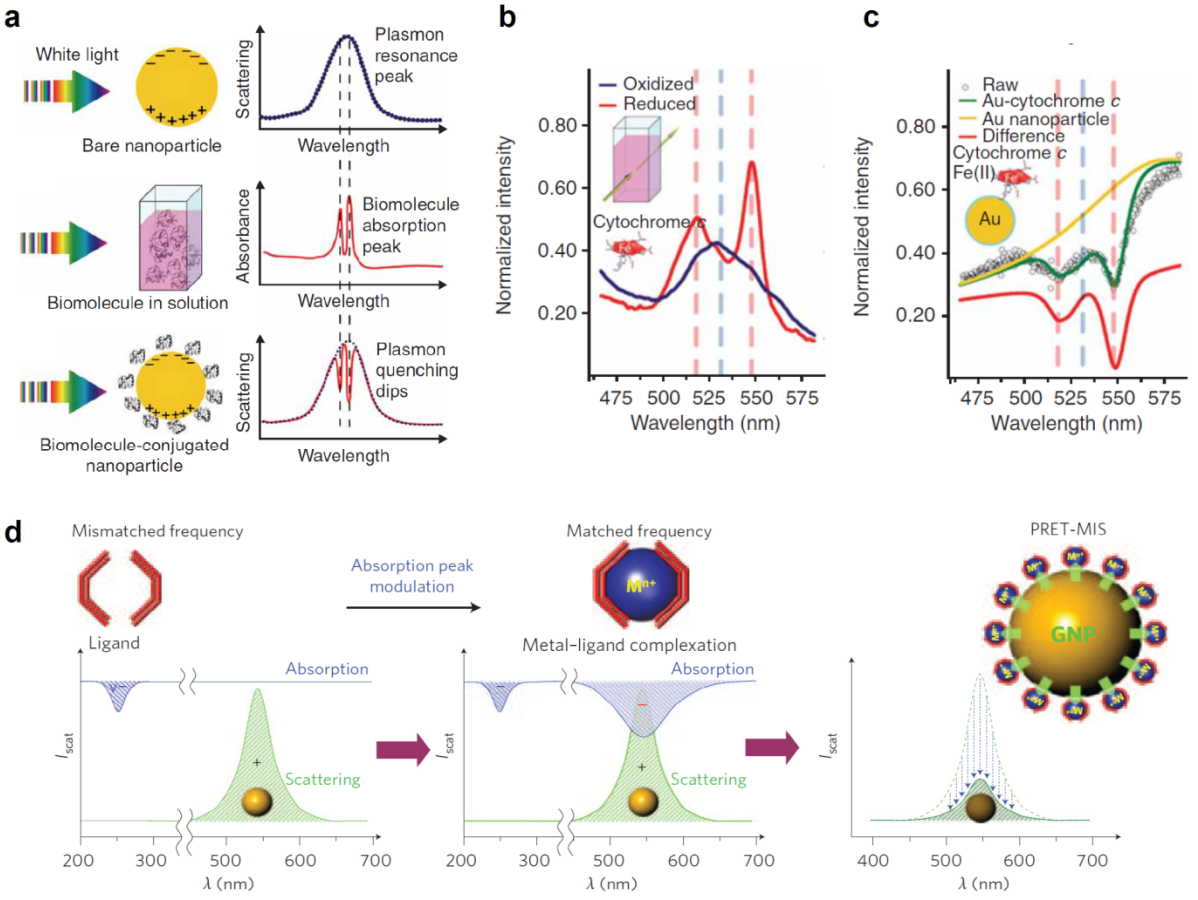

Figure 1.7 Plasmon resonance energy transfer.[29-32] **a,** Plasmon quenching dips (bottom) in the scattering spectrum of a GNP (top) match well with the absorption speaks of biomolecules in bulk solution (meddle). **b,** The absorption spectra of oxidized (blue solid line) and reduced (red solid line) cytochrome c in bulk solution. **c,** Plasmon quenching dips (red line) of GNPs/ reduced cytochrome c complex, obtained by subtracting the raw data (green line) from scattering spectrum of bare GNPs (yellow line). **d,** PRET-based sensing of metal ion. The electronic absorption peak of ligand / metal ion complex can be tuned to ~540nm, matched the SPR spectrum of GNPs (left and middle). Local concentration of metal ion can be measured by the resonant quenching in Rayleigh scattering spectrum (right).

1.5 Metal Enhanced Fluorescence

Fluorescence is one of the most widely used light-matter interactions for probing biological systems function owing to its high sensitivity and capabilities of multiplexing. Organic dyes and fluorescent proteins are two types of probes widely adopted for this purpose. However, their low quantum yield, photobleaching and blinking problems inevitably restrict their applications for long-term observations *in vitro* or *in vivo*. In recent years, fluorescent nanoparticles (such as quantum dots and fluorescent nanodiamonds) have gained considerable attention because of their high photobleaching thresholds. To further improve the signal-to-noise ratio of fluorescence signals, the MEF technique utilized metallic nanostructures in which the surface plasmons resonate with the molecular dipole of the fluorophores to reduce their fluorescence excited state lifetimes and simultaneously increase their emission intensities.[33-37] In fluorescence emission, the quantum yield (Q_0) and lifetime (τ_0) of fluorophores in free space are defined by the radiative rate (Γ) and the non-radiative rate (k_{nr}),

$$Q_0 = \frac{\Gamma}{\Gamma + k_{nr}}$$

$$\tau_0 = \frac{1}{\Gamma + k_{nr}}$$

With the presence of a nearby metallic nanostructures, an additional radiative rate factor (Γ_m) is introduced, therefore increasing the quantum yield (Q_m) while reducing the excited state lifetime (τ_m),

$$Q_m = \frac{\Gamma + \Gamma_m}{\Gamma + \Gamma_m + k_{nr}}$$

$$\tau_m = \frac{1}{\Gamma + \Gamma_m + k_{nr}}.$$

The effect of fluorophore–metal interactions is distance-dependent.[72] Single plasmonic particles/single dyes experiments indicated that the maximum fluorescence enhancement occurred at a separation distance of 5-10 nm between surface of metal and fluorophores (Fig. 1.8a). On the other hand, short distances of gaps (0–5 nm) can include fluorescence quenching. It is suggested that covering the metallic nanostructures with nm-thick buffer layers is essential for achieving the largest MEF effect. Typically, a 2- to 10-fold enhancement ($\gamma_{em}/\gamma_{em}^0$) in the fluorescence emission can be obtained. To overcome such low efficiency of enhancement due to weak hot-spots, nanotechnologies have been involved. For instance, coupled nanoparticles, metal tips, nanopockets, optical antennas, and feed gaps have achieved 10-to 1,000-times enhancements of fluorescence emission and reduced excitation volumes to atto-to zeptoliter.[33-36,72-80]

In single molecule experiments, bowtie nanoantennas have been used to facilitate detection of single dye molecules and showed a 1,340-fold increase in fluorescence intensity (Fig. 1.8b).[77] The spatial extent of the enhancement hot-spots, as small as 15-nm, has been measured by single molecule imaging as well. Also, in biomedical applications, MEF technique has been used in improving the detection limit of immunoassay and DNA hybridization (Fig. 1.8c).[34]

Silver island films are general substrates often used to meet such purpose. For example, the cardiac marker myoglobin was captured by antibody-coated plasmonic substrates and then further labeled by dye-labeled anti-myoglobin antibodies. Compared with glass substrates without MEF effect, around 10-fold enhancement on fluorescence signal was observed. That improved the detection limit down to 10 ng/mL, lower than cut-off concentrations for myoglobin for clinical studies (Fig. 1.8d and 8e). To lower the fabrication threshold as well as to develop microfluidic integratable metallic nanostructures, our group recently presented a simple, ultra-rapid and robust method to create sharp nanopetals structures in a shape memory polymer substrate over large surface areas.[73,74] Extremely strong surface plasmon resonance due to the high-density multifaceted petal structures increases fluorescence emission by thousands-fold. This microfluidic-integratable material enables us to apply MEF techniques in point-of-care biomedical diagnosis.

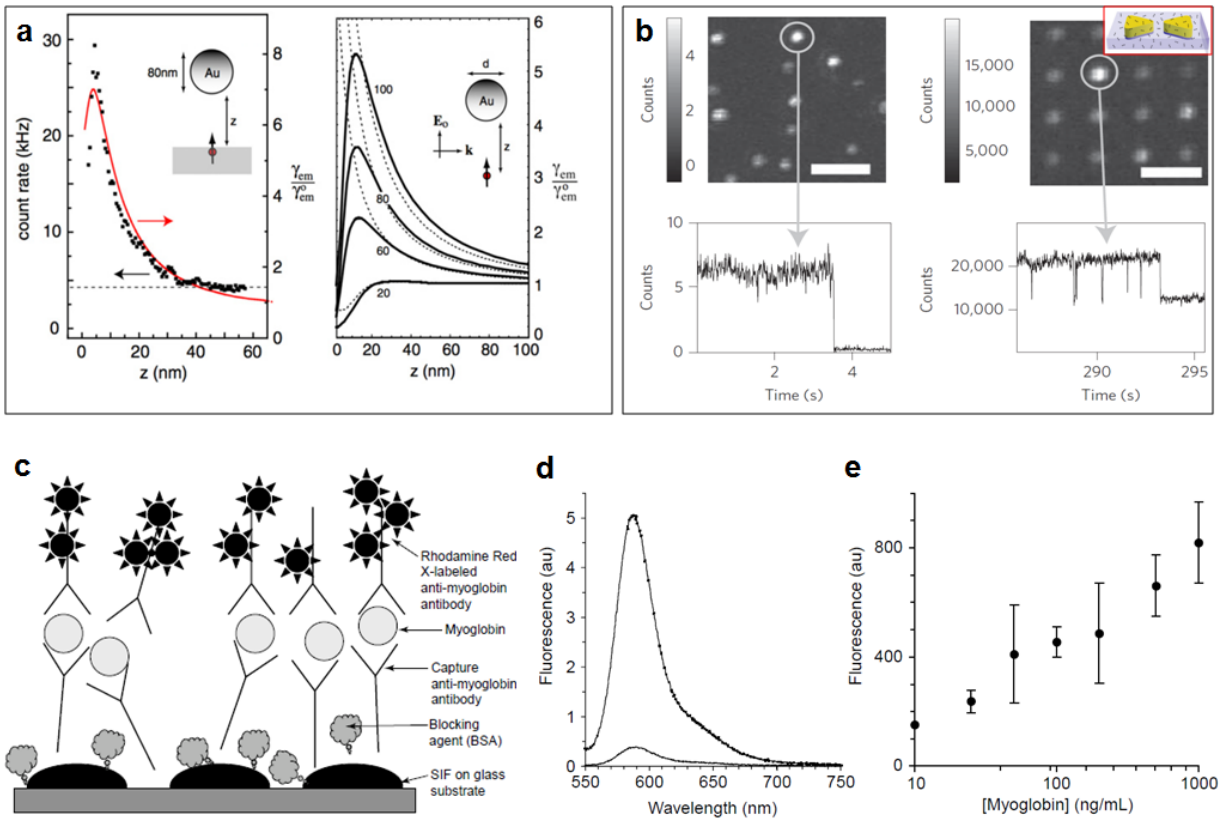

Figure 1.8 Metal-enhanced fluorescence (MEF). **a,** Interaction of a metallic nanoparticle and a fluorophore in the near-field. The metal–fluorophore coupling increases both absorption and emission rates of the fluorophores. Fluorescent emission rate (left axis) and factors of enhancement (right axis) as a function of the gap between GNPs and fluorophores.[72] **b,** Fluorescent images (top), together with time traces of intensities (bottom), of single dye molecules without (~7 counts, left) and with enhancement (~20,000 counts, right) by bowtie nano-structures (top-right inset).[37] **c,** Schematic illustration of metal-enhanced immunoassay by silver island film (SIF).[34] **d,** Fluorescence spectra of anti-myoglobin antibody (Rhodamine Red-X-labeled) / myoglobin sandwich on SIF (with MEF, strong intensity) and on a glass slide (without MEF, weak intensity). **e,** The detection limit of myoglobin can reach 10 ng/ml with MEF techniques.

1.6 Surface enhanced Raman spectroscopy

Raman scattering is a light-matter interaction that occurs when incident photons are scattered inelastically from molecules. The resulting photons may gain or lose energy after scattering (Fig. 1.9a). Under irradiation ($h\nu_L$), a red-shift in scattering is referred to as *Stokes shift* if the interaction causes the vibrating molecule with energy $h\nu_M$ to re-emit a photon of signal $h\nu_S$, corresponding to an energy difference between a higher vibrational energy and incident excitation levels ($h\nu_S = h\nu_L - h\nu_M$). On the other hand, light is blue-shifted and its shift is known as *Anti-Stokes* if the signal $h\nu_{AS}$ occurs with a difference between a lower vibration energy and incident excitation levels ($h\nu_{AS} = h\nu_L + h\nu_M$). The vibrational energy $h\nu_M$ is characteristic of the molecule in question and can be served as a unique spectroscopic signature. However, unlike the elastic Rayleigh scattering process, the Raman one occurs much less frequently. The weak effect of Raman is evaluated at a small absorption cross-section in the order of $\sigma^R \sim 10^{-30} cm^2$ per molecules, whereas that of the fluorescence is at $\sigma^R \sim 10^{-16} cm^2$.[40-42]

The weak Raman signal can be enhanced by several orders of magnitude in SERS. This is done chemically or electromagnetically by the adsorption of molecules near surface of metals. The electromagnetically enhancement plays the main role because SERS scales roughly with the "fourth" power of electric field enhancement (hot-spots). Such strong enhancement makes Raman scattering from single molecules strong enough to be detected (Fig. 1.9b).[81,82] Polarized confocal microscopy with spectroscopy was used to probe ultra-low concentration of Rhodamine 6G molecules. The order of $\sim 10^{15}$ fold enhancement in Raman scattering from single silver particle measurements was much larger than the ensemble-averaged values derived from traditional methods. Such SERS effect provides single-molecular Raman single which are stronger and more stable than single-molecule fluorescence.

Although single-molecular SERS opened a new way in label-free ultra-sensitive detection, there are some additional concerns with respect to SERS-based molecular detection. For instance, because the enhancement occurs on few nanometers away from the surface of SERS substrate, it requires analytes extremely close to the surface. Especially in bulk single-molecular detection, the possibility for analyte reaching hot-spots becomes very low. In the bulk solution, the mean free path of molecules (depending on the diffusion coefficient of molecules) is in the scale of micrometers, much smaller than the scale of sample chambers. This mismatch results in dramatically decreasing in sensitive and making detection time extremely long. To address this problem, microfluidic chips basically lower the channel height to approach the mean free path of analytes, and hence increase the accessibility of molecules to the surface hot-spots. SERS substrates have been integrated into micro- or nano-fluidic chips.[83-88] For example, a silver nanowell array was fabricated in microfluidic devices made by polydimethylsiloxane (PDMS). Compared to smooth silver surface, nanowell-based SERS substrates show 10^7-fold of enhancement in SERS single.[88] It is possible to detect molecules with concentration as low as 10 fM (Fig. 1.10a). In addition to improvement in sensitivity, SERS substrates/ microfluidic systems also make high-throughput analysis possible, in accord with their capability of multiplexing.

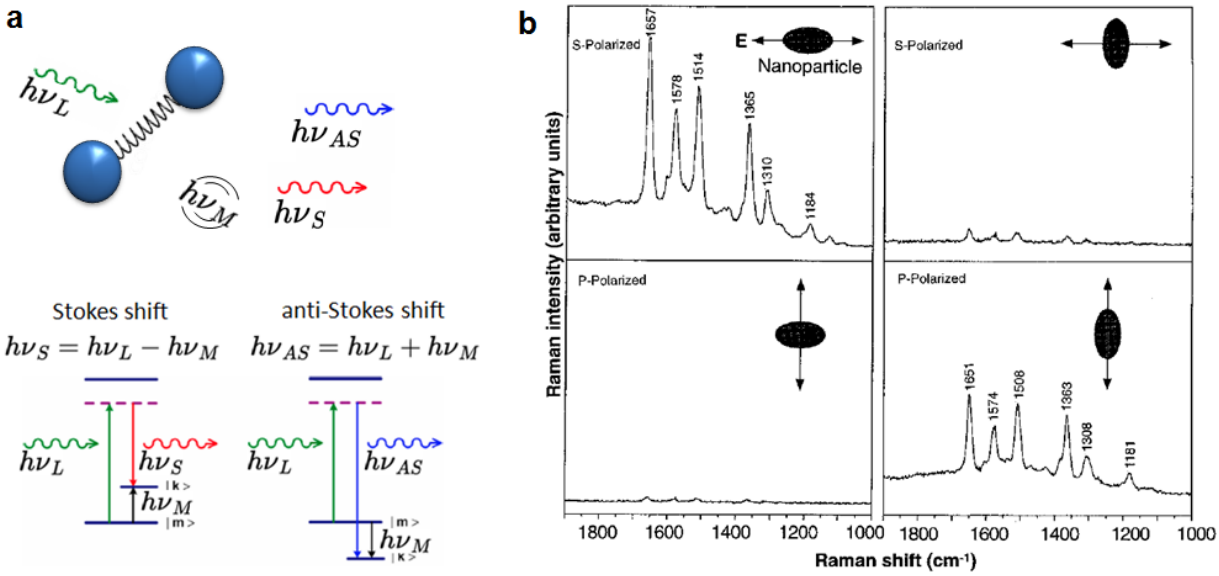

Figure 1.9 Fundamentals of surface enhanced Raman spectroscopy (SERS).[41,42] **a,** A molecule undergoing non-resonant Raman scattering interplay between the incident photon and vibrational energies. The Stokes shift corresponds to reduction in photon energy (redshift with a longer scattering wavelength) whereas the anti-Stokes, an addition in photon energy (blueshift with a shorter scattering wavelength). The purple doted upper lines denote virtual states for the fact that, contrary to fluorescence, Raman scattering is a non-resonant light absorption and can occur without resonant absorption corresponding to electronic states. **b,** The hot-spots around metallic nanoparticles can enhance Raman single of molecules over 10^{15}-fold, which resulted in finger-print-like SERS spectrum. Single-molecular SERS was demonstrated by specific SERS signal and controlled by the direction of laser polarization and orientation of the particle.[81]

Instead of locating samples to SERS substrates, an alternative way is to move hot-spots close to samples. For instance, tip-enhanced Raman scattering (TERS) utilizes the hot-spot at a metal-coated atomic-force microscope (AFM) tip to locally enhance molecules with spatial-resolution down to few nanometers (Fig. 1.10b).[39,89-91] This method has been applied to obtain sub-molecular Raman scattering spectra from various biomolecules, such as DNA, RNA and peptides. Specific Raman spectra were obtained along single RNA strands and demonstrated the potential of being a method for direct-sequencing.

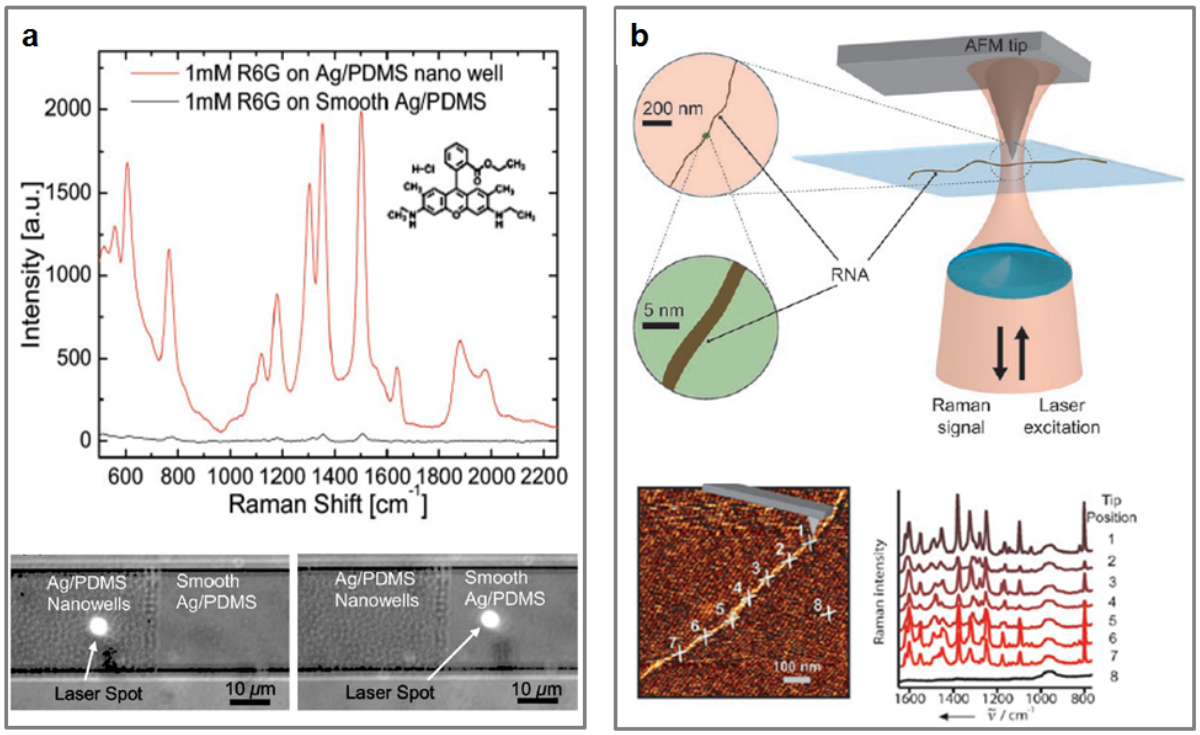

Figure 1.10 Applications of SERS in vitro. **a,** Images of nanowell arrays fabricated by soft-lithography for biomolecular SERS detections in integrated microfluidic channels (bottom).[88] Top, SERS spectra of R6G molecules taken from Ag/PDMS nanowell arrays (red) and from smooth Ag/PDMS surface (blue). **b,** Top, experimental system configuration for scanning single RNA stands by tip-enhanced Raman spectroscopy.[39] Bottom, a topography image (left) and corresponding tip-enhanced Raman scattering, collected from various position along a single RNA strand (right), demonstrated single RNA detection.

Recently, for cellular experiments, SERS has been utilized in mapping of pH inside living mouse fibroblasts by monitoring SERS spectra of pH-sensitive molecules (e.g. 4-mercaptobenzoicacid, pMBA). GNP-pMBA nanoantennas were introduced into cells and SERS spectra from individual probes provided a map of pH value based on the ratio of spectrum lines at 1423 and 1076 cm^{-1}(Fig. 1.11a).[43] Dynamic monitoring of pH changes provide a new way to study cell-cycles and metabolic processes with sub-cellular resolution. In addition to single SERS particles applications, dimer-enhanced SERS was used to study the dynamics of receptors aggregation on cell membrane (Fig. 1.11b). GNPs were conjugated with receptor-specific binding antibodies and targeted on corresponding receptors. Receptor aggregation induced GNP-GNP dimer formation. Strong coupling between GNPs further enhanced intensity of hot-spots and therefore generate stronger SERS signal. Studying the dynamics of cell membrane proteins might provide more detail information regarding cellular interaction and communication.[38]

In addition to *in vitro* detection, SERS-based diagnosis has also been tested for *in vivo*

applications as well.[46,92-95] For example, tumor targeting and detection has been demonstrated by SERS nanoparticles. Pegylated colloidal gold nanoparticles were conjugated with Raman reporters and single-chain variable fragment (ScFv) antibodies for specific targeting epidermal growth factor (EGF) receptors on cancer cells (Fig. 1.12a).[46] The intensity of SERS nanoparticles was much brighter than semiconductor quantum dots in near-infrared biological window. After incubation with cancer cells (expressing EGF surface markers), ScFv-SERS nanoparticles can specifically target those cells and provide strong SERS signal (Fig. 1.12b). On the other hand, in negative control experiments (without ScFv conjugation in SERS particles or without EGF expression in cells), SERS signal was significantly weak. To demonstrate the capability of *in vivo* cancer targeting, nanoparticles were injected into tails of nude mice and wait for 5 hours before recording spectra (Fig. 1.12c). A NIR laser with wavelength at 785-nm was equipped for penetrating the skin and exciting SERS particles. SERS single detecting from tumors was stronger than non-tumors spots, such as liver (Fig. 1.12d).

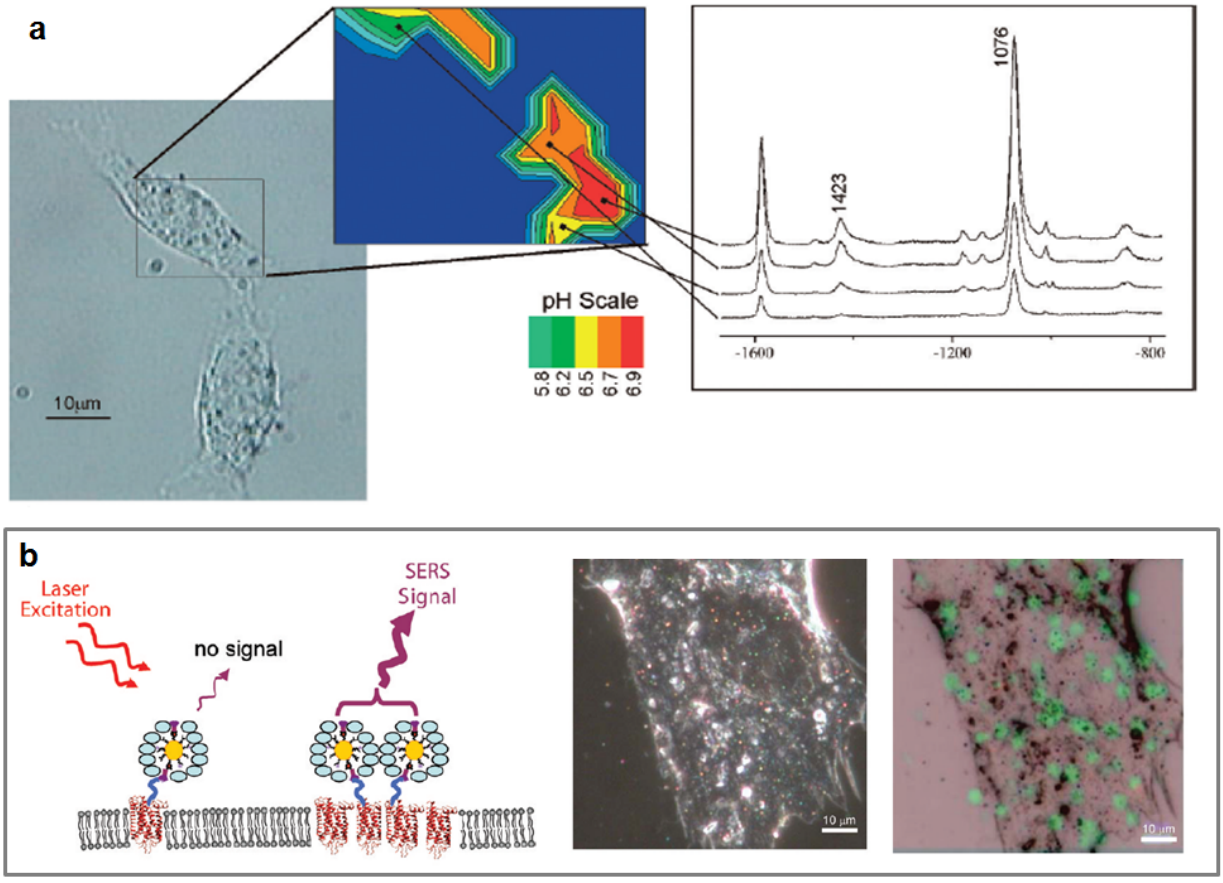

Figure 1.11 Applications of SERS in studding dynamics of single cells. **a,** Subcellular mapping pH in living cells by measurements of SERS spectrum of 4-mercaptobenzoic acid (pH-sensitive probes).[43] **b,** Cell membrane receptor-specific binding antibodies were conjugated with GNPs (left) for detection of receptor dynamics on cell membrane. A dark-field image has shown a cell with GNPs binding (middle). Strong coupling of GNPs enhanced strong SERS single (green dots) and indicated aggregation of receptors on cell membrane.[38]

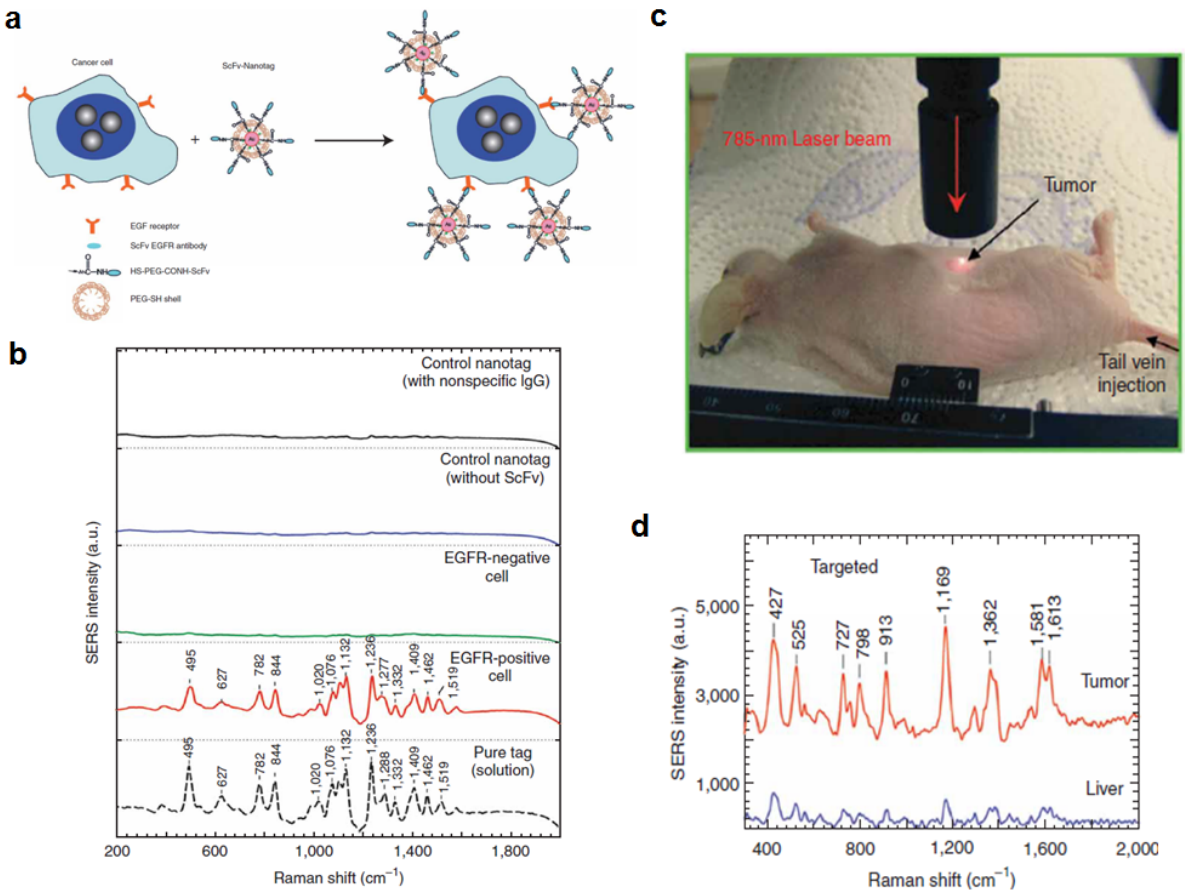

Figure 1.12 Applications of SERS in vivo. **a,** Preparation of antibody-conjugated SERS nanoparticles for targeting cancer cells with spectroscopic detection. **b,** SERS spectra recorded from EGFR-positive cancer cells (red line) and from EGFR negative cancer cells (green line), along with other controls. **c,** Tumor targeting and SERS detection by antibody-conjugated SERS nanoparticles in a small animal. **d,** SERS spectra obtained from the tumor (red line) and the liver (blue) *in vivo*.

1.7 Plasmonic Enhanced Photothermal Effect

Upon laser excitation using a pulsed or continuous wave, the photothermal response of metallic nanoparticles involves many energy conversions occurring at different time scales.[25,96] The response can be *internal* to the plasmonic particle where the particle becomes a source of heat due to inner dynamic of particles or *external* where the core and the electromagnetic energy establish how heat is transferred to the environment. Following the absorption of photons by metallic nanoparticles, plasmons are excited via LSPR. Inside particles, the interplay between photons, plasmons and phonons inside the conductor – quanta of light, charges or lattice vibration – determine the internal energy conversion to heat and the time scales of each steps. Towards outside, heat is transferred across the boundary of the metal-surrounding interface and is dissipation to the immediate surroundings.

Internal to the sub-wavelength metal nanoparticle following the absorption of a fs pulse laser, LSPR occurs from the collective conduction electron oscillation and rapidly dephases (Fig. 1.13a).[25,96] The broadening of the resonance line width is due to surface free electron scattering surfaces for small particles in the quasi-static regime and to radiation damping for larger ones. The broadening can quantitatively given by examining the complex dielectric function. The real part determines the position of the resonance and the imaginary part gives the dephasing. The line width is defined by

$$\Gamma = \gamma + \frac{Av_F}{l_{eff}} + 2\hbar\kappa V$$

where γ is the bulk damping constant, A is a constant that characterize electron scattering, v_F is fermi velocity, l_{eff} is effective path length of electrons, $\hbar = h/(2\pi)$ is the reduced planck constant, κ is a phenomenological damping efficiency constant, V is the polarization volume. Note that the third term is volume dependant and is negligible for small nanospheres. Usually, the LSPR line width is on the order of 20 nm. The dephasing time is very fast, estimated at around 10 fs.

The energy through dephasing due to surface electron scattering is then partially converted non-thermally over the conduction bands through interbands or intraband transitions in which electrons are excited (Fig. 1.13a).[25,96] This electron distribution reaches equilibrium through electron-electron scattering on a few 100fs time scale before they create a hot electron distribution with a new equilibrium temperature higher than the lattice phonon temperature, causing energy transfer from electrons to lattice phonons. This process is referred to as electron-phonon relaxation and happens within a few ps. This is manifested as vibrations of the lattice and raises the overall temperature of the nanoparticle in contact with its surrounding medium.

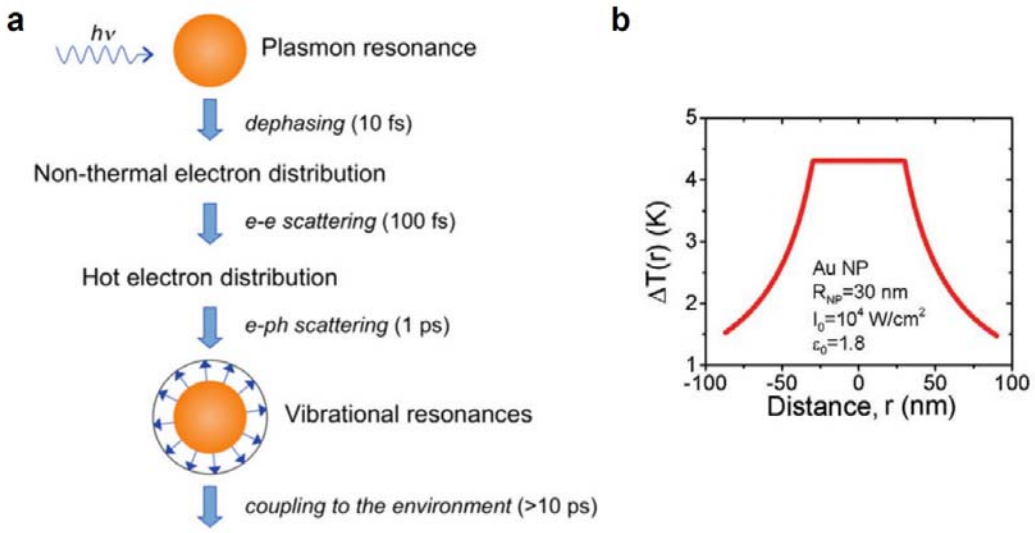

Figure 1.13 Localized photothermal conversion based on plasmonic nanoparticles. **a,** Sequence of photothermal conversion and heat diffusion following electromagnetic radiation.[25] **b,** Calculated temperature profile (cross-sectional) for a single GNP under irradiation.[96]

The EM contribution arising from the field inside the nanoplasmonic structures can be described through a heat transfer equation. This gives an evaluation of the amount of temperature change the hot plasmonic source of heat gives off to the surrounding environment (Fig. 1.13b). Without phase transformation, the heat transfer outward at the metal-water interface at R is governed by

$$\rho_M c_M \frac{\partial T(\boldsymbol{r},t)}{\partial t} = \begin{Bmatrix} \kappa_M \nabla^2 T(\boldsymbol{r},t) + Q(\boldsymbol{r},t) & inside \\ \kappa_W \nabla^2 T(\boldsymbol{r},t) & outside \end{Bmatrix}$$

where ρ_M is mass density of metal, c_M is its specific heat, $T(\boldsymbol{r},t)$ is temperature field, k_M and k_W is the thermal conductivity of metal and water, respectively. $Q(\boldsymbol{r},t)$ is local heat intensity as a function of joule heating average. $Q(\boldsymbol{r},t) = \langle \boldsymbol{J}(\boldsymbol{r},t) \cdot \boldsymbol{E}(\boldsymbol{r},t) \rangle$ given by the time-averaged value of Joules heating (energy lost resistively) and can be calculated with the knowledge of the fields inside the sphere, The heat transfer equation above is usually solved numerically except in the case of a perfectly spherical nanoparticle which can yield an analytical solution. The analysis can be performed for a continuous wave or pulse.[25,96] In steady-state, the expression for a metallic nanosphere of radius r with a volume V_{NP} is

$$\Delta T(\boldsymbol{r}) = \frac{V_{NP} Q}{4\pi k_0 r}.$$

where k_0 is the thermal conductivity of surrounding medium. An example of the difference in temperature of a GNP sphere as a function of its radial distance is plotted in Fig. 1.13b.

To remotely manipulate gene delivery, a new method based on photothermal effect of plasmonic nanoparticles is demonstrated for precisely controlling gene expression in live cells using near-

infrared (NIR) laser.[22,48,49,97,98] The NIR laser has long tissue penetration depth, suitable for *in vivo* experiments. Gene delivery and interference are important steps in controlling cell behaviors and reprogramming cells by introducing biomaterials, such as DNA, RNA, small molecules, and proteins. To perform remote light-induced molecular delivery, NIR-absorbed gold nanorods (GNRs) are often used to convert light to thermal energy. After absorption of high power of pulse NIR laser, rod-like gold nanoparticles can transfer their shape to spherical and result in surface atom rearrangement, together with molecular releasing. For example, when GNRs conjugated with enhanced green fluorescent protein (EGFP) plasmid DNA, this shape transformation broke the chemical bonds between gold and DNA and therefore triggered gene releasing (Fig. 1.14a).[97] HeLa cells with EGFR-gold nanorods uptaken showed strong GFP expression after irradiation (Fig. 1.14b). It has been demonstrated that plasmonic nanoparticles are promising materials to be used as vectors for remotely control gene delivery without causing serious cell damage.

On the other hand, under low power irradiation, nanoplasmonic particles can be slowly heated up without dramatically changes in their shape.[22,49,98] Heating above the melting temperature of conjugated molecules can also induce local molecular delivery. For example, downstream gene interference can be achieved by nanoplasmonic particle-mediated small DNA or RNA deliveries. After antisense DNA conjugated GNRs introduced into BT474 breast carcinoma cells, small DNA molecules can be released in cytosol by heating GNRs over melting temperature of DNA complex (Fig. 1.14c). After hybridization of antisense DNA/target ERBB2 mRNA in cytosol, ubiquitous RNase H-mediate gene silencing down regulates the expression of ERBB2 proteins, demonstrated by fluorescence imaging (Fig. 1.14d).

An additional advantage with respect to plasmonic GNR is that their light absorption properties are subject to change, depending on their aspect ratio. For studying gene circuits where multiple gene perturbations are required, it is possible to employ different color (i.e. wavelength) of light to address specific GNRs which absorb light at different wavelength (Fig. 1.15a).[47,49] This expends the scope of directly probing signaling pathways in live cells, which might provide critical insights in both cell biology and translational medicine. To test this concept, two different sequences of siRNA molecules were conjugated to two types of GNRs with separated absorption peak at 780nm and 650nm, respective. Therefore, by just utilizing two different wavelength of laser (λ_1 andλ_2 in Fig. 1.15a), a light-mediated method for dynamic reconfiguration of gene circuits has been suggested. For instance, gene expressions of p65 can be turn on or off, depending on laser irradiation (Fig. 1.15b and 15c). Moreover, the feasibility of time-dependent modulations of photonic gene circuits with corresponding downstream protein expression is tested by immunostanding. In the future, as inspiration of optogenetics, nanoplasmonic-genetics might be able to more precisely regulate multiple genes in living cells and small animals as well.

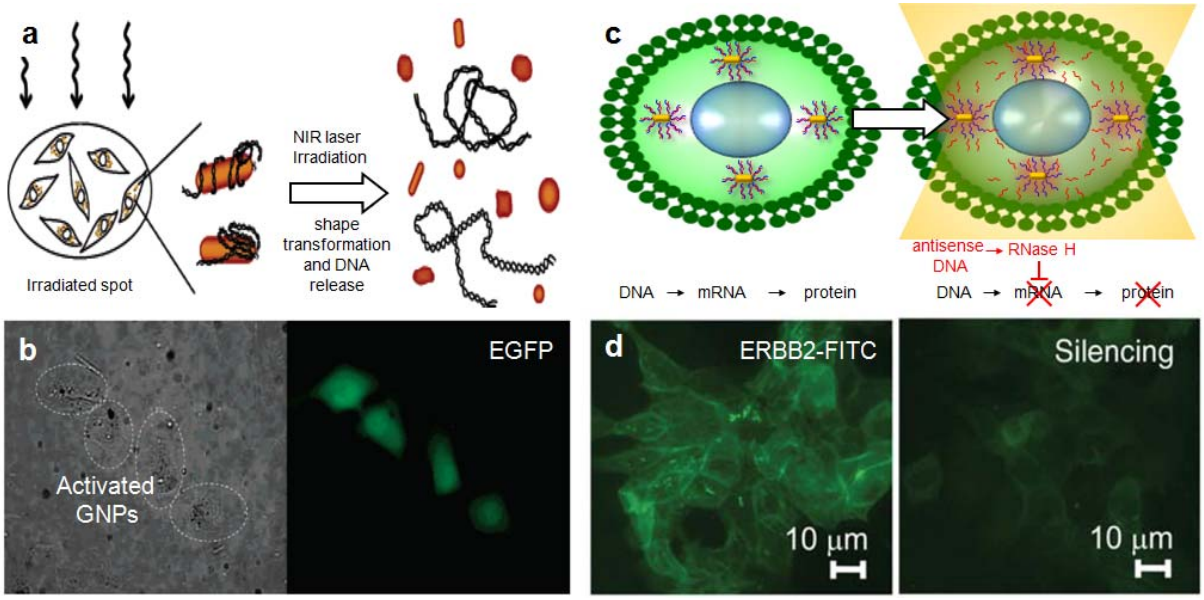

Figure 1.14 Light control of genetic materials release in live cells. **a,** Schematic illustration of remote control of DNA (with green fluorescence protein, GFP, gene) release in live cells by laser triggered shape transformation of GNRs.[97] **b,** Bright-field (left) and fluorescence (right) images of cells with high GFP expression (inside white circles) after laser irradiation. **c,** Schematic illustration of remote control of antisense DNA release in live cells by locally heating of GNRs. **d,** Fluorescence images of cells with (right) and without (left) irradiation.[22,49,98]

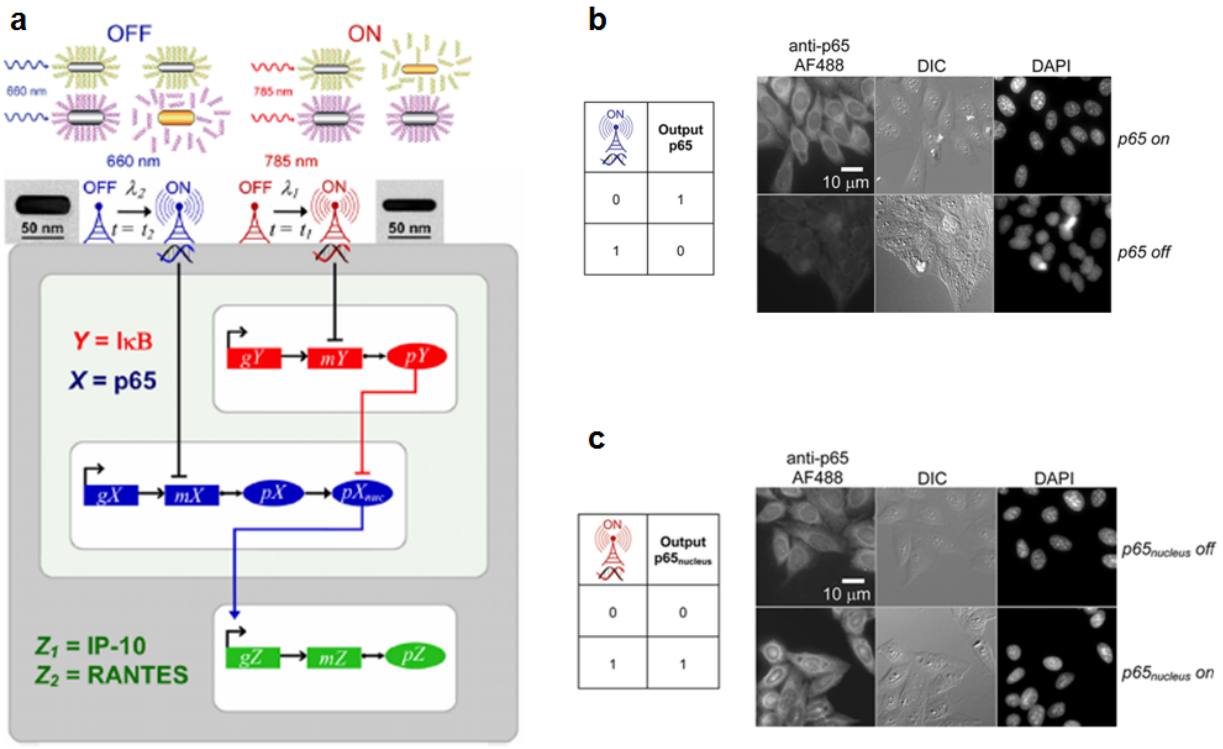

Figure 1.15 a, Controlling siRNA release for gene circuits manipulation by two optically addressable siRNA-Au nanoantennas (absorption at 660 and 785nm, respectively). Genes (gX, gY and gZ), mRNAs (mX,mY and mZ) and proteins (pX, pY and pZ) can be regulated by siRNA-Au nanoantennas with different color of incident light. **b,** Logic table for OFF-switch photonic gene circuit (left) and fluorescence cell imaging of OFF-switch photonic gene circuit (right). Lowering expression of p65 proteins was demonstrated by anti-p65-AF488 immunostaining. **c,** Logic table for ON-switch photonic gene circuit (left) and fluorescence cell imaging of ON-switched cells (right). Expression of p65 proteins was higher after ON-switch.[47,49]

1.8 Nanoplasmonic Trapping

Conventional optical tweezers, based on diffraction-limited laser spots, are not suitable for dealing with subwavelength objects (Fig. 1.16a). Two undesirable against the operation of trapping occurs when decreasing particle size: 1) the trapping potential well becomes shallower due to a decrease of the magnitude of the restoring force, and 2) the viscous drag is reduced causing a decrease of the trapped object damping. As the random thermal energy becomes more significant for smaller particles, a rule of thumb given by Ashkin et al. stipulates that the potential depth should be at least $10k_BT$ to compensate the specimen from escaping from the trap due to random stochastic Brownian motion.[54,55,99] In general, it is hard to trap particles with size smaller than wavelength of light by conventional optical tweezers.

The hot-spots that result from a tight plasmonic focus can overcome the limit of conventional optical trapping. The intense electric and magnetic field tailored by subwavelength focusing through LSPR can contribute to an force capable of stable nano-scale trapping, with a increased confinement and a deep depth of trapping potential (Fig. 1.16b).[55] The optical force and trapping potential can be calculated from focused fields through the Maxwell stress-tensor. Examples of trapping potential for a spherical particle are illustrated in Fig. 1.16a and 16b. Although the trapping force arises purely from an electromagnetic contribution of the field around the plasmonic structure, it is difficult to quantify the respective amount that will actually result in optical trapping rather than in photothermal heating. LSPR also cause an internal heating and dissipation of the particle surface energy through the medium, which result in convection and thermophoresis. It is therefore important to mention both components of optical forces and thermally induced forces.

Fig. 1.16c demonstrated a nanoplasmonic substrate for nanoparticles trapping. Two-dimensional arrays of gold nano-dots dimers with diameter of 134nm were fabricated by electron beam lithography on a glass substrate (left, Fig. 1.16c).[54] The gap in the middle of dimers supported a localized and intense hot-spot, confirmed by numerical simulations (right, Fig. 1.16c). In conventional optical trapping, a polystyrene bead (200 nm in diameter, refractive index of 1.6) was trapped by a focused laser beam and its trajectory demonstrated that the confinement was c.a. 800nm in diameter (left, Fig. 1.16d). On the other hand, in present of a hot-spots, supported by a gold nano-dots dimer, its moving in solution was confined in the scale of 100nm, smaller than diffraction limit of light (right, Fig. 1.16d). More recently, nanoplasmonic trapping has demonstrated on trapping of ~10nm dielectric particles, bacteria, and even single proteins. For example, plasmonic enhanced optical trapping of single bovine serum albumin (BSA) molecules has been demonstrated by using a double-nanohole in an Au film (Fig. 1.17a).[50] The hot-spot in the gap strongly trapped single protein and cased increase in reflective index (Fig. 1.17b). Because of strong optical force in the gap, protein unfolding was observed as well. High concentration, together with localization, makes nano-sized hot-spots a promising tool for trapping single particles and single molecules.[50,51,54,55]

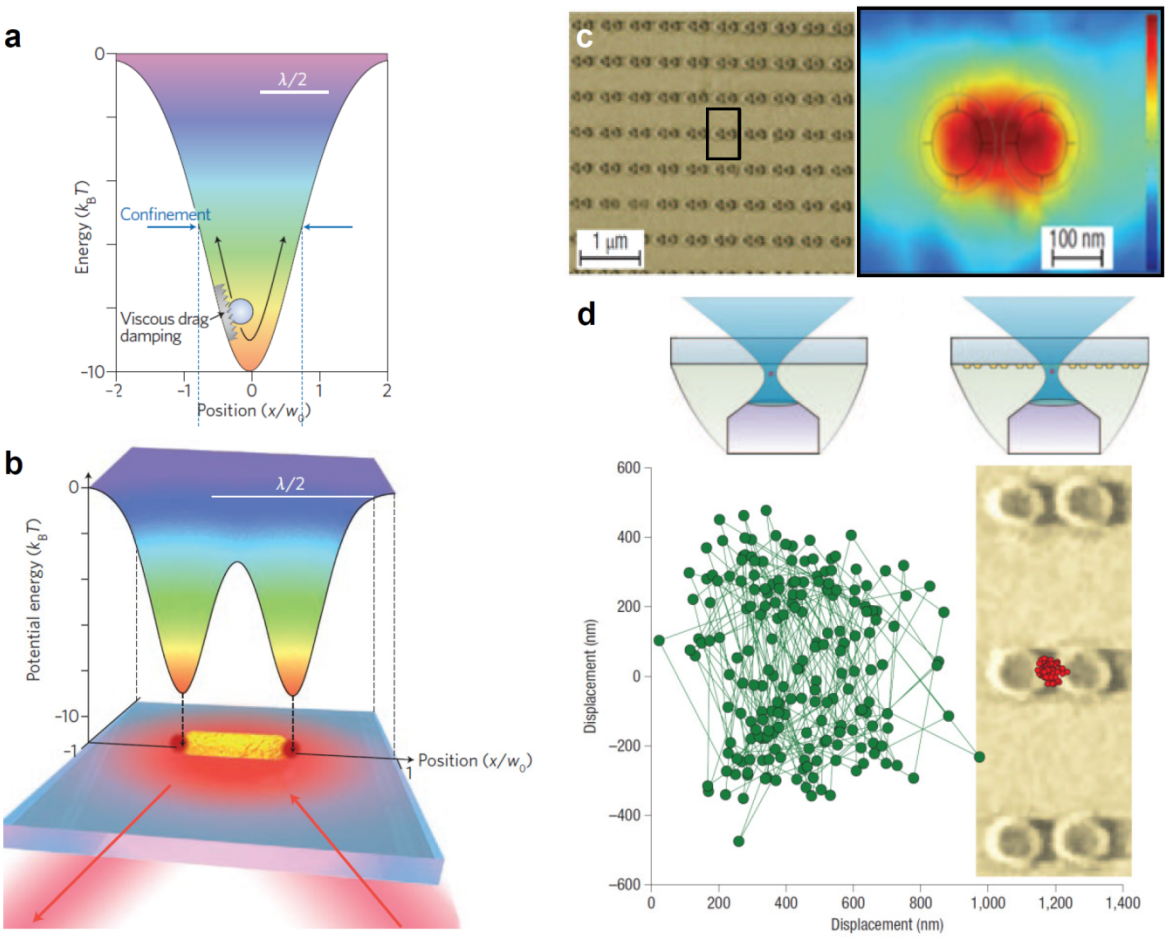

Figure 1.16 Conventional optical trapping versus nanoplasmonic trapping.[54,55] **a,** Conventional optical trapping potential for a polystyrene sphere. **b,** Nanoplasmonic trapping potential landscape resulting from a plasmonic gold nanorod. Note that the scale of confinement in nanoplasmonic trapping (i.e. ~$\lambda/4$) is smaller than that in conventional optical trapping (i.e. ~λ). **c,** Micrograph of nanodot pairs (left) and corresponding simulation of electromagnetic field intensity in near-fields. **d,** Trapping of single polystyrene spheres by conventional optical trapping (left, green line) and by a pair of plasmonic nanodots (right, red line).

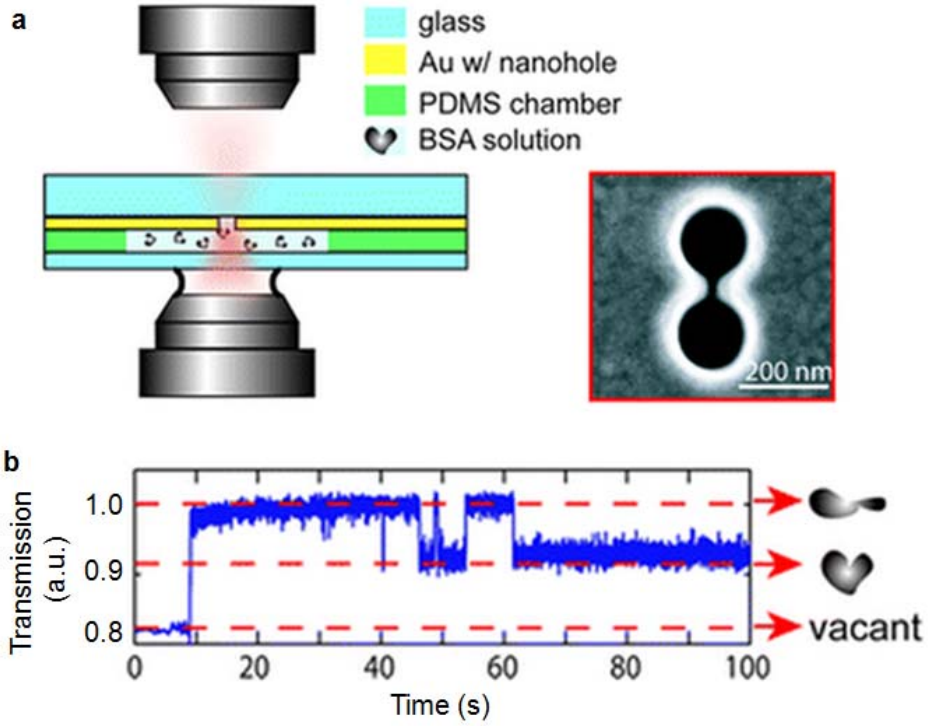

Figure 1.17 Single proteins trapping by plasmonic nanoholes. **a,** Schematic illustration of single bovine serum albumin trapping experiment (left) by double-nanohole structures (SEM image, right).[50] **b,** Time traces of light transmission demonstrated that plasmonic nanoholes can perform single-protein trapping. Nanoplasmonic force not only trapped a single nature protein (indicated by the middle arrow) but also induced unfolding (indicated by the top arrow).

References

1. Weiss, S. Fluorescence spectroscopy of single biomolecules. *Science* **283**, 1676-1683 (1999).

2. Michalet, X.*, et al.* Quantum dots for live cells, in vivo imaging, and diagnostics. *Science* **307**, 538-544 (2005).

3. Lippincott-Schwartz, J. & Patterson, G.H. Development and use of fluorescent protein markers in living cells. *Science* **300**, 87-91 (2003).

4. Lacoste, T.D.*, et al.* Ultrahigh-resolution multicolor colocalization of single fluorescent probes. *Proceedings of the National Academy of Sciences of the United States of America* **97**, 9461-9466 (2000).

5. Fu, C.C.*, et al.* Characterization and application of single fluorescent nanodiamonds as cellular biomarkers. *Proceedings of the National Academy of Sciences of the United States of America* **104**, 727-732 (2007).

6. Gao, X.H., Cui, Y.Y., Levenson, R.M., Chung, L.W.K. & Nie, S.M. In vivo cancer targeting and imaging with semiconductor quantum dots. *Nature Biotechnology* **22**, 969-976 (2004).

7. Yu, J., Xiao, J., Ren, X.J., Lao, K.Q. & Xie, X.S. Probing gene expression in live cells, one protein molecule at a time. *Science* **311**, 1600-1603 (2006).

8. El-Sayed, I.H., Huang, X.H. & El-Sayed, M.A. Selective laser photo-thermal therapy of epithelial carcinoma using anti-EGFR antibody conjugated gold nanoparticles. *Cancer Letters* **239**, 129-135 (2006).

9. Butt, H.J., Cappella, B. & Kappl, M. Force measurements with the atomic force microscope: Technique, interpretation and applications. *Surf. Sci. Rep.* **59**, 1-152 (2005).

10. Gradinaru, V.*, et al.* Molecular and Cellular Approaches for Diversifying and Extending Optogenetics. *Cell* **141**, 154-165 (2010).

11. Deisseroth, K. Optogenetics. *Nature Methods* **8**, 26-29 (2011).

12. Lu, Y., Liu, G.L., Kim, J., Mejia, Y.X. & Lee, L.P. Nanophotonic crescent moon structures with sharp edge for ultrasensitive biomolecular detection by local electromagnetic field enhancement effect. *Nano Letters* **5**, 119-124 (2005).

13. Ross, B.M. & Lee, L.P. Plasmon tuning and local field enhancement maximization of the nanocrescent. *Nanotechnology* **19**(2008).

14. Anker, J.N.*, et al.* Biosensing with plasmonic nanosensors. *Nature Materials* **7**, 442-453 (2008).

15. Lee, S.E. & Lee, L.P. Biomolecular plasmonics for quantitative biology and nanomedicine. *Current Opinion in Biotechnology* **21**, 489-497 (2010).

16. Li, Y., Jing, C., Zhang, L. & Long, Y.-T. Resonance scattering particles as biological nanosensors in vitro and in vivo. *Chemical Society Reviews* **41**, 632-642 (2012).

17. Hell, S.W. Far-field optical nanoscopy. *Science* **316**, 1153-1158 (2007).

18. Fernandez-Suarez, M. & Ting, A.Y. Fluorescent probes for super-resolution imaging in living cells. *Nat. Rev. Mol. Cell Biol.* **9**, 929-943 (2008).

19. Huang, B., Bates, M. & Zhuang, X.W. Super-Resolution Fluorescence Microscopy. in *Annual Review of Biochemistry*, Vol. 78 993-1016 (Annual Reviews, Palo Alto, 2009).

20. Lal, S., Link, S. & Halas, N.J. Nano-optics from sensing to waveguiding. *Nature Photonics* **1**, 641-648 (2007).

21. Zheng, Y.B., Kiraly, B., Weiss, P. & Huang, T. Molecular plasmonics for biology and nanomedicine. *Nanomedicine-Uk* **7**, 751-770 (2012).

22. Lee, S.E. & Lee, L.P. Nanoplasmonic gene regulation. *Current Opinion in Chemical Biology* **14**, 623-633 (2010).

23. Willets, K.A. & Van Duyne, R.P. Localized surface plasmon resonance spectroscopy and sensing. *Annu Rev Phys Chem* **58**, 267-297 (2007).

24. Willets, K.A. & Van Duyne, R.P. Localized surface plasmon resonance spectroscopy and sensing. in *Annu Rev Phys Chem*, Vol. 58 267-297 (Annual Reviews, Palo Alto, 2007).

25. Hartland, G.V. Optical Studies of Dynamics in Noble Metal Nanostructures. *Chemical Reviews* **111**, 3858-3887 (2011).

26. Halas, N.J., Lal, S., Chang, W.S., Link, S. & Nordlander, P. Plasmons in Strongly Coupled Metallic Nanostructures. *Chemical Reviews* **111**, 3913-3961 (2011).

27. Sonnichsen, C., Reinhard, B.M., Liphardt, J. & Alivisatos, A.P. A molecular ruler based on plasmon coupling of single gold and silver nanoparticles. *Nature Biotechnology* **23**, 741-745 (2005).

28. Liu, G.L.*, et al.* A nanoplasmonic molecular ruler for measuring nuclease activity and DNA footprinting. *Nature Nanotechnology* **1**, 47-52 (2006).

29. Choi, Y., Kang, T. & Lee, L.P. Plasmon Resonance Energy Transfer (PRET)-based Molecular Imaging of Cytochrome c in Living Cells. *Nano Letters* **9**, 85-90 (2009).

30. Zheng, Y.B.*, et al.* Active Molecular Plasmonics: Controlling Plasmon Resonances with Molecular Switches. *Nano Letters* **9**, 819-825 (2009).

31. Liu, G.L., Long, Y.-T., Choi, Y., Kang, T. & Lee, L.P. Quantized plasmon quenching dips nanospectroscopy via plasmon resonance energy transfer. *Nature Methods* **4**, 1015-1017 (2007).

32. Choi, Y., Park, Y., Kang, T. & Lee, L.P. Selective and sensitive detection of metal ions by plasmonic resonance energy transfer-based nanospectroscopy. *Nature Nanotechnology* **4**, 742-746 (2009).

33. Lakowicz, J.R.*, et al.* Plasmon-controlled fluorescence: a new paradigm in fluorescence spectroscopy. *Analyst* **133**, 1308-1346 (2008).

34. Aslan, K.*, et al.* Metal-enhanced fluorescence: an emerging tool in biotechnology. *Current Opinion in Biotechnology* **16**, 55-62 (2005).

35. Fort, E. & Gresillon, S. Surface enhanced fluorescence. *J Phys D Appl Phys* **41**(2008).

36. Cang, H.*, et al.* Probing the electromagnetic field of a 15-nanometre hotspot by single molecule imaging. *Nature* **469**, 385-+ (2011).

37. Kinkhabwala, A.*, et al.* Large single-molecule fluorescence enhancements produced by a bowtie nanoantenna. *Nature Photonics* **3**, 654-657 (2009).

38. Kennedy, D.C.*, et al.* Nanoscale Aggregation of Cellular beta(2)-Adrenergic Receptors Measured by Plasmonic Interactions of Functionalized Nanoparticles. *Acs Nano* **3**, 2329-2339 (2009).

39. Bailo, E. & Deckert, V. Tip-enhanced Raman spectroscopy of single RNA strands: Towards a novel direct-sequencing method. *Angewandte Chemie-International Edition* **47**, 1658-1661 (2008).

40. Drescher, D. & Kneipp, J. Nanomaterials in complex biological systems: insights from Raman spectroscopy. *Chemical Society Reviews* **41**, 5780-5799 (2012).

41. Kneipp, J., Kneipp, H. & Kneipp, K. SERS - a single-molecule and nanoscale tool for bioanalytics. *Chemical Society Reviews* **37**, 1052-1060 (2008).

42. Porter, M.D., Lipert, R.J., Siperko, L.M., Wang, G. & Narayanana, R. SERS as a bioassay platform: fundamentals, design, and applications. *Chemical Society Reviews* **37**, 1001-1011 (2008).

43. Kneipp, J., Kneipp, H., Wittig, B. & Kneipp, K. Following the Dynamics of pH in Endosomes of Live Cells with SERS Nanosensors. *Journal of Physical Chemistry C* **114**, 7421-7426 (2010).

44. Cho, H.S., Lee, B., Liu, G.L., Agarwal, A. & Lee, L.P. Label-free and highly sensitive biomolecular detection using SERS and electrokinetic preconcentration. *Lab Chip* **9**, 3360-3363 (2009).

45. Ando, J., Fujita, K., Smith, N.I. & Kawata, S. Dynamic SERS Imaging of Cellular Transport Pathways with Endocytosed Gold Nanoparticles. *Nano Letters* **11**, 5344-5348 (2011).

46. Qian, X.M.*, et al.* In vivo tumor targeting and spectroscopic detection with surface-enhanced Raman nanoparticle tags. *Nature Biotechnology* **26**, 83-90 (2008).

47. Anikeeva, P. & Deisseroth, K. Photothermal Genetic Engineering. *Acs Nano* **6**, 7548-7552 (2012).

48. Braun, G.B.*, et al.* Laser-Activated Gene Silencing via Gold Nanoshell-siRNA Conjugates. *ACS Nano* **3**, 2007-2015 (2009).

49. Lee, S.E.*, et al.* Photonic Gene Circuits by Optically Addressable siRNA-Au Nanoantennas. *Acs Nano* **6**, 7770-7780 (2012).

50. Pang, Y.J. & Gordon, R. Optical Trapping of a Single Protein. *Nano Letters* **12**, 402-406 (2012).

51. Righini, M.*, et al.* Nano-optical Trapping of Rayleigh Particles and Escherichia coli Bacteria with Resonant Optical Antennas. *Nano Letters* **9**, 3387-3391 (2009).

52. Branton, D.*, et al.* The potential and challenges of nanopore sequencing. *Nature Biotechnology* **26**, 1146-1153 (2008).

53. Venkatesan, B.M. & Bashir, R. Nanopore sensors for nucleic acid analysis. *Nature Nanotechnology* **6**, 615-624 (2011).

54. Grigorenko, A.N., Roberts, N.W., Dickinson, M.R. & Zhang, Y. Nanometric optical tweezers based on nanostructured substrates. *Nature Photonics* **2**, 365-370 (2008).

55. Juan, M.L., Righini, M. & Quidant, R. Plasmon nano-optical tweezers. *Nature Photonics* **5**, 349-356 (2011).

56. Thakor, A.S., Jokerst, J., Zavaleta, C., Massoud, T.F. & Gambhir, S.S. Gold Nanoparticles: A Revival in Precious Metal Administration to Patients. *Nano Letters* **11**, 4029-4036 (2011).

57. Wagner, F.E.*, et al.* Before striking gold in gold-ruby glass. *Nature* **407**, 691-692 (2000).

58. Ross, B.M. & Lee, L.P. Comparison of near- and far-field measures for plasmon resonance of metallic nanoparticles. *Opt Lett* **34**, 896-898 (2009).

59. Kam, Z. ABSORPTION AND SCATTERING OF LIGHT BY SMALL PARTICLES - BOHREN,C, HUFFMAN,DR. *Nature* **306**, 625-625 (1983).

60. Mayer, K.M. & Hafner, J.H. Localized Surface Plasmon Resonance Sensors. *Chemical*

Reviews **111**, 3828-3857 (2011).

61. Johnson, P.B. & Christy, R.W. OPTICAL CONSTANTS OF NOBLE METALS. *Phys Rev B* **6**, 4370-4379 (1972).

62. Link, S. & El-Sayed, M.A. Shape and size dependence of radiative, non-radiative and photothermal properties of gold nanocrystals. *Int. Rev. Phys. Chem.* **19**, 409-453 (2000).

63. Eustis, S. & El-Sayed, M.A. Why gold nanoparticles are more precious than pretty gold: Noble metal surface plasmon resonance and its enhancement of the radiative and nonradiative properties of nanocrystals of different shapes. *Chemical Society Reviews* **35**, 209-217 (2006).

64. Zijlstra, P., Chon, J.W.M. & Gu, M. Five-dimensional optical recording mediated by surface plasmons in gold nanorods. *Nature* **459**, 410-413 (2009).

65. Reinhard, B.M., Sheikholeslami, S., Mastroianni, A., Alivisatos, A.P. & Liphardt, J. Use of plasmon coupling to reveal the dynamics of DNA bending and cleavage by single EcoRV restriction enzymes. *Proceedings of the National Academy of Sciences of the United States of America* **104**, 2667-2672 (2007).

66. Ross, B.M., Wu, L.Y. & Lee, L.P. Omnidirectional 3D Nanoplasmonic Optical Antenna Array via Soft-Matter Transformation. *Nano Letters* **11**, 2590-2595 (2011).

67. Chi-Cheng, F.*, et al.* Bimetallic nanopetals for thousand-fold fluorescence enhancements. *Applied Physics Letters* **97**, 203101 (203103 pp.)-203101 (203103 pp.)203101 (203103 pp.) (2010).

68. Aubry, A.*, et al.* Plasmonic Light-Harvesting Devices over the Whole Visible Spectrum. *Nano Letters* **10**, 2574-2579 (2010).

69. Hentschel, M.*, et al.* Transition from Isolated to Collective Modes in Plasmonic Oligomers. *Nano Letters* **10**, 2721-2726 (2010).

70. Rong, G., Wang, H. & Reinhard, B.M. Insights from a Nanoparticle Minuet: Two-Dimensional Membrane Profiling through Silver Plasmon Ruler Tracking. *Nano Letters* **10**, 230-238 (2010).

71. Jun, Y.-W.*, et al.* Continuous imaging of plasmon rulers in live cells reveals early-stage caspase-3 activation at the single-molecule level. *Proceedings of the National Academy of Sciences of the United States of America* **106**, 17735-17740 (2009).

72. Anger, P., Bharadwaj, P. & Novotny, L. Enhancement and quenching of single-molecule fluorescence. *Physical Review Letters* **96**(2006).

73. Fu, C.-C.*, et al.* Tunable Nanowrinkles on Shape Memory Polymer Sheets. *Adv Mater* **21**, 4472-+ (2009).

74. Fu, C.C., *et al.* Bimetallic nanopetals for thousand-fold fluorescence enhancements. *Applied Physics Letters* **97**(2010).

75. Garcia-Parajo, M.F. Optical antennas focus in on biology. *Nature Photonics* **2**, 201-203 (2008).

76. Kawata, S., Inouye, Y. & Verma, P. Plasmonics for near-field nano-imaging and superlensing. *Nature Photonics* **3**, 388-394 (2009).

77. Kinkhabwala, A., *et al.* Large single-molecule fluorescence enhancements produced by a bowtie nanoantenna. *Nature Photonics* **3**, 654-657 (2009).

78. Sanchez, E.J., Novotny, L. & Xie, X.S. Near-field fluorescence microscopy based on two-photon excitation with metal tips. *Physical Review Letters* **82**, 4014-4017 (1999).

79. Levene, M.J., *et al.* Zero-mode waveguides for single-molecule analysis at high concentrations. *Science* **299**, 682-686 (2003).

80. Muhlschlegel, P., Eisler, H.J., Martin, O.J.F., Hecht, B. & Pohl, D.W. Resonant optical antennas. *Science* **308**, 1607-1609 (2005).

81. Nie, S.M. & Emery, S.R. Probing single molecules and single nanoparticles by surface-enhanced Raman scattering. *Science* **275**, 1102-1106 (1997).

82. Kneipp, K., *et al.* Single molecule detection using surface-enhanced Raman scattering (SERS). *Physical Review Letters* **78**, 1667-1670 (1997).

83. Huber, D.L., Manginell, R.P., Samara, M.A., Kim, B.I. & Bunker, B.C. Programmed adsorption and release of proteins in a microfluidic device. *Science* **301**, 352-354 (2003).

84. Lu, Y., Liu, G.L. & Lee, L.P. High-density silver nanoparticle film with temperature-controllable interparticle spacing for a tunable surface enhanced Raman scattering substrate. *Nano Letters* **5**, 5-9 (2005).

85. Wang, M., Jing, N., Chou, I.H., Cote, G.L. & Kameoka, J. An optofluidic device for surface enhanced Raman spectroscopy. *Lab Chip* **7**, 630-632 (2007).

86. Tong, L., Righini, M., Ujue Gonzalez, M., Quidant, R. & Kall, M. Optical aggregation of metal nanoparticles in a microfluidic channel for surface-enhanced Raman scattering analysis. *Lab Chip* **9**, 193-195 (2009).

87. Choi, D., Kang, T., Cho, H., Choi, Y. & Lee, L.P. Additional amplifications of SERS via an optofluidic CD-based platform. *Lab Chip* **9**, 239-243 (2009).

88. Liu, G.L. & Lee, L.P. Nanowell surface enhanced Raman scattering arrays fabricated by soft-lithography for label-free biomolecular detections in integrated microfluidics. *Applied Physics Letters* **87**(2005).

89. Hayazawa, N., Saito, Y. & Kawata, S. Detection and characterization of longitudinal field for tip-enhanced Raman spectroscopy. *Applied Physics Letters* **85**, 6239-6241 (2004).

90. Knoll, B. & Keilmann, F. Near-field probing of vibrational absorption for chemical microscopy. *Nature* **399**, 134-137 (1999).

91. Hartschuh, A., Sanchez, E.J., Xie, X.S. & Novotny, L. High-resolution near-field Raman microscopy of single-walled carbon nanotubes. *Physical Review Letters* **90**(2003).

92. Giljohann, D.A.*, et al.* Gold Nanoparticles for Biology and Medicine. *Angewandte Chemie-International Edition* **49**, 3280-3294 (2010).

93. Boisselier, E. & Astruc, D. Gold nanoparticles in nanomedicine: preparations, imaging, diagnostics, therapies and toxicity. *Chemical Society Reviews* **38**, 1759-1782 (2009).

94. Sperling, R.A., Rivera gil, P., Zhang, F., Zanella, M. & Parak, W.J. Biological applications of gold nanoparticles. *Chemical Society Reviews* **37**, 1896-1908 (2008).

95. Davis, M.E., Chen, Z. & Shin, D.M. Nanoparticle therapeutics: an emerging treatment modality for cancer. *Nature Reviews Drug Discovery* **7**, 771-782 (2008).

96. Govorov, A.O. & Richardson, H.H. Generating heat with metal nanoparticles. *Nano Today* **2**, 30-38 (2007).

97. Chen, C.C.*, et al.* DNA-gold nanorod conjugates for remote control of localized gene expression by near infrared irradiation. *Journal of the American Chemical Society* **128**, 3709-3715 (2006).

98. Lee, S.E., Liu, G.L., Kim, F. & Lee, L.P. Remote Optical Switch for Localized and Selective Control of Gene Interference. *Nano Letters* **9**, 562-570 (2009).

99. Grier, D.G. A revolution in optical manipulation. *Nature* **424**, 810-816 (2003).

CHAPTER 2

Nanoplasmonic Optoporation for Large-scale Precision Gene Regulation

Gene regulation is an important step in cell reprogramming both *in vitro* and *in vivo*.[1-3] Traditional methods for delivery of genetic materials are limited in terms of their spatial and temporal controllability.[3] Here, we accomplished a nanoplasmonic optoporation for large-scale precision gene regulation by creating transient nanopores on cell membrane with a remote near-infrared (NIR) light source. The biophysical and photothermal mechanism of gold nanoplasmonic particles allows us to create nanopores with diameter ranging from 10 to 70 nm.[4,5] After irradiation at laser pulse fluence of 2 mJ/cm^2, the time constant of pore resealing is about 30 min.[6-8] Centimetre-scale optoporation, together with single-cell level precision, is demonstrated by sequential molecular deliveries.[9,10] Finally, we demonstrated that siRNA-mediated gene regulation of stem cells. The efficiency is ~ 2-fold higher than conventional lipofection methods.

2.1 Introduction

Transcription factor transduction can convert somatic cells into induced pluripotent stem (iPS) or other cell types.[1,2] Reprogrammed cells, which contain the same genetic information as the original donor cells, hold great potential in disease modelling, drug screening, and transplantation therapies.[3] A critical step in these applications is to regulate the gene expression of targeted cells by introducing interference materials, such as nucleic acids, small molecules, and proteins.[1-3] Although common methods, including viral transduction, lipid- or polymer-mediated transfection, and electroporation, show robust large-scale delivery,[3,9,10] their spatial and temporal controllability are limited by the stochastic nature of bulk operations. By contrast, nanotechnological approaches may show improved controllability.

Nanowire injection, carbon nanomaterials, nanochannels, nanoblades, nano-optical ablation, and nanostructure-coated substrates have been developed for patterning deliveries, improving efficiency, and enhancing resolution to the single-cell level.[11-18] However, most nanomediated deliveries are difficult to apply to *in vivo* studies, which require long penetration depths across tissues.[11,14,15] Nano-optical ablation requires manual perturbation of individual cells, which limits their scope of throughput, by high magnification objective with extremely high energy (Fig. 2.1a).[18] In contrast, plasmonic nanoantennas, such as gold nanorods (GNRs), nanoshells, and nanocages, are promising materials to overcome this limitation due to localized photothermal effects (Fig. 2.1b).[19-23] Their absorption can be tuned to the NIR region, in which light can penetrate tissue as deep as 1 cm. Together with their low cytotoxicity and easy bioconjugation, nanoantennas could be ideal vectors for *in situ* transfection *in vitro* and *in vivo*.[5] However, their application has been hampered by poor understanding of the interactions between nanoplasmonic vectors and cell membranes.

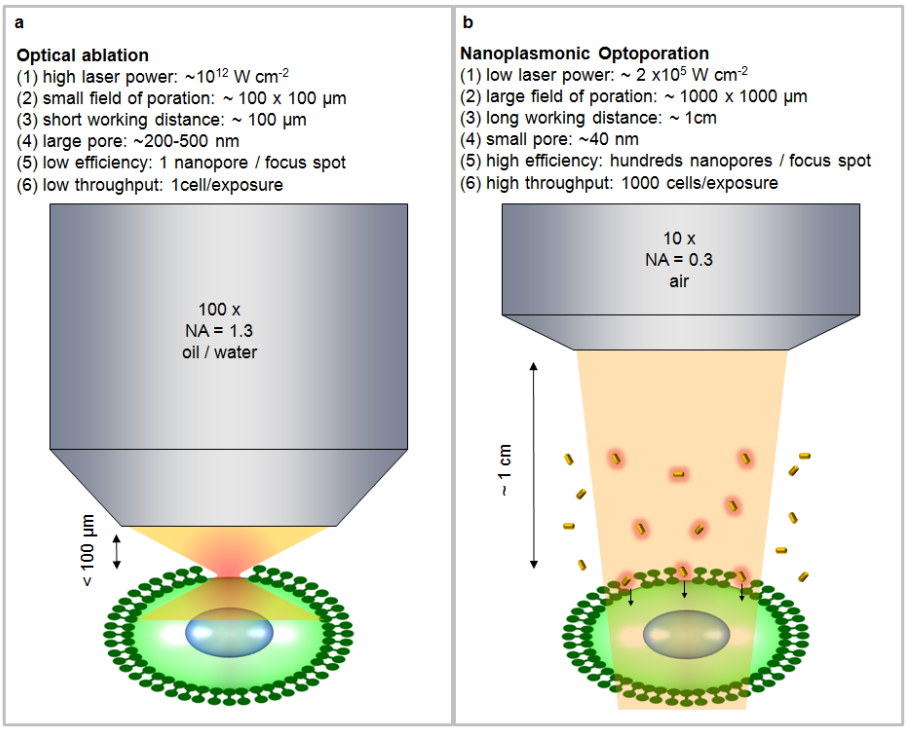

Figure 2.1 Schematic illustrations and comparison of optical ablation and nanoplasmonic optoporation. **a**, In optical ablation, a high magnification objective, with high N.A., is required to generate high power density in the focus spot. Well alignment between a diffraction limit focus spot (200 - 500nm in diameter) and cell membranes (~ 2 nm thickness) is necessary to create nanopores on membranes. **b,** In contrast, by leveraging the localized photothermal effect of nanoantennas, nanoplasmonic optoporation generates nanopores on cell membranes more efficiently, using a low magnification objective with low optical power.

In this study, we characterised nanoantenna-mediated transfection, optimized the optical energy for creating nanopores, and measured the nanopore lifetime by fluorescence microscopy. We proposed a mechanism of how photothermal GNRs melt and penetrate cytoplasmic membranes, based on scanning electron microscopy (SEM) results and finite-element (FE) simulations.[24,25] Through this method, various small molecules, including organic dyes, were delivered to mouse embryonic fibroblasts (MEFs) with single-cell level controllability and tissue-scale expendability.[11] Highly efficient light-controlled gene silencing was obtained in mouse embryonic stem (MES) cells.[10,26,27] This platform holds great potential for remotely controlling the transfection of transcription factors and studying cell reprogramming at the single-cell level (Fig. 2.2).[3,28]

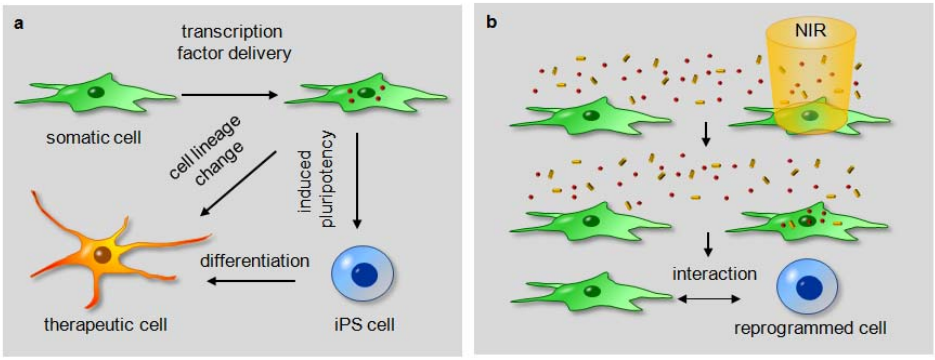

Figure 2.2 Nanoplasmonic optoporation for cell reprogramming. **a**, Schematic illustration of cell reprogramming. Through the delivery of well-defined factors (red dots), somatic cells can be reprogrammed to iPS cells or cells of other lineages. Owing to their similar properties to embryonic stem cells, iPS cells are able to differentiate into various cell types for therapies. **b**, NIR-absorbed plasmonic nanoantennas (gold nanorods, GNRs, yellow dots) are promising vectors for the spatial and temporal control of molecular delivery for cell reprogramming.

2.2 Characterization of Nanopores

Cells were cultured on glass or plastic slides with molecules (dyes or RNA) and GNRs (39 nm long, 10 nm wide) suspended in medium (Fig. 2.3a). A laser scanning microscope was equipped with pulse laser (140 fs pulse width) operating at 800 nm, matched with the surface plasmon resonance (SPR) of GNRs (Fig. 2.3b).[4,5] The sample was excited through an air objective lens (10x, N.A. 0.3) with a working distance of 1 cm and a large (1 mm^2) irradiation field (Fig. 2.3c and 2.3d). Typically, laser with single pulse fluence of 2 mJ/cm^2 was used to activate nanoantenna-mediated cell poration and transfection with a total exposure time of 1 min.

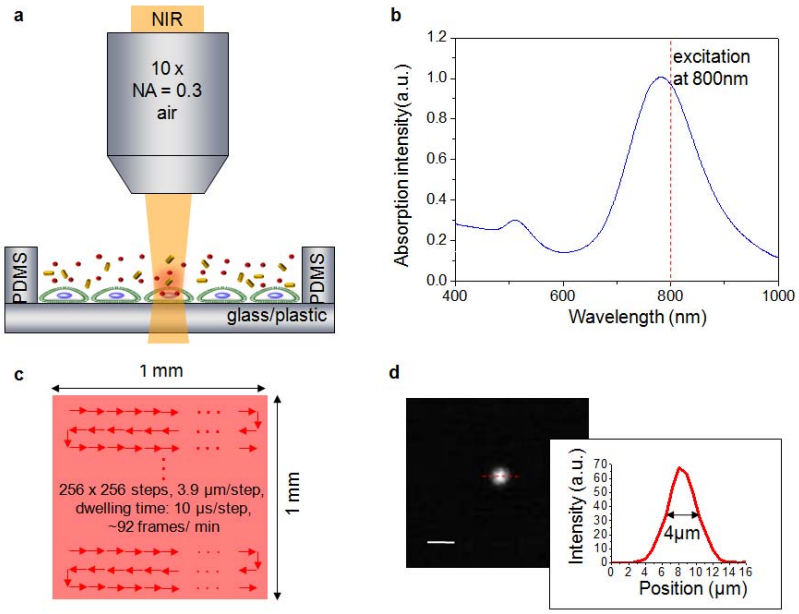

Figure 2.3 **a**, Cell membrane-impermeable dyes (propidium iodide, PI) and GNRs were seeding around MEFs. **b**, The absorption spectrum of GNRs with SPR peak at 790 nm where the wavelength of excitation laser, 800 nm, is matched. **c**, The illustration of a large scale of uniform excitation field generated by a laser scanning microscopy. The step size is close to the size of laser spot(see below). **d,** A confocal scanning image of a 20-nm fluorescent nanosphere dispersed on a bare glass substrate. The inset shows the intensity profile of the fluorescence image along the dashed line drawn in **c.** The full width at half maximum (FWHM) of the peak is 4 µm, corresponding to the diameter of the focused laser spotin our microscope. The scale bar in **d** is 10 µm.

Optical energy was optimized to achieve high delivery efficiency with low cell damage (Fig. 2.4 and 2.5). Cell membrane-impermeable dyes (propidium iodide, PI, and red nuclear DNA-staining fluorophores) and GNRs were seeding around MEFs. After irradiation by laser scanning, red dyes were taken up by porated cells via nanopores.[10] After cell recovery in an incubator for 1 hour, cell viability was determined by standard calcein AM staining (green fluorescence, staining only live cells). Under the optimal condition (Fig. 2.4a, middle panel), after extracellular molecule uptake, cells should recover by resealing nanopores on their membranes. At a laser pulse fluence of 2 mJ/cm^2, about half of the cells exhibited red dye uptake. Most cells emitted bright green fluorescence, indicating no significant loss in viability (Fig. 2.4b). Without irradiation, introduction of GNRs did not lead to red dye uptake or affect cell viability (Fig. 2.4b, left panel). At 4 mJ/cm^2, no calcein AM activity and a dramatic change in cell morphology were seen, which suggested that overexposure caused serious cell damage (Fig. 2.4b, right panel, and Fig. 2.5a).[29] Because dead cells cannot heal membranes, saturation of PI-DNA binding resulted in very bright red fluorescence (>10-times higher than with 2 mJ/cm^2 fluence). The control results confirmed that molecular delivery was specifically triggered by laser-antenna interactions (or plasmonic effects). In the absence of GNRs, irradiated cells did not take up any

red dye (Fig. 2.5b). The optimal energy for triggering nanoantenna-mediated delivery was ~2 mJ/cm^2, at which approximately half of the cells had extracellular molecule uptake without loss of viability (Fig. 2.4c).

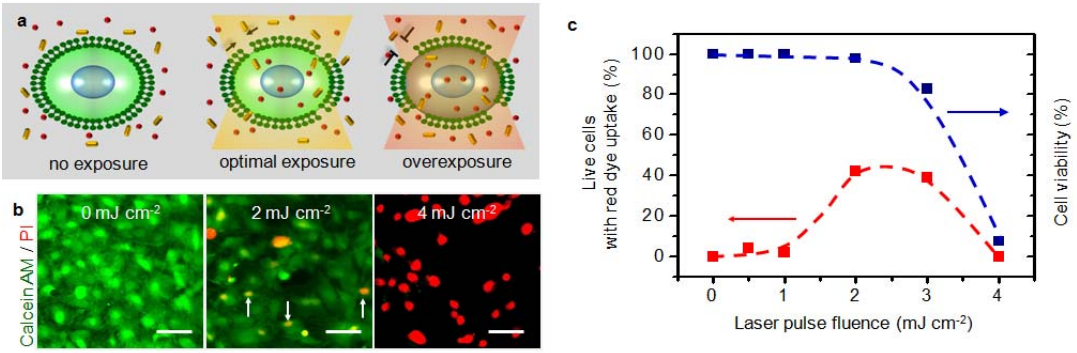

Figure 2.4 **a**, Schematic illustration of the characterization of optimal energy for nanoplasmonic optoporation. GNRs (yellow dots) and dyes (red dots) were seeded in medium with MEFs. Without laser exposure, cells showed no dye uptake and remained alive, as indicated by their strong interactions with calcein AM (green in cytoplasm). Under the optimal condition, the red dye uptake and positive calcein AM signal implied that nanopores were generated and could reseal (arrows) afterward. Cells lost their recovery ability and died (negative in calcein AM staining) when overexposed to laser. **b**, Corresponding fluorescence images of MEFs after exposure to different laser energies. **c**, Plot of live cells with red dye uptake and cell viability as a function of laser pulse fluence. Optimal energy is ~2 mJ/cm^2. The scale bars in **d** are 100 μm.

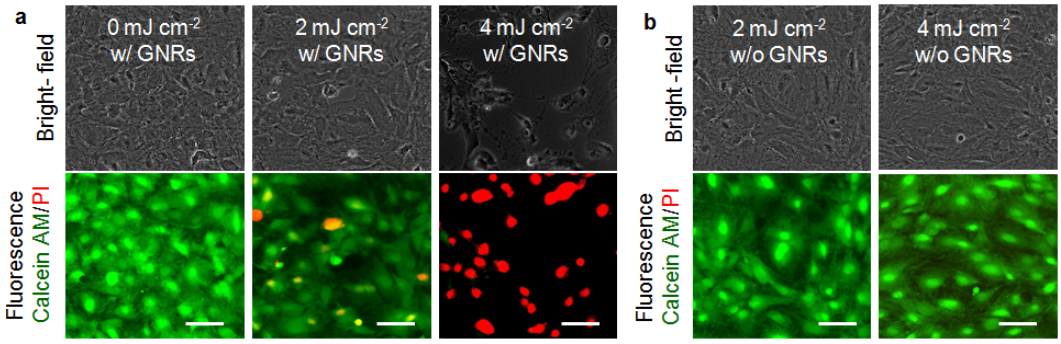

Figure 2.5 Fibroblasts with and without nanoplasmonic poration. **a,** Bright-field and fluorescence images of fibroblasts after being irradiated by different optical energy. The green (Calcien AM) and red channel (PI) represent live cells and cells with red dye molecules uptake respectively . Dramatic changes on cell morphology show up after exposed under 4 mJ cm^{-2} of laser pulse fluence. **b,** Bright-field and fluorescence images of post-irradiated cells without GNRs incubating. Cell are alive and no sign of PI uptake.

To inspect the nanopore geometries, we obtained SEM images of fixed cells, which cannot perform pore resealing before and after nanoplasmonic poration (Fig. 2.6 and 2.7).[13] Nanopores displayed two specific populations: smaller nanopores (~40 nm diameter; red arrows in Fig. 2.6a) and larger nanopores (~100 nm diameter; blue arrows in Fig. 2.6a). All nanopores were about two orders of magnitude smaller than the laser spot size (4 μm). A bimodal size distribution was observed (Fig. 2.6b), with the major population (73%, red line) showing a peak centred at 40 nm (range: 10–70 nm) and the minor population (27%, blue line) centred at 105 nm (range: 85–125 nm). Untreated samples showed no sign of nanopore formation on the cytoplasmic membranes (Fig. 2.7). We hypothesized that smaller pores were created by nanorods that penetrated the membrane with large entry angle (φ) between the long rod axis and membrane (Fig. 2.6b, left inset). At the contact points, the rod-shape particles seemed to orient vertically to the membrane to reduce the total membrane elastic energy.[24,25] The rotational and longitudinal diffusion of nanorods in the liquid-membrane interface might contribute to the round, rather than rod, shape of the nanopores. Existence of larger pores might allow GNRs to enter the membranes at relatively smaller angles φ (Fig. 2.6b, right inset). In this case, the GNRs are parallel to the electric field and can absorb more energy.[4,5] A larger contact area with the membrane could generate bigger pores.

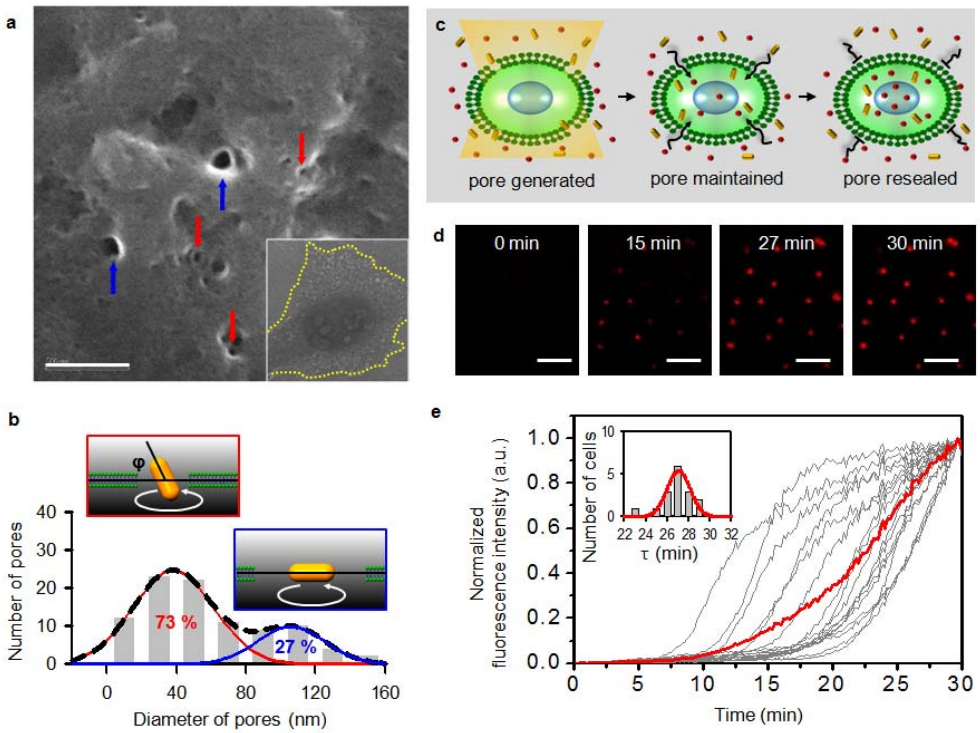

Figure 2.6 Characterization of nanopores and the mechanism of nanopore formation. **a**, An SEM image of single nanopores on a cell membrane. Blue and red arrows indicate large and small pores, respectively. Inset shows corresponding images with a large-scale view of the cell. Yellow dashed line shows the cell contour. **b**, Histograms of the nanopore diameter. Blue and red lines indicate the populations of large and small pores, respectively. Insets show possible pathways of how NIR-absorbed hot GNRs penetrate cytoplasmic membranes. **c**, Schematic illustration of nanopore lifetime measurements. Laser irradiation was performed and nanopores were generated at time zero. Dyes were transported via transient nanopores until they were resealed. **d**, Time-dependent confocal fluorescence images of MEFs with dynamic dye uptake. **e**, Fluorescence trajectories (grey lines) recorded from single cells with averaged intensity (the red line). Inset shows the histograms of time (τ) required to reach 90% of the maximum intensity. The scale bar in **a** is 500 nm. Scale bars in **a** and **d** are 500 nm and 100 μm, respectively.

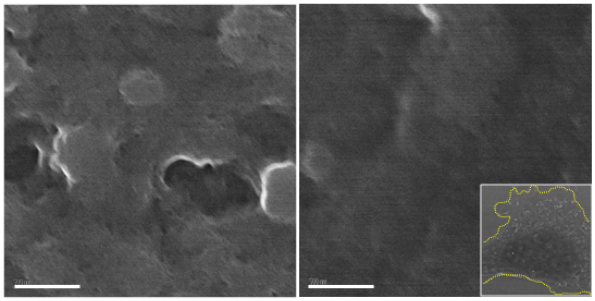

Figure 2.7 Two SEM images of cell plasma membranes without nanoplasmonic poration. No obvious pores with sharp edges can be observed. The inset on right-bottom shows the same cell images with large –scale of view. The yellow dash line indicates contour of a cell. The scale bars are 500 nm.

After they were irradiated at time zero, MEFs started to absorb PI dye via nanopores. The amount of transported dye was monitored by tracking the fluorescence intensity change due to dye-nuclear DNA binding (Fig. 2.6c).[10] Once the pores had resealed, extracellular dye transport was blocked, and the fluorescence intensity increase was stopped. The dye uptake dynamics are shown as a time series of confocal scanning fluorescence images (Fig. 2.6d). At 15 min after activation, fluorescent emissions were observed from single cells. The cells subsequently became brighter, and all cells reached steady state fluorescence within 30 min. Under the optimal irradiation condition (i.e., 2 mJ/cm^2), the intracellular dye did not reach saturation with DNA binding. The fluorescence intensity trajectories and corresponding lifetime histograms indicated that nanopore resealing occurred within 25 to 29 min (Fig. 2.6e). The average nanopore lifetime (and, thus, cell recovery time) was approximately 27 min, consistent with the pore-opening time obtained by injecting hot gold nanoparticles through artificial phospholipid membranes.[6] Therefore, a single delivery can be completed <1 hour, which is ~5-times faster than commercial lipofection.

2.3 The Mechanism of Nanopore Formation

From the nanopore characterization and three-dimensional FE simulation results, we proposed a mechanism of plasmonic nanoantenna-mediated cell poration (Fig. 2.8). First, extracellular molecules and GNRs diffuse outside the cytoplasmic membrane. Under laser irradiation at a pulse fluence of 2 mJ/cm^2, GNRs locally enhance the EM field ~10-fold and strongly harvest light via SPR absorption (Fig. 2.8a and 2.8b).[5] Absorbed energy is converted to thermal energy and dissipated via electron-phonon and phonon-phonon coupling.[4,5] The process usually takes ~10 – 100 ps and increases the local temperature to ~71 °C, which is above the phospholipid membrane gel-fluidic transition temperature (~40–50 °C, Fig. 2.8c).[6-8] Transient heating, along with less than 5-nm-length heat dissipation, causes the lipid bilayers to melt locally (Fig. 2.8d and 2.8e).[6,7] To decrease the total membrane elastic energy, GNRs are wrapped by fluidic membranes and tend to rotate vertically (Fig. 2.8e). Most of the hot rod-like nanoparticles penetrate the membrane through tip rotation and create round nanopores. Finally, the nanopores are resealed after ~30 min.

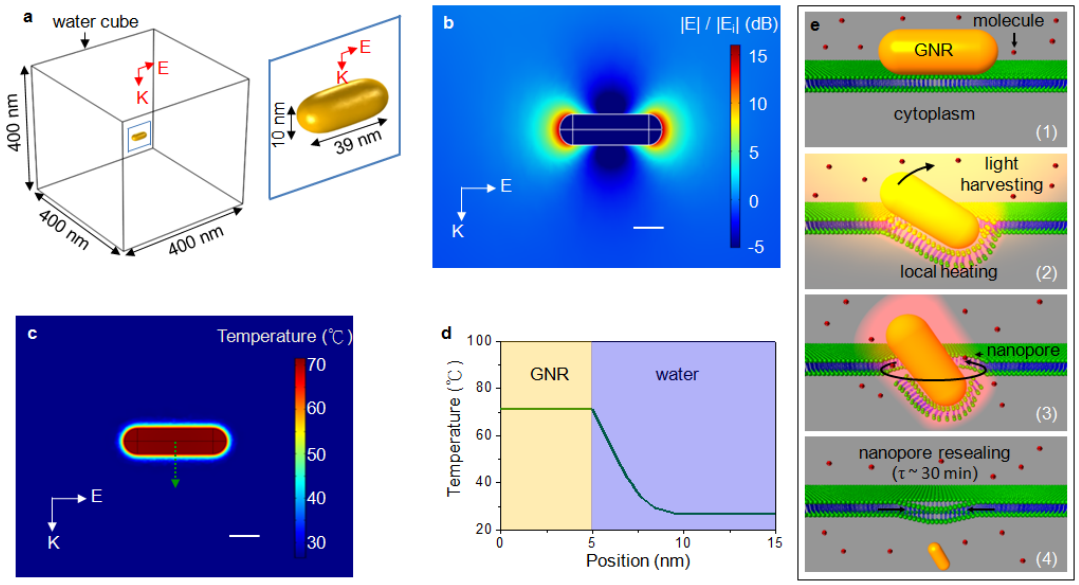

Figure 2.8 Finite element simulation of local field enhancement and photothermal conversion of GNRs. **a,** A 3D model of a GNR in the middle of water cube with EM field irradiated. The inset shows an enlarged view of the GNR in the model. **b,** Cross-sectional view of electric field amplitude surrounding a GNR at laser pulse fluence of 2 mJ cm^{-2}. **c,** Cross-sectional view of surface temperature of GNRs 10ps after irradiation at laser pulse fluence of 2 mJ cm^{-2}. **d,** The temperature profile, along the green arrow drawn in **c**, shows heat dispassion between the GNR (yellow block) and water (blue block) interface. The temperature of water drops to its background value within 5nm away from the surface of GNR. **e**, Schematic illustration of the mechanism of nanopore formation caused by tip rotation of photothermal a GNR on a local melted membrane. The scale bars in **b** and **c** are 10nm.

2.4 Light-patterned Multi-molecular Deliveries with Single-cell Controllability

To verify nanopore resealing, we tested the sequential delivery of different materials to cells. Red and blue dyes were delivered to two adjacent groups of MEFs, defined by patterns of light (Fig. 2.9a). Red dye (PI) and GNRs were incubated with cells, half of which were exposed to laser to trigger red-dye uptake. After incubation for 1 hour for pore resealing, free GNRs and red dyes were replaced with freshly prepared GNRs and blue dyes (Sytox Blue). The other half of the cell sample was exposed to laser for delivery of blue dye. Nonabsorbed materials were washed away after incubation for 1 hour. Both cell samples were separated by a nonirradiated margin of 50 um (i.e., approximate size of single attached MEFs). Red and blue dyes were specifically and selectively delivered to either side of the cells (Fig. 2.9b). The lack of cross-contamination indicated that the nanopores generated at the first treatment had resealed completely. The clear boundaries between the centre margin region and two laser-exposed areas indicated high spatial controllability. Single- or sub-cellular resolution was achieved because the laser spot size (4 μm),

which was the dominant factor, was an order of magnitude smaller than the cells.[18]

We demonstrated that the delivery region can be easily expanded to the tissue scale. Red dye (PI) and GNRs were applied to a large sheet of nearly confluent MEFs (Fig. 2.9c and 2.9d). A large irradiation pattern (~1 cm^2) was achieved by moving an x-y stage over a 6 × 4 array (0.8 × 0.8 mm element size, 0.4 mm spacing). Figure 2.9d shows a large fluorescence image overlapped by hundreds of small images. The inset is an enlarged view of a single element overlapped with its corresponding bright-field image. When cells were cultured in ~1 cm^2 of the field, only laser-exposed areas took up the extracellular molecules. In addition to well-defined delivery, there was no significant decrease in efficiency over the entire area. This result is difficult to achieve by traditional optical poration, which requires a high magnification objective (small irradiation field) and sophisticated technology to align the laser spot on the cytoplasmic membrane.[18] The high throughput of our method outcompetes most nanomediated delivery systems.[11,14] Furthermore, cells could be porated multiple times for delivery of various materials (Fig. 2.10).

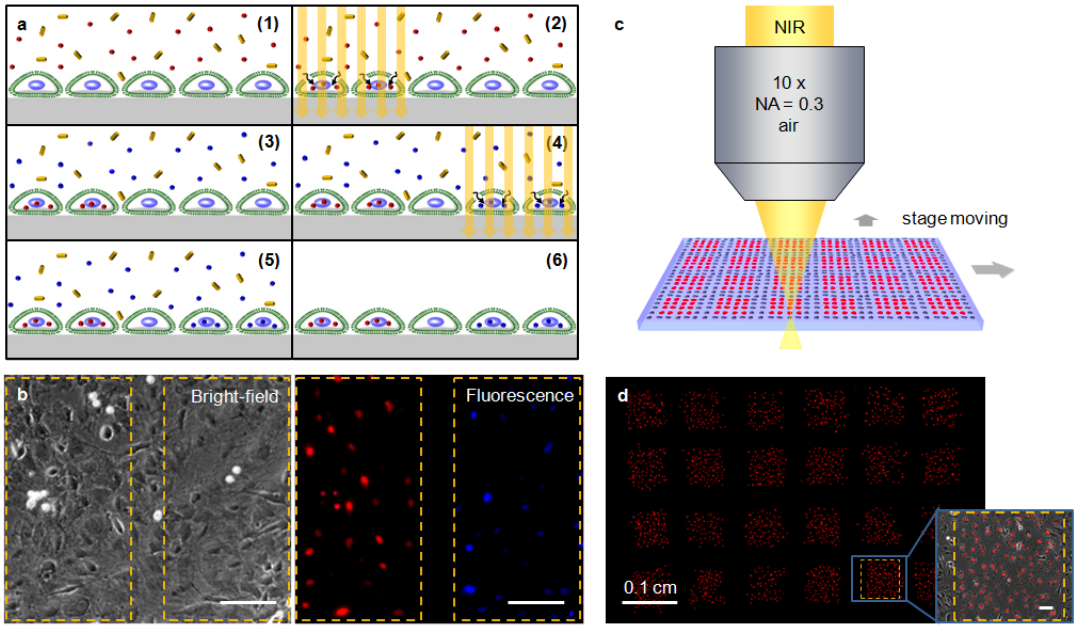

Figure 2.9 Light-patterned multimolecular deliveries with single-cell controllability and tissue-scale expendability. **a**, Schematic illustrations of the delivery of red and blue dyes to each side of MEFs mediated by nanoplasmonic optoporation. **b**, Images of treated cells under bright-field (left) and fluorescence (right) microscopy. Yellow dashed lines indicate two irradiation windows with a gap of 50 μm. No significant crosstalk was detected between the two deliveries. **c**, Schematic illustration of a large irradiation pattern (~ 1 cm^2) in which red dye delivery is controlled by a stage. The margins between elements are not irradiated. **d**, Large fluorescence image of cells with dye uptake, defined by light patterns. Inset shows an enlarged view of a fluorescence image overlapped with the corresponding bright-field image. Yellow dashed line indicates a single irradiation element. Scale bars in **b** and inset of **d** are 100 μm.

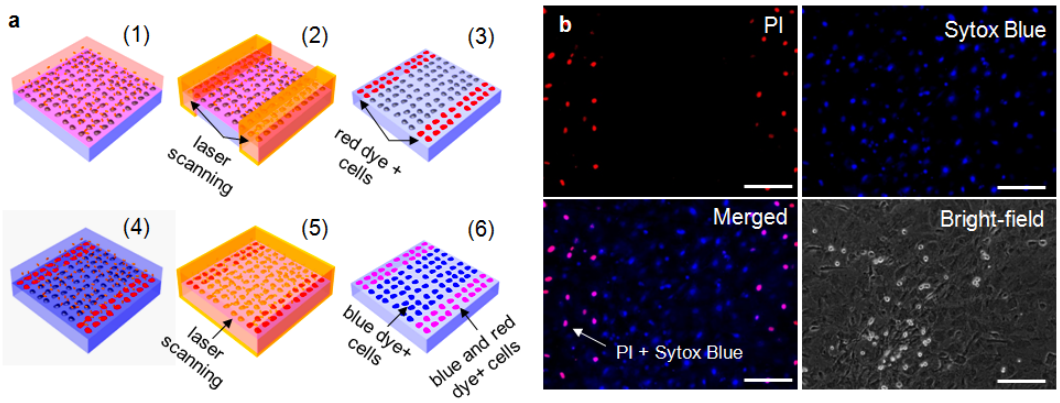

Figure 2.10 Multi-times delivery by nano-plasmonic poration. **a,** Schematic illustrations of delivery of red and blue molecules (PI and Sytox Blue, respective) controlled by laser scanner. **b,** Fluorescence and bright-field images of cell after molecular delivery. Cells on the edges (pink dots) show both red and blue dyes uptake, demonstrating the capability of multiple delivery on the same group of cells. The scale bars in **b** are 100 μm.

2.5 Nanoplasmonic Optoporation-mediated RNA Delivery for Gene Regulation

Delivery of gene materials was evaluated in stem cells. The green fluorescence protein (GFP) gene was inserted into the Nanog locus of MES cells (TNG cell line).[27] TNG cells were transfected with egfp siRNA by nanoantenna-mediated delivery to trigger the RNA-induced silencing complex (RISC) and downregulate Nanog-GFP expression.[9,10,22,26] Nanog is a key transcriptional factor involved in cell fate determination. Natural fluctuations in Nanog expression play a pivotal role in stem cell development, either maintaining pluripotency or commitment to differentiation, as reflected in the variations in Nanog-GFP expression in TNG stem cells (Fig. 2.11a and 2.11b).[27] Most of the population (79%; Fig. 2.11a, blue arrows; Fig. 2.11b, blue line) with high Nanog expression tended to stabilize in the pluripotent state. The remaining 21% with low-level Nanog expression (Fig. 2.11a, red arrows; Fig. 2.11b, red line) might have a greater chance to differentiate.[27] At 1 day after nanoantenna-mediated siRNA delivery, the population of high Nanog-GFP expression cells dropped from 79% to 22% (Fig. 2.11c and 2.11d), indicating successful degradation of corresponding mRNAs (inset of Fig. 2.11d). This efficiency was higher than that of standard liposome-mediated transfection, in which 48% of the cell population remained at a high Nanog-GFP expression level (Fig. 2.12a). Negative controls demonstrated the specificity of our approach for posttranscriptional gene regulation (Fig. 2.12b and 2.12c). In the absence of GNRs or laser exposure, no significant sign of gene silencing was detected.

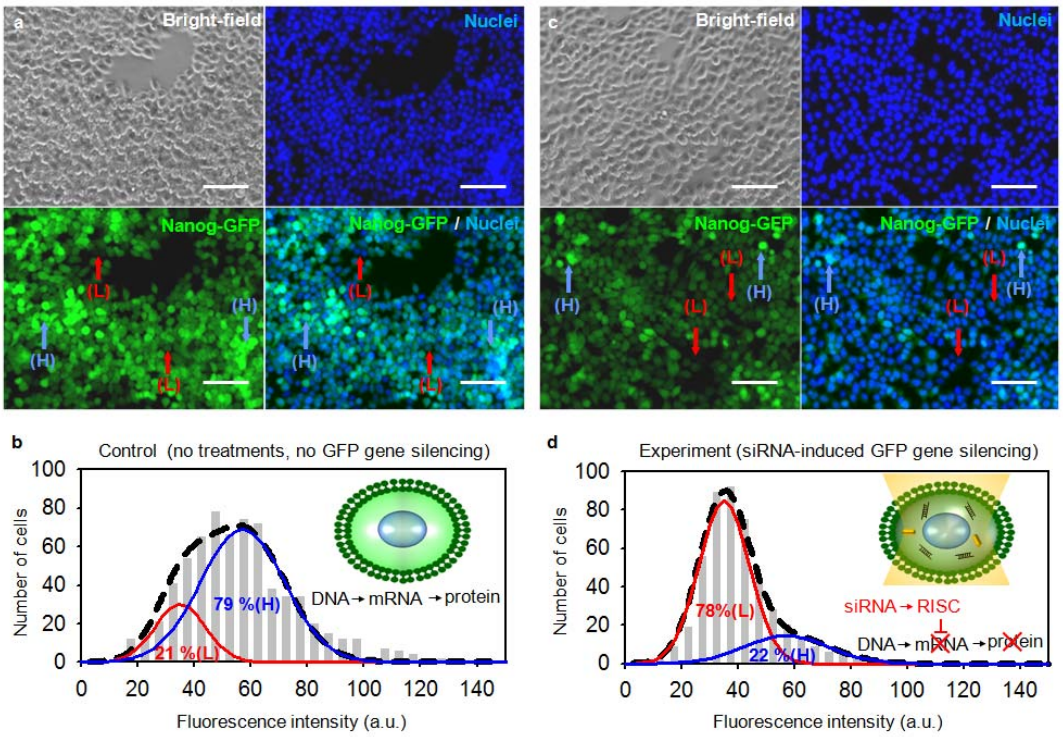

Figure 2.11 Nanoplasmonic optoporation-mediated RNA delivery for gene regulation. **a**, Bright-field and fluorescence images of Nanog-GFP-expressing stem cells in absence of siRNA delivery. Blue and red arrows indicate cells with high (H) and low (L) Nanog-GFP expression levels, respectively. **b**, Histograms of the green fluorescence intensities of single cells. Blue and red lines indicate cell populations of high (H) and low (L) Nanog-GFP expression levels, respectively. Inset shows an illustration of a stem cell with strong green fluorescence in the absence of GFP gene silencing. **c**, Bright-field and fluorescence images of stem cells at 1 day after transfection of siRNA, mediated by nanoplasmonic optoporation. **d**, Histograms of the green fluorescence intensities of cells with siRNA delivery. The cell population of high GFP expression (H) dropped to 22%. Inset shows an illustration of a stem cell with weak green fluorescence due to downregulation of mRNA and GFP expressions induced by interactions between siRNA and the RISC. Scale bars in **a** and **c** are 100 μm.

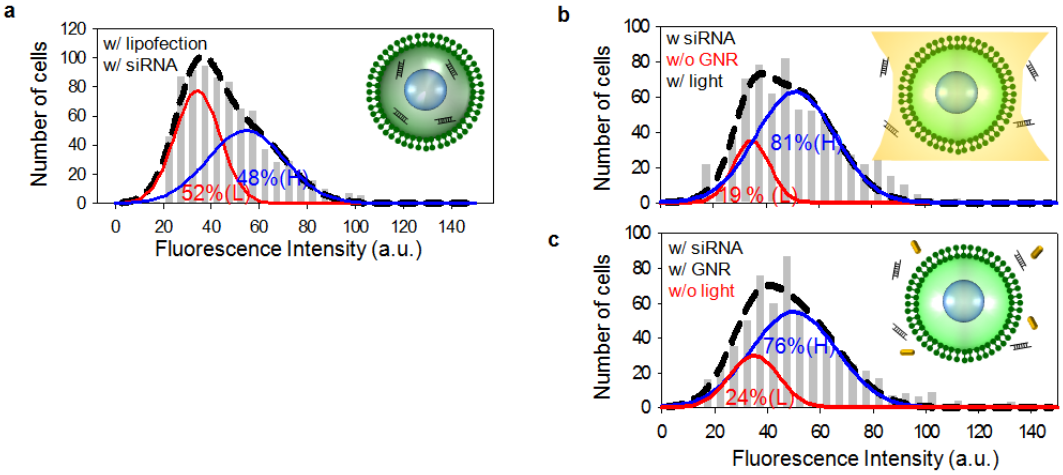

Figure 2.12 Controls of siRNA gene silencing experiments. **a,** The fluorescence intensity histograms of TNG stem cells after transfection of siRNAs by Lipofectamine ®. **b,** The histograms of post-irradiation TNG stem cells with siRNAs but without GNRs incubation. **c,** The histograms of TNG stem cells with siRNAs and GNRs incubation but without irradiation. Note that comparing with the histogram of cells without any treatment no significant GFP-silencing shown on **b** and **c**.

2.6 Conclusions and Outlook

We have characterized the properties of plasmonic nanoantennas as vectors for cellular delivery and transfection. Nanopores generated on membranes showed several unique features, including NIR-GNRs-specific triggering and nanometre-scale perturbation, which reduce safety concerns of further applications in tissue.[5] Small molecules and RNA materials were delivered to two important cell lines in cellular reprogramming (i.e., MEFs and MES cells). Nanoantenna-mediated delivery has the advantages of controllability at the single-cell level and tissue-scale expendability. Future studies of *in vivo* transfection should examine the ability of the current setup to target cells with surface-functionalized nanoantennas specifically and to trigger deliveries in deep tissue remotely. Large-scale light-controlled gene regulation combined with nanoplasmonic detection (e.g., surface-enhanced Raman scattering and metal-enhanced fluorescence) make NIR-absorbing nanoantennas a promising approach for *in situ* transfection and real-time monitoring of cell reprogramming *in vitro* and *in vivo*.[9,28,30]

Methods

Preparation of GNR and dye samples. To remove excess cetyltrimethylammonium bromide surfactant, 100 µL of GNR stock solution (40 µg/mL in water, SPR peak at 790 nm; Nanopartz) was resuspended in 1 mL of nuclease-free water. After centrifugation at 5000 rpm for 10 min (206D; Deville), the pellet (100 µL) was transferred and resuspended in 0.9 mL of poration

medium (phenol red-free DMEM medium supplemented with 10% FBS; Gibco) to a final concentration of 4 μg/mL (or 5×10^{10} particles/mL).[20,21] Then, PI (Sigma) and SYTOX Blue (5 mM solution in DMSO; Invitrogen) were added to the samples to 100 μM and 10 μM, respectively.

Nanoantenna-mediated dye delivery to MEFs. Homemade plates were precoated with fibronectin (Sigma), and MEFs were cultured on the plates in phenol red-free DMEM medium (Gibco) supplemented with 10% FBS (Gibco) and 1% penicillin/streptomycin (Invitrogen). The plates were constructed with two components: a standard microscope slide (5 × 7.6 × 0.1 cm; Fisher) and a 0.5-cm-thick cured PDMS (Sylgard) cut with two hollow wells (2.5 × 3 cm; 0.5 cm gap between wells) attached to the top of the slide. Before irradiation, the culture medium was replaced by an aliquot (1 mL) of poration medium with suspended GNRs and PI. Samples were porated through an air objective (×10, NA 0.3, WD 10mm, UPLFLN; Olympus) with a Ti : sapphire laser (operating at 800 nm, 80 MHz repetition rate, 140 fs pulse width; Chameleon Ultra II, Coherent) on a microscope (Ultima; Prairie Technologies). The excitation field was facilitated by an x-y laser scanner (U-1002; Prairie Technologies). A typical set-up utilized a frame size of 1 mm^2, frame rate of 800 ms, and total exposure time of 1 min. After irradiation, the cells were incubated at 37 °C in a 5% CO_2 incubator for ~1 hour. Extracellular molecules not taken up were removed by washing with warm culture medium. For delivery of blue dye (SYTOX Blue), the samples were treated again, according to the same protocol. Large-scale delivery was performed by patterning the exposure areas with an automated specimen stage with a scanning system (Prairie Technologies). Cell viability tests were performed by adding calcein AM (Invitrogen) to the culture medium to a final concentration of 2 μM after poration and incubating for ~1 hour for cell recovery. Cells were incubated with calcein AM at 37 °C in a 5% CO_2 incubator for 30 min and washed three times with culture medium.

siRNA delivery for gene regulation in MES cells. Two single-stranded RNA molecules (egfp 21-nt sense: gacguaaacggccacaaguuc and corresponding anti-sense; Bioneer) were dissolved in nuclease-free water to 100 μM, respectively.[26] After mixing and annealing at 90 °C for 2 min and subsequently at 37 °C for 1 hour, a stock solution of annealed double-stranded siRNA molecules was made by slowly cooling to room temperature and diluting with nuclease-free water to a concentration of 10 μM. Before experimentation, an aliquot (4 μL) was diluted with 0.5 mL of poration medium with GNRs (4 μg/mL) suspended to a final concentration of ~80 nM.

The TNG MES cells, containing a GFP reporter inserted into the Nanog locus, were a kind gift from the laboratory of Ian Chambers.[27] The TNG cells were cultured on microplates (multidishes; Nunc) precoated with 0.1% gelatin solution (Sigma). The TNG culture medium was DMEM/F12, GlutaMax (with sodium bicarbonate and sodium pyruvate; Gibco) supplemented with 10% FBS (Gibco), 1% penicillin streptomycin (Invitrogen), 1% nonessential amino acids (Invitrogen), 55 μM 2-mercaptoethanol (Gibco), 100 units/ml LIF (Millipore).[27] After cell confluency reached ~40%, the culture medium was changed with 0.5 mL of Opti-MEM I (reduced serum medium; Gibco) and incubated at 37 °C with 5% CO_2 for 1 hour. The culture medium was replaced with poration medium containing suspended GNRs and siRNA molecules. Samples were mounted on the microscope (Ultima; Prairie Technologies) and laser-irradiated at a pulse fluence of 2 mJ/cm^2, following the same protocols as described in the dye delivery section. After incubation for 1 hour,

cells were washed with culture medium and cultured in an incubator for 1 day. Finally, after the nuclei were stained by Hoechst 34580 according to the manufacturer's instructions (Invitrogen), samples were examined by wide-field epifluorescence microscopy (Axio Observer; Carl Zeiss) for inspection of GFP expression.

Lipofection of TNG stem cells with siRNA. For transfection of TNG stem cells with siRNA, the Lipofectamine 2000 reagent (Invitrogen) was utilized, according to the manufacturer's protocol. Briefly, 4 μL of stock siRNA (100 μM in nuclease-free water; Bioneer) and 1.5 μL of Lipofectamine 2000 were individually added to two samples of 100 μL of Opti-MEM I reduced serum medium (Gibco). After incubation for 5 min at room temperature, the two samples were combined and gently mixed for 20 min. The complex was diluted by adding 300 μL of Opti-MEM I reduced serum medium to a final siRNA concentration of ~80 nM. The siRNA-Lipofectamine 2000 complex solution was incubated for 4 hours with TNG cells, which had been precultured for ~1 hour in Opti-MEM I reduced serum medium. After lipofection, cells were cultured in TNG culture medium for 1 day, nuclei were stained by Hoechst 34580, and samples were inspected by epifluorescence microscopy.

Fluorescence microscopy. The wide-field epifluorescence microscope was equipped with an illumination system (120Q; X-Cite) and various excitation filters (G365, BP470/40, and BP 546/12; Carl Zeiss). Emission was collected by a ×10 objective (NA 0.25, A-plan, ph 1; Carl Zeiss) with various band-pass filters (BP 445/50, BP 525/50, and BP 575-640; Carl Zeiss) and recorded with a charge-coupled device (Axiocam Mrm; Carl Zeiss). All fluorescence images were recorded by the wide-field epifluorescence microscope, except that time-dependent PI uptake was monitored by a swept-field confocal microscope (Prairie Technologies). The sample was excited through an air objective (×10, NA 0.3, WD 10 mm, UPLFLN; Olympus) with a solid-state diode laser (green line, Aurora; Prairie Technologies). Epifluorescence passing through a 565-nm long-pass filter (E565lp; Chroma Tech) was collected and detected by an electron-multiplying CCD (QuantEM:512SC; Photometrics). The exposure time was 0.1 seconds with a 10-second repetition rate and was performed over 30 min.

Histograms of the single-cell fluorescence intensity. Histograms of the average fluorescence intensity of single TNG stem cells were examined by ImageJ. Briefly, regions of interest (ROIs) of single cells were defined by the locations and areas of nuclei (in blue fluorescence images). Green fluorescence intensities in corresponding ROIs were averaged to obtain the average GFP expression in single cells. The data were collected and plotted as histograms.

Observation of single pores on cell membranes by SEM. The MEFs were fixed with 4% paraformaldehyde (Sigma) for 15 min. Excess paraformaldehyde was washed away with cold PBS (~4 °C) three times. Cells were placed in poration medium with suspended GNRs (4 μg/mL) and were laser-irradiated at a pulse fluence of 2 mJ/cm^2. Samples were washed and incubated with 50% ethanol in PBS buffer for 15 min. The ethanol percentage was gradually increased from 50% to 100%, and samples were stored at 4 ^{o}C for 1 day. After the ethanol was aspirated, the samples were air-dried, deposited with ~2-nm-thick gold using sputtering (SEM coating system; Polaron), and inspected by SEM (S-5000; Hitachi).

Simulation of local field enhancement and photothermal conversion of GNRs. To investigate the local EM field enhancement and temperature profile around GNRs, a three-dimensional model was developed in the FE-based software package (COMSOL Multiphysics). To match the experimental conditions, a 10 x 39 nm GNR was placed in the middle of a cube of water (each side: 400 nm; > 10-times larger than the GNR), and an EM field was irradiated (800 nm wavelength, 140 fs pulse width, and 2 mJ/cm^2 single pulse optical energy). Because the GNR size is ~20-fold smaller than the wavelength of light, the incident EM wave could be simplified by a plane wave. Radio frequency (RF) and heat modules were combined to simulate plasmonic interactions between light, antennas, and photothermal effects. First, local EM field enhancement by the GNR was solved by scattered field in the RF module. Second, photothermal conversions in GNRs via electron-phonon and phonon-phonon coupling, along with subsequent heat dissipation to the environment, were simulated by heat modules. The output showed a thermal image of a GNR at 10 ps after irradiation.

References

1. Takahashi, K. & Yamanaka, S. Induction of pluripotent stem cells from mouse embryonic and adult fibroblast cultures by defined factors. *Cell* **126**, 663-676 (2006).

2. Warren, L., *et al.* Highly efficient reprogramming to pluripotency and directed differentiation of human cells with synthetic modified mRNA. *Cell Stem Cell* **7**, 618-630 (2010).

3. Robinton, D.A. & Daley, G.Q. The promise of induced pluripotent stem cells in research and therapy. *Nature* **481**, 295-305 (2012).

4. Link, S. & El-Sayed, M.A. Spectroscopic determination of the melting energy of a gold nanorod. *J Chem Phys* **114**, 2362-2368 (2001).

5. Huang, X.H., Neretina, S. & El-Sayed, M.A. Gold Nanorods: From Synthesis and Properties to Biological and Biomedical Applications. *Advanced Materials* **21**, 4880-4910 (2009).

6. Urban, A.S., Pfeiffer, T., Fedoruk, M., Lutich, A.A. & Feldmann, J. Single-step injection of gold nanoparticles through phospholipid membranes. *ACS Nano* **5**, 3585-3590 (2011).

7. Urban, A.S., *et al.* Controlled nanometric phase transitions of phospholipid membranes by plasmonic heating of single gold nanoparticles. *Nano Lett* **9**, 2903-2908 (2009).

8. Kyrsting, A., Bendix, P.M., Stamou, D.G. & Oddershede, L.B. Heat profiling of three-dimensionally optically trapped gold nanoparticles using vesicle cargo release. *Nano Lett* **11**, 888-892 (2011).

9. Medarova, Z., Pham, W., Farrar, C., Petkova, V. & Moore, A. In vivo imaging of siRNA delivery and silencing in tumors. *Nat Med* **13**, 372-377 (2007).

10. Paganin-Gioanni, A., *et al.* Direct visualization at the single-cell level of siRNA electrotransfer into cancer cells. *Proc Natl Acad Sci U S A* **108**, 10443-10447 (2011).

11. Yan, R., *et al.* Nanowire-based single-cell endoscopy. *Nat Nanotechnol* **7**, 191-196 (2012).

12. Chakravarty, P., Qian, W., El-Sayed, M.A. & Prausnitz, M.R. Delivery of molecules into cells using carbon nanoparticles activated by femtosecond laser pulses. *Nat Nanotechnol* **5**, 607-611 (2010).

13. Cai, D., *et al.* Highly efficient molecular delivery into mammalian cells using carbon nanotube spearing. *Nat Methods* **2**, 449-454 (2005).

14. Boukany, P.E., *et al.* Nanochannel electroporation delivers precise amounts of biomolecules into living cells. *Nat Nanotechnol* **6**, 747-754 (2011).

15. French, C.T., *et al.* Dissection of the Burkholderia intracellular life cycle using a photothermal nanoblade. *Proc Natl Acad Sci U S A* **108**, 12095-12100 (2011).

16. Wu, T.H., Kalim, S., Callahan, C., Teitell, M.A. & Chiou, P.Y. Image patterned molecular delivery into live cells using gold particle coated substrates. *Opt Express* **18**, 938-946 (2010).

17. Lukianova-Hleb, E.Y., *et al.* Selective gene transfection of individual cells in vitro with plasmonic nanobubbles. *J Control Release* **152**, 286-293 (2011).

18. Tirlapur, U.K. & Konig, K. Targeted transfection by femtosecond laser. *Nature* **418**, 290-291 (2002).

19. Yavuz, M.S., *et al.* Gold nanocages covered by smart polymers for controlled release with near-infrared light. *Nat Mater* **8**, 935-939 (2009).

20. Lee, S.E., Liu, G.L., Kim, F. & Lee, L.P. Remote optical switch for localized and selective control of gene interference. *Nano Lett* **9**, 562-570 (2009).

21. Lee, S.E., *et al.* Biologically functional cationic phospholipid-gold nanoplasmonic carriers of RNA. *J Am Chem Soc* **131**, 14066-14074 (2009).

22. Braun, G.B., *et al.* Laser-Activated Gene Silencing via Gold Nanoshell-siRNA Conjugates. *ACS Nano* **3**, 2007-2015 (2009).

23. Wu, G., *et al.* Remotely triggered liposome release by near-infrared light absorption via hollow gold nanoshells. *J Am Chem Soc* **130**, 8175-8177 (2008).

24. Yang, K. & Ma, Y.Q. Computer simulation of the translocation of nanoparticles with different shapes across a lipid bilayer. *Nat Nanotechnol* **5**, 579-583 (2010).

25. Shi, X., von dem Bussche, A., Hurt, R.H., Kane, A.B. & Gao, H. Cell entry of one-dimensional nanomaterials occurs by tip recognition and rotation. *Nat Nanotechnol* **6**, 714-719 (2011).

26. Caplen, N.J., Parrish, S., Imani, F., Fire, A. & Morgan, R.A. Specific inhibition of gene expression by small double-stranded RNAs in invertebrate and vertebrate systems. *Proc Natl Acad Sci U S A* **98**, 9742-9747 (2001).

27. Chambers, I., *et al.* Nanog safeguards pluripotency and mediates germline development. *Nature* **450**, 1230-1234 (2007).

28. Huebsch, N. & Mooney, D.J. Inspiration and application in the evolution of biomaterials. *Nature* **462**, 426-432 (2009).

29. Tong, L., *et al.* Gold Nanorods Mediate Tumor Cell Death by Compromising Membrane Integrity. *Adv Mater* **19**, 3136-3141 (2007).

30. Qian, X., *et al*. In vivo tumor targeting and spectroscopic detection with surface-enhanced Raman nanoparticle tags. *Nat Biotechnol* **26**, 83-90 (2008).

CHAPTER 3

Graphene Nanopores with Integrated Optical Antennae for Nucleic Acid Analysis

The atomically thin graphene[1-3] is an ideal membrane for nanopores-based single-molecular nucleic acid analysis.[4-7] The conventional approach to creating nanopores on graphene requires a sophisticated electron beam sculpting/drilling process.[4-9] Here, utilizing the localized heating of hot-spots with gold nanorods, we report that graphene nanopores can be fabricated and integrated with an optical antennae with a single irradiation step. Heating a nanometre-scale spot by photothermal effect of a gold nanorod resting on a graphene membrane forms a nanoscale pore with an integrated gold nanoantenna.[10-13] The unique graphene nanopore-plasmonic nanoantenna interface is composed of a nanopore with dimensions as small as a few nanometers and a hemispherically shaped gold nanoparticle located adjacent to it. The unique plasmonic traits of plasmonic nanoparticles allow them to focus micron-scale light into many nanoscale spots, thus enabling parallel nanopore fabrication via a simple and robust way. By controlling the laser fluence and the dimensions of the nanoparticles, the nanopore shape and the size of the integrated nanoantennae are tunable. The integrated plasmonic nanoantenna achieves the desired optical function, demonstrating multifold enhancement of the fluorescent signal during the translocation of a single DNA molecule through a graphene nanopore. We believe that our approach represents a significant advance and a new direction in nanopore-based DNA and RNA analysis and sequencing [8,9,14-16].

3.1 Introduction

Figure 3.1a shows an illustration of the graphene nanopore with a plasmonic nanoantenna as a single-molecular nucleic acid analysis platform. Similarly to conventional solid-state nanopores[8,15], the translocation of biomolecules occurs through a nanoscale pore on an atomically thin graphene material. The hot-spot on integrated plasmonic optical antenna can be used as a plasmonic enhancer to integrate current standard ion current and optical measurements. This complementary detection scheme could potentially improve signal selectivity while preserving the excellent spatial resolution offered by the graphene nanopores. Optically enhanced detection with specific fluorescent probes attached to each nucleotide[16] may improve the accuracy of base identification. The optical features of an integrated plasmonic optical antenna could enable new functions such as plasmonic enhanced fluorescence imaging, surface-enhanced Raman spectroscopy and plasmonic trapping of biomolecules. In addition to plasmonic enhancement, the metallic surfaces of the nanoantennae could facilitate functionalisation with biomolecules[17,18], thus enabling specific biomolecular interactions (e.g. enzymatic-mediated unzipping of double stranded DNA for sequencing).[19,20]

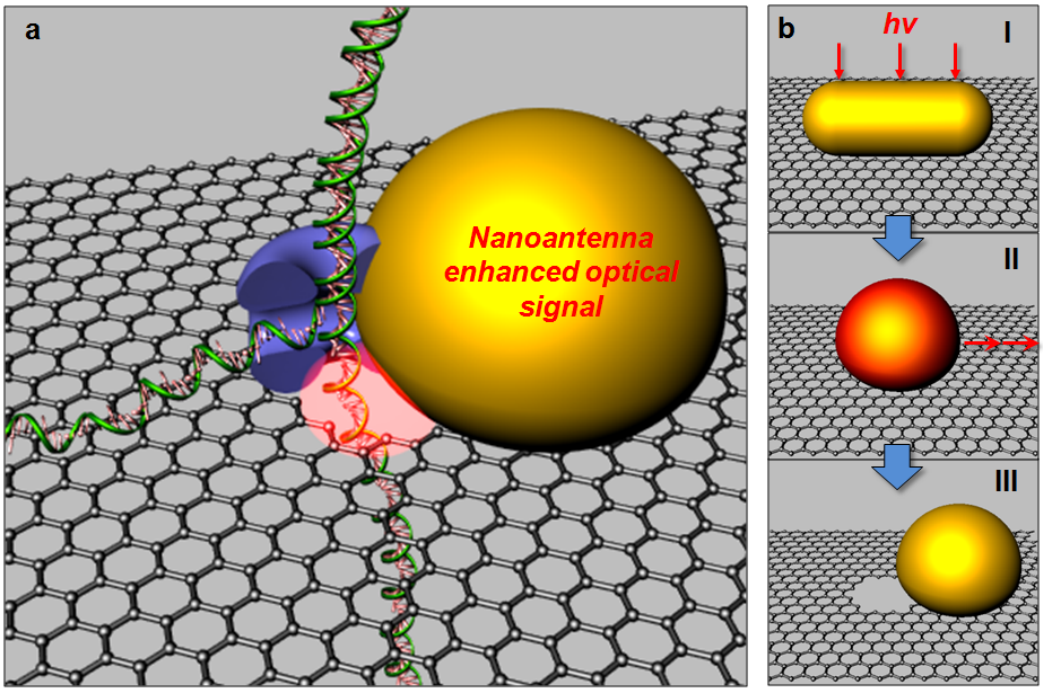

Figure 3.1. Graphene nanopores with integrated optical antennae for nucleic acid analysis. **a,** Illustration of a DNA analysis platform made by a graphene nanopore integrated with a gold nanoparticle as a plasmonic enhancer and a chemical reactor. **b,** Illustration of one-step fabrication process used to form graphene nanopores with integrated optical antennae using photothermal sculpting. First, a gold nanorod on a graphene membrane is exposed to laser light (*hv*). Second, the nanorod melts and becomes mobile. Finally, the hot nanoparticle oxidises the graphene membrane and creates a nanopore, and then cools down to form a hemispherical gold nanoparticle.

Figure 3.1b shows an illustration of our one-step fabrication process used to form graphene nanopores with integrated optical antennae. Graphene is synthesised[21,22] and transferred[23] onto a carbon grid or an ~10nm-thick carbon membrane, and a drop of gold nanorods solution is then dried on graphene. The gold nanorods on graphene are exposed with light with the wavelength matching the the resonant peak of the gold nanorods (I in Figure 3.1b). For example, the maximum absorption for gold nanorods with short and long dimensions of 10 nm and 38 nm, respectively, occurs at a wavelength of approximately 800 nm. During illumination with a femto-second (fs) laser, a photothermal effect causes gold nanorods to melt and results in the formation of a heated spot at the nanoparticle (II in Fig. 3.1b). According to simulation results, the nanoparticle in this condition reaches a maximum temperature of 680°C and then cools down to room temperature under irradiation of laser pulse fluence of 2 mJ/cm^2 (Fig. 3.2). These hot nanoparticles, with temperature above the oxidation temperature of the graphene membrane, remove the grapheme membrane with controllable dimensions (III in Fig. 3.1b). [24] Both round

and rod shape of nanopores can be made, depending on the mobility of melted gold nanoparticles (see below).

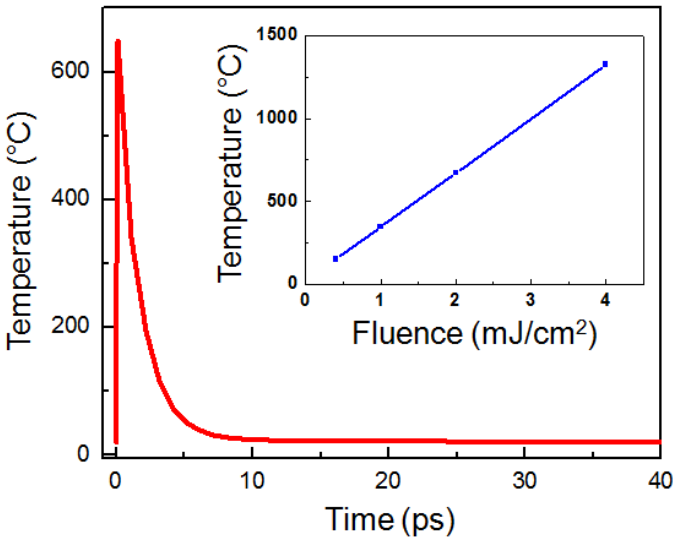

Figure 3.2. Simulation of the temperature of a gold nanorod. The time-dependent temporal profile of a gold nanorod after a fs pulse laser irradiation at 2 mJ/cm^2 fluence. The substrate is a single layer of graphene on a carbon membrane. (Inset) A plot of peak temperature of GNRs versus single pulse fluence of the incident laser.

3.2 Fabrication of Graphene Nanopores with Integrated Optical Antennae

Figures 3.3a and 3.4a show scanning electron microscope (SEM) images of multiple nanopores created simultaneously on graphene (with an ultra-thin carbon membrane) by our photothermal sculpting method. Note that pores and gold particles appear black and white in SEM images, respectively. At the wavelength of 800nm (matched with absorption of the gold nanorods), the minima laser pulse fluence to create nanopores is approximately 1.5 mJ/cm^2 . Over this energy, GNRs undergo re-shaping to a hemispherical (Figure 3.3b). Without irradiation, GNRs did not change their conformation or create nanopores on membranes (Figure 3.4b). At laser fluence at 0.5 mJ/cm^2, the shape change from nanorods to hemispheres can be observed but no sign of poration. Furthermore, without supporting carbon membranes, photothermal-mediated poration is also observed in free-standing graphene membranes (Figure 3.4c). However, in this case, the graphene membrane is less stable than that with a supporting carbon membrane under laser illumination[25].

Transmission electron microscopic (TEM) images with analysis provide more details in

graphene nanopores with integrated optical nanoantennae, as shown in Figures 3.3c-3.3e. Note that in TEM images pores and gold nanoparticles appear white and black, respectively. Those TEM images demonstrated that gold nanoparticles are located at the nanopores with approximately 10-nm in size by photothermal sculpting. By fine-tuning of the laser illumination conditions, it is possible to create 2 nm wide nanopores (Figure 3.4d). SEM energy dispersive analysis (Fig. 3.5), together with electron diffraction (Fig. 3.3d), is performed to confirm and evaluate the crystallinity of gold nanoparticles after photothermal-induced melting. Furthermore, atomic resolution TEM is equipped to study the edge nanostructure of a graphene nanopore[26]. Figure 3.3e shows that the edge with graphene hexagonal lattice has nanometre-scale roughness after sculpting.

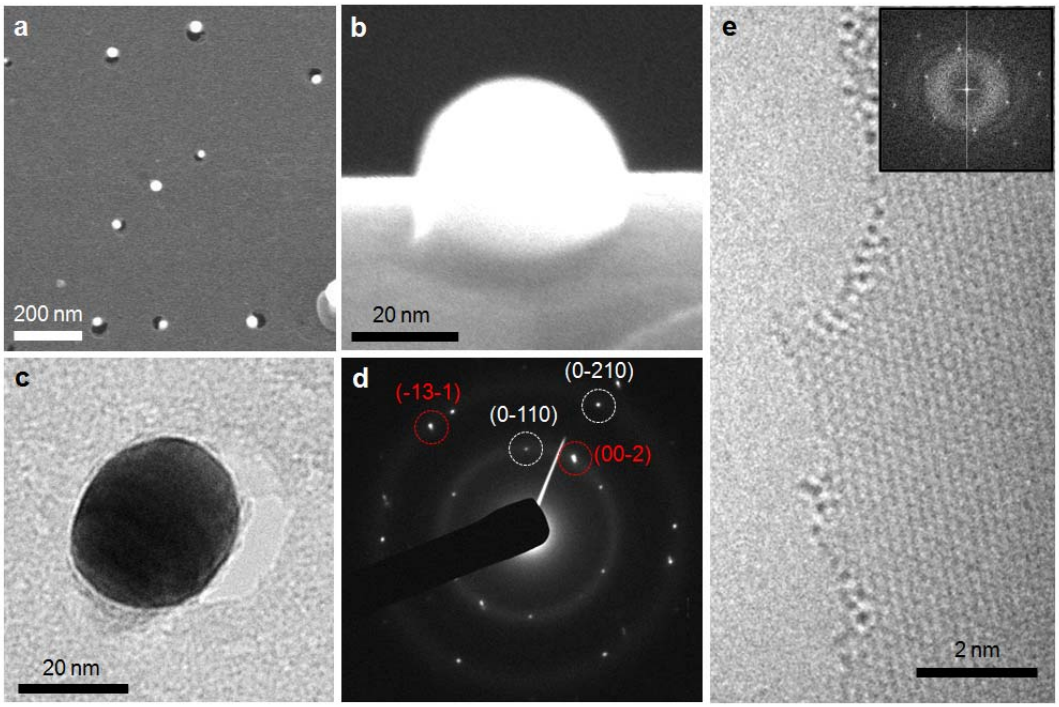

Figure 3.3. Geometric characterization of graphene nanopores and integrated antennae. **a,** SEM image of graphene nanopores (black) with an integrated optical antennae (white) on an ultra-thin carbon membrane. **b,** Side-view SEM of a hemispherically shaped gold nanoparticle, original from a melted gold nanorod. **c,** TEM image of a graphene nanopore (white) with a nanoantenna (black). **d,** Electron diffraction pattern of a gold nanoantenna on a graphene membrane. Electron diffraction pattern of a gold nanoparticle indexed as the [310] zone axis of face-centred cubic (red-dot circles) and hexagonal patterns from single-layer graphene (white-dot circles). **e,** A TEM image of the edge of a graphene nanopore with Fourier transform of the image (inset).

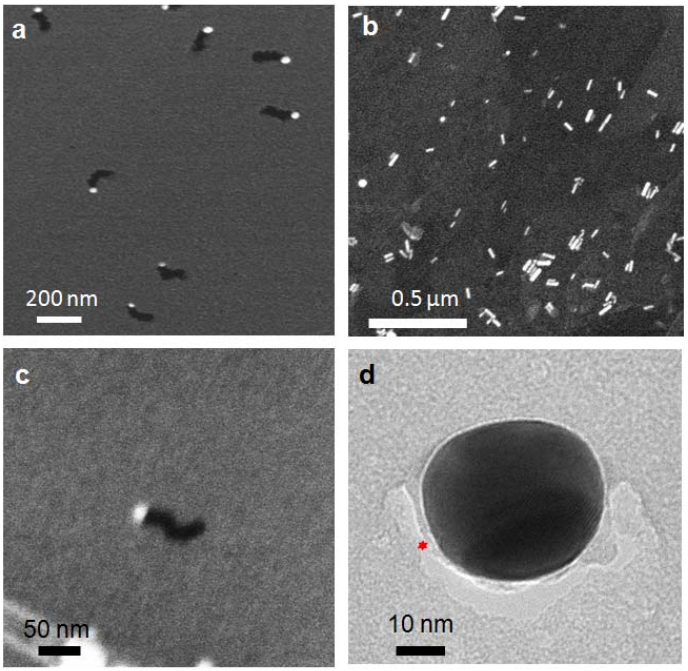

Figure 3.4. **a,** Nano-scaled hot-spots convert light energy from micron-sized light to achieve high-throughput nanopore fabrication. **b**, No sign of poration in a graphene membrane in absence of illumination. **c**, SEM image of a nanopore (black) with an integrated gold nanoantenna (white) created on a graphene membrane without a supporting substrate. **d**, The TEM image of the smallest graphene nanopore (width ~ 2 nm) created by our method.

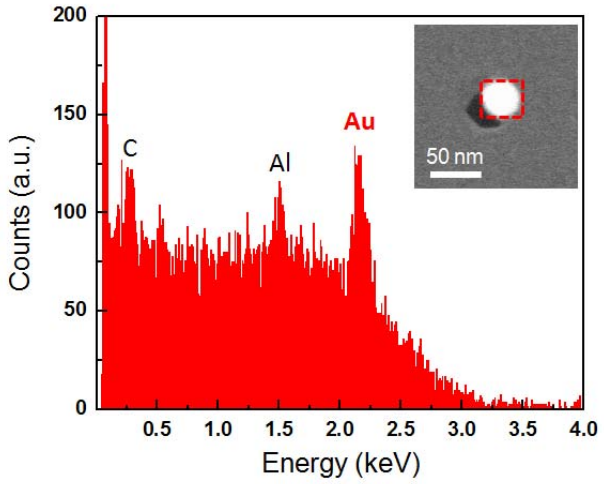

Figure 3.5. SEM energy dispersive analysis (EDS) of an integrated antenna. It indicated that the optical antenna is mainly composed of gold.

3.3 Tunability of Graphene Nanopores and Integrated Plasmonic Antennae

We scanned laser illumination fluence from 0 to 8 mJ/cm^2 to test the tunability of light-to-heat nanopore sculpting on the dimensions of the nanopores (Figs. 3.6a and 3.6b). The standard sample is made by graphene on a supporting carbon membrane and GNR (size: 10 nm by 38 nm). At the laser fluence lower than 1.5 mJ/cm^2, reshaping of the gold nanorods occurred but without nanopore formation. At higher laser power ($\geq$1.5 mJ/cm^2), we successfully created nanopores with integrated gold nanoparticles. Note that the aspect ratio (b/a) of the nanopores is dependent on the illumination fluence. Figure 3.6b shows a plot of laser power-dependent aspect ratio of pores (higher power results in larger aspect ratio). For example, when the laser fluence is approximately 4 mJ/cm^2, nanopores with high aspect ratio (~5.5) are fabricated. Based on this result, we suggest the mechanism about pore formation in which the hot gold nanoparticles are very mobile after photothermal-induced melting (Fig. 3.1b). In addition, at very high power (laser fluence between 5 - 8 mJ/cm^2), anisotropic nanopores can be created, but gold nanoparticles begin to disappear. These observations support that at high level of laser fluence, nanoparticles begin to detach from the surface of graphene because the optical pressure becomes higher than the surface tension/interaction.[27,28].

In addition to shape controllability, nanopore diameters can be tuned as well by changing the size of the deposited nanoparticles (Fig. 3.6c). We varied the initial nanoparticle dimensions and shapes (i.e. rod or sphere) and kept the irradiation fluence at 2 mJ/cm^2. Three different types of gold nanoparticles were used: gold nanorods with short by long axis lengths of 10 nm by 38 nm and 25 nm by 73 nm, and gold nanospheres with a 150 nm diameter. We tuned our laser wavelength to match absorption peaks of each type of nanoplasmonic particles (details in methods). The results show that each type of nanoparticle creates a nanopore with a diameter proportional to the initial dimensions of the nanoparticles after irradiation (Fig. 3.6c). Their photophysical properties were further characterized by darkfield imaging (Fig. 3.6d) of integrated plasmonic nanoantennae with three different dimensions. The darkfield images show dark green, bright green and orange colours (left to right, insets in Fig. 3.6d) taken from graphene nanopores with plasmonic nanoparticles of differing diameters. The results are consistent with previous reports in the literature[29] where a redshift of plasmon resonance occurs as the size of the nanoparticles increases. Spectrum analysis shows scattering peaks of 510 nm, 550 nm and 590 nm from three different directions with respect to the nanoparticle. We believe that the tunability of the optical characteristics could allow for multiplexed optical detection/sequencing in the future.

3.4 DNA Translocation through Integrated Graphene Nanopores with Plasmonic Optical Antennae.

We explored the optical features of these graphene nanopores with integrated optical antennae during DNA translocation events[30]. Lambda (λ) DNA (48.50 kbp) molecules were labelled with green fluorescence dyes (TOTO-1). The DNA sample and buffer solution were injected into the bottom chamber and the top reservoir, respectively, of a polydimethylsiloxane

(PDMS) electrophoresis device mounted with an array of graphene nanopores and integrated optical antennae (Figs. 3.7 and 3.8a). The dynamics of DNA translocation through the graphene nanopores were recorded by a water immersion objective lens on a fluorescent microscope. Gold nanoantennae on the edges of the nanopores have a surface plasmon resonance peak at 510 nm, which overlaps well with the absorption peak of the fluorophores, ensuring resonant interactions and metal-enhanced fluorescence (inset of Fig. 3.8a)[31].

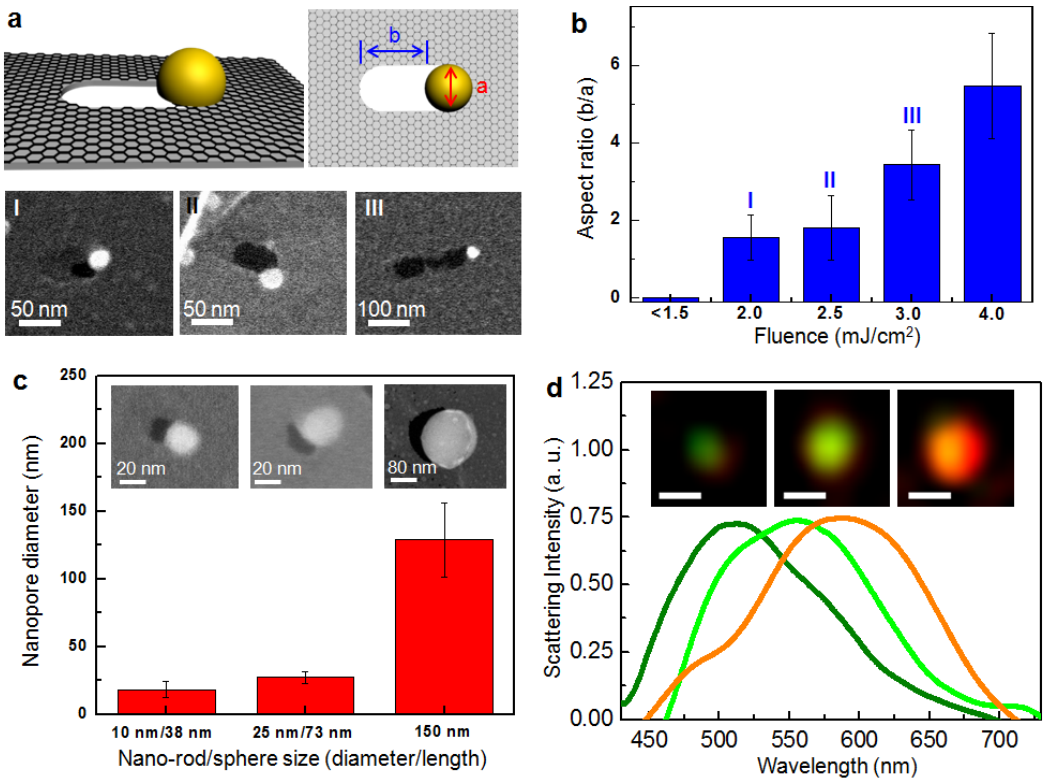

Figure 3.6. Shape and size tunability of photothermal-mediated poration and corresponding surface plasmon resonance characteristics. **a,** Schematic illustration of nanopore anisotropy, defined by *b/a*. SEM images of nanopores created at different laser illumination fluence. **b,** Statistical analysis of nanopore anisotropy as a function of laser fluence. The error bars represent one standard deviation. **c,** Statistical distribution of the diameters of nanopores formed with three different sizes of gold nanoparticles: gold nanorods with short by long axis lengths of 10 nm by 38 nm and 25 nm by 73 nm, and gold nanospheres with a 150 nm diameter. The inset shows representative SEM images of nanopores. **d,** Darkfield scattering images and corresponding spectra of plasmonic nanoparticles taken from nanopores with integrated nanoantennae that are shown in Figure 3.6c. Scale bar, 0.5 μm.

When DNA molecules passed through the nanopore under an electrical field, we observed a bright fluorescent spot at the nanopore. The bright spot maintains its intensity during the entire elongation and stretching process (Fig. 3.8b), and finally, the λ DNA is nearly fully stretched to approximately 18 μm with minimal partial coiling. Detailed analysis of the fluorescent intensity profile of fully stretched DNA (Fig. 3.8c) shows that the fluorescence intensity is 4- to 5-fold higher at the nanopore (red arrow) than at the centre (blue arrow), as shown in Figures 3.8b and 3.8c. This enhanced fluorescence was observed reproducibly in subsequent studies, as seen in the histogram of enhancement factors in Figure 3.8d with a peak centred at 4.5-fold. In contrast to the results of the nanopores without any plasmonic nanoantennae (Fig. 3.9), these observations clearly demonstrate that the plasmonic nanoantennae enhance single-molecule fluorescence[31].

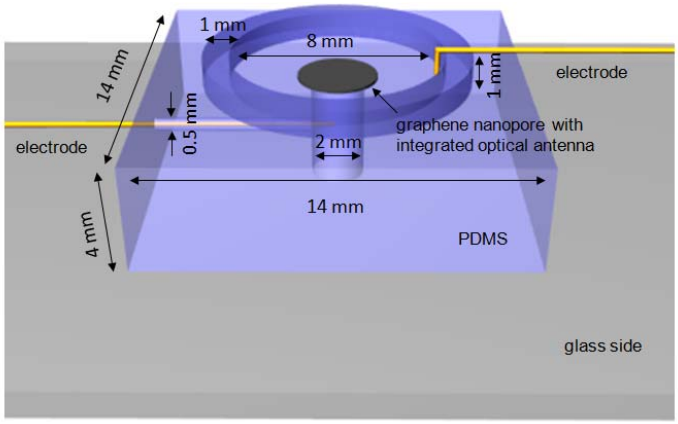

Figure 3.7 Schematic illustration of the graphene nanopore DNA translocation chip. The gold lines represent electrodes and the blue parts represent PDMS.

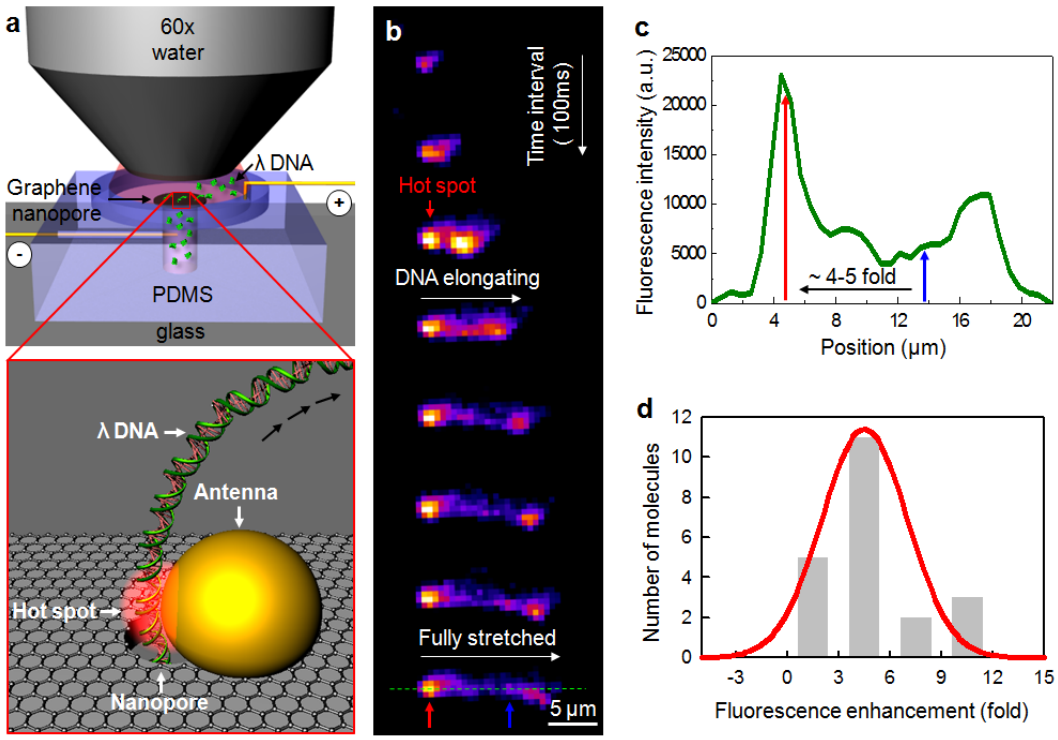

Figure 3.8. DNA translocation through integrated graphene nanopores with plasmonic optical antennae. **a,** Schematic drawing of a PDMS device mounted with an array of graphene nanopores that have integrated nanoantennae. The inset shows a zoomed-in view of the plasmonic enhancement of the fluorescence of dyes in a single λ DNA molecule when passing through a graphene nanopore with a plasmonic nanoantenna. **b,** Time series confocal scanning fluorescence images of λ DNA translocation with a time interval of 100 ms. The last image shows DNA that has been fully stretched by the applied electrical field at 800 ms. **c,** Fluorescent intensity profile along the green dashed line in Figure 3.8b. **d,** Histogram of plasmonic fluorescent enhancement factors.

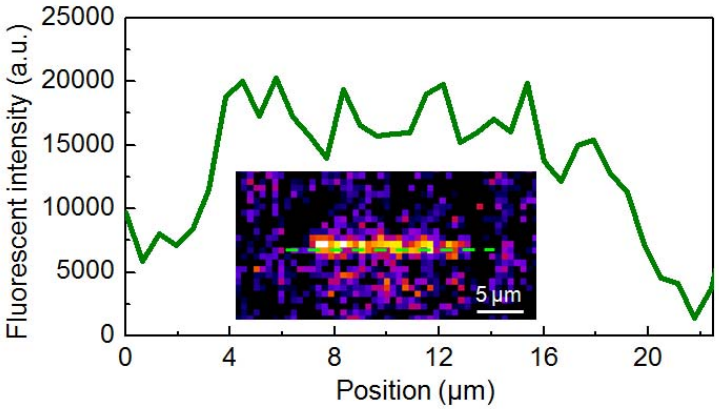

Figure 3.9. Uniform fluorescence intensity of the DNA that has been fully stretched by the applied electrical field during translocation through a nanopore without a plasmonic optical antenna. The inset shows a confocal scanning fluorescence image of λ DNA translocation through a nanopore without a plasmonic optical antenna. The translocation membrane used in this control experiment (polycarbonate, diameter of pores: 200nm) contributed to the auto-fluorescent background.

3.5 Conclusions and Outlook

This light-to-heat nanopore sculpting presents numerous advantages over the conventional direct atomic displacement approach and provides new capabilities. First, light-to-heat sculpting allows for simple and inexpensive nanopore creation based on nanoplasmonic photothermal effects occurring well below the diffraction limit, thus eliminating the need for high-end electron microscopy. Second, light-to-heat poration intrinsically creates nanopores in parallel, whereas conventional electron beam sculpting forms nanopores sequentially[8]. Third, fewer potential defects can occur during photothermal sculpting spanning up to a few nanometers away from the plasmonic nanoparticle[11,17] compared to electron beam sculpting, as this new method does not expose the sample to electron beams at high acceleration voltages[4-9]. Finally, the readily integrated plasmonic nanoantennae serve new and unique functions, and we can envision the optical transducer[13] (e.g., plasmonic enhanced fluorescence imaging, surface enhanced Raman spectroscopy, and nanoplasmonic trapping of biomolecules) as a complement to conventional ion current measurements of biomolecule translocation.

We have developed a novel yet simple approach to creating nanopores on graphene through light-to-heat conversion of plasmonic nanoparticles, inducing nanometre-sized heated spots. We show that the unique graphene nanopore-optical antenna interface is formed with a graphene nanopore width as small as 2 nm and a hemispherically shaped gold nanoparticle spontaneously integrated at the nanopore. Furthermore, we successfully tune the nanopore shape and dimensions by controlling the laser illumination fluence and the size of the initial nanoparticles, respectively. This unique ability to adjust the nanopore shape could provide an interesting

biophysical platform for the study of translocation events dependent on the shapes (i.e., isotropic versus anisotropic) of biomolecules. The plasmonic resonance characteristics of the integrated nanoantennae can also be controlled for potential multiplexed optical detection as demonstrated by the fluorescent signal enhancement during λ DNA translocation through graphene nanopores. A significant enhancement of fluorescence intensity, together with atomically thin graphene membranes, makes integrated optical antennae/nanopores promising substrates for ultrasensitive and ultrafast detection for applications of DNA analysis.

Methods

Graphene synthesis. Graphene was synthesized by chemical vapor deposition (CVD) on a 25 μm thick copper foil[1] (99.8% Alfa Aesar, Ward Hill, MA). Briefly, copper foil was inserted into a quartz tube and heated to 1,000 °C while flowing 10 sccm H_2 at 150 mTorr. After annealing for 30 min, the gas mixture of 25 sccm CH_4 and 10 sccm H_2 at 520 mTorr was introduced for 20 min to synthesize graphene. Finally, the system was fast cooled to room temperature while flowing 20 sccm CH_4 at a pressure of under 330 mTorr.

Graphene transfer. After the synthesis, graphene was transferred to a Quantifoil holey carbon or an ultra-thin carbon membrane TEM grid (Electron Microscopy Sciences, PA) using a direct transfer method[2]. We placed the TEM grid onto a graphene-covered copper foil with the carbon film side facing the graphene. Then a small amount of isopropyl alcohol (IPA) was dropped on to the sample and air-dried. An additional flattening step (prior to the IPA step) of the copper foil or the TEM grid was performed by sandwiching it between glass slides to ensure better adhesion. Finally, the sample was placed into a solution of sodium persulfate to etch the underlying copper foil and was then rinsed with deionized water.

Photothermal poration of graphene. Suspended graphene or graphene on an ultra-thin carbon membrane was porated through an air objective (×10, NA 0.3, WD 10 mm, UPLFLN; Olympus) with a Ti:sapphire laser (80 MHz repetition rate, 140 fs pulse width; Chameleon Ultra II, Coherent) on a laser-scanning microscope (Ultima; Prairie Technologies). The diameter of the laser spot is ~4 μm. A typical setup utilized a frame size of 0.4 mm^2, and a laser spot dwell time of 10 μs.

High resolution transmission electron microscope (TEM) analysis of graphene nanopore. The high-resolution TEM image was obtained with the TEAM 0.5 operated at 80 kV at the National Center for Electron Microscopy[3]. The microscope is equipped with image Cs aberration corrector and monochromator.

Darkfield imaging and spectrum analysis. Our microscopy system is composed of a Carl Zeiss Axiovert 200 inverted microscope with a dry darkfield condenser, a true-color digital camera (CoolSNAP cf; Roper Scientific, NJ), and a 300 mm focal-length and 300 grooves/mm monochromator (Acton Research, MA) with a 1024 × 256-pixel cooled spectrograph CCD camera (Roper Scientific, NJ). The scattering images of gold nanoparticles were taken using a dry darkfield condenser with a 40X objective lens and a true-color camera with a white light illumination (100 W halogen lamp). To perform the scattering spectrum analysis of gold nanoparticles, the scattered light was routed to the monochromator and spectrograph CCD. An

aperture was placed at the entrance slit of the monochromator to obtain a spectrum solely from a single nanoparticle in the region of interest.

Lambda phage DNA translocation experiment. Lambda (λ) DNA (48.50 kbp; New England BioLabs) molecules were dissolved in 0.5X Tris/Borate/EDTA (TBE) buffer with 10 mM NaCl and then fluorescently labeled with TOTO-1 (Molecular Probes) at a molar ratio of 4 bp per dye molecule. The length of the λ DNA molecule is ~20 μm after labeling[4]. The sample was diluted with the same buffer with 1% BSA (1 mg/ml; Sigma) to a concentration of 20 ng/ml before being injected into a polydimethylsiloxane (PDMS; Sylgard) device. The device was constructed with four components: a standard microscope slide, a cured PDMS punched with two holes attached on top of the glass slide, an array of graphene nanopores with integrated gold optical antennae on the PDMS device sealed by epoxy adhesive, and a PDMS O-ring (inner diameter: 1 cm, height: 1 mm) attached on top of the PDMS device. The array of graphene nanopores with integrated gold optical antennae was fabricated with photothermal poration (laser fluence of 2.5 mJ/cm^2) of graphene/gold nanorods on an ultra-thin carbon membrane. The DNA sample and buffer with 1% BSA were injected to the bottom chamber and the top reservoir, respectively. We then connected the device with two Au electrodes (diameter: 0.1 mm; Sigma) to apply an electric field with a power supply (1–5 V; Keithley Instruments Inc.). The device was mounted on a swept-field confocal microscope (Prairie Technologies) and fluorescence was excited through a water objective (×60, NA 0.9, UPLFLN; Olympus) with a solid-state diode laser (488nm, Aurora; Prairie Technologies) from the top of the device. Epifluorescence passing through a 510-nm long-pass filter (Chroma Tech) was captured by an electron-multiplying CCD (QuantEM:512SC; Photometrics) with 2x2 pixel-binning and 100 ms exposure time.

References

1. Novoselov, K. S. *et al*. Two-dimensional gas of massless dirac fermions in graphene. *Nature* **438**, 197-200 (2005).

2. Zhang, Y., Tan, Y., Stormer, H. L. & Kim, P. Experimental observation of the quantum Hall effect and Berry's phase in graphene. *Nature* **438**, 201-204 (2005).

3. Novoselov, K. S. *et al*. Electric field effect in atomically thin carbon films. *Science* **306**, 666-669 (2004).

4. Garaj, S. *et al.* Graphene as a subnanometer trans-electrode membrane. *Nature* **467**, 190-193 (2010).

5. Schneider, G. F. *et al.* DNA translocation through graphene nanopores. *Nano Lett.* **10**, 3163-3167 (2010).

6. Merchant, C. A. *et al.* DNA translocation through graphene nanopores. *Nano Lett.* **10**, 2915-2921 (2010).

7. Venkatesan, B. M. *et al.* Stacked graphene-Al_2O_3 nanopore sensors for sensitive detection of DNA and DNA-protein complexes. *ACS Nano* **6**, 441-450 (2012).

8. Dekker, C. Solid-state nanopores. *Nature Nanotechnol.* **2**, 209-215 (2007).

9. Xie, P., Xiong, Q., Fang, Y., Qing, Q. & Lieber, C. M. Local electrical potential detection of DNA by nanowire-nanopore sensors. *Nature Nanotechnol.* **7**, 119-125 (2012).

10. Cao, L., Barsic, D. N., Guichard, A. R. & Brongersma, M. L. Plasmon-assisted local temperature control to pattern individual semiconductor nanowires and carbon nanotubes. *Nano Lett.* **7**, 3523-3527 (2007).

11. Fedoruk, M., Lutich, A. A. & Feldmann, J. Subdiffraction-limited milling by an optically driven single gold nanoparticle. *ACS Nano* **5**, 7377-7382 (2011).

12. Liu, G. L., Kim, J., Lu, Y. & Lee, L. P. Optofluidic control via photothermal nanoparticles. *Nature Mater.* **5**, 27-32 (2006).

13. Jain, P. K., Huang, X., El-sayed, I. H. & El-sayed, M. A. Noble metals on the nanoscale: optical and photothermal properties and some applications in imaging, sensing, biology, and medicine. *Acc. Chem. Res.* **41**, 1578-1586 (2008).

14. Pennisi, E. Search for pore-fection. *Science* **336**, 534-537 (2012).

15. Venkatesan, B. M. & Bashir, R. Nanopore sensors for nucleic acid analysis. *Nature Nanotechnol.* **6**, 615-624 (2011).

16. Branton, D. *et al.* The potential and challenges of nanopore sequencing. *Nature Biotechnol.* **26**, 1146–1153 (2008).

17. Lee, S. E., Liu, G. L., Kim, F. & Lee, L. P. Remote optical switch for localized and selective control of gene interface. *Nano Lett.* **9**, 562-570 (2009).

18. Park, S. Y. *et al.* DNA-programmable nanoparticle crystallization. *Nature* **451**, 553-556 (2008).

19. Manrao, E. A. *et al.* Reading DNA at single-nucleotide resolution with a mutant MspA nanopore and phi29 DNA polymerase. *Nature Biotechnol.* **30**, 349-353 (2012).

20. Geim, A. K. Graphene: status and prospects. *Science* **324**, 1530-1534 (2009).

21. Li, X. *et al.* Large-area synthesis of high-quality and uniform graphene films on copper foils. *Science* **324**, 1312-1314 (2009).

22. Bae, S. *et al.* Roll-to-roll production of 30 inch graphene films for transparent electrodes. *Nature Nanotechnol.* **5**, 574-578 (2010).

23. Regan, W. *et al.* A direct transfer of layer-area graphene. *Appl. Phys. Lett.* **96**, 113102-113102 (2010).

24. Liu, L. *et al.* Graphene oxidation: thickness-dependent etching and strong chemical doping. *Nano Lett.* **8**, 1965-1970 (2008).

25. Yoo, J.-H., In, J. B., Park, J. B., Jeon, H. & Grigorpoulos, C. P. Graphene folds by femtosecond laser ablation. *Appl. Phys. Lett.* **100**, 233124-233124 (2012).

26. Girit, C. O. *et al.* Graphene at the edge: stability and dynamics. *Science* **323**, 1705-1708 (2009).

27. Habenicht, A., Olapinski, M., Burmeister, F., Leiderer, P. & Boneberg, J. Jumping nanodroplets. *Science* **309**, 2043-2045 (2005).

28. Nedev, S., Urban, A. S., Lutich, A. A. & Feldmann, J. Optical force stamping lithography. *Nano Lett.* **11**, 5066-5070 (2011).

29. Ross, B. M. & Lee, L. P. Comparison of near- and far-field measures for plasmon resonance of metallic nanoparticles. *Optics Lett.* **34**, 896-898 (2009).

30. Chansin, G. A. T. *et al.* Single-molecule spectroscopy using nanoporous membranes. *Nano Lett.* **7**, 2901-2906 (2007).

31. Zhang, J., Fu, Y., Chowdhury, M. H. & Lakowicz, J. R. Metal-enhanced single-molecule fluorescence on silver particle monomer and dimer: coupling effect between metal particles. *Nano Lett.* **7**, 2101-2107 (2007).

CHAPTER 4

Plasmonic Nanoantennae-mediated Single miRNA Detection for Cancer Diagnosis

Short microRNAs (miRNAs,~22 nucleotides in length) are circulating in blood of cancer patients and can be specific biomarkers for cancer diagnosis.[1-7] Using blood-based circulating nucleic acids as biomarkers has gained considerable attention in recent years because it holds a number of advantageous features including low invasive sampling and easiness of probe designs. Here, we developed a simple, highly sensitive and robust method to detect circulating microRNAs (miRNAs) in the blood using DNA-conjugated gold nanoparticles (GNPs).[8-14] These metallic nanoparticles scatter the green light extremely strongly due to the surface plasmon resonance effect. The property lowers the detection threshold and improves the sensitivity to detect miRNA. Our results showed that the method could detect miRNAs in a dynamic range of 1 μM to 1pM. In addition to detecting miRNAs by single GNP, a dimer-form of GNP induced by target miRNAs is designed to induce the red shift in the scattering wavelength when binding to target miRNAs. This design made it possible to achieve single molecule detection by simply counting nanoplasmonic particles with scattering that is shifted towards the red wavelength. In addition to probe designs, we present an optical dark-field set-up based on total internal reflection illumination. This set-up shows highly potential to integrate with a microfluidic chip and becomes a portable point-of-care device.[15-17]

4.1 Introduction

In both normal and cancer cells, miRNAs are short non-coding RNAs that post-transcriptionally regulate gene expression.[1-4,6,7,18] In tumorigenesis, miRNAs function either as tumor suppressor or oncogene. In recent years, the miRNA profiling has gained a lot of attentions because it has a number of potential applications in screening cancers and monitoring the efficiency of anti-cancer treatments. In the blood, there are circulating nucleic acids and proteins released from dead cells before they get clear out of the body (Fig. 4.1a).[1,3,7,18] A simple and less invasive way to diagnose cancers is to detect cancer specific biomarkers that are circulating in the blood. miRNAs are potentially good biomarkers because they are relatively stable and it is easy to design probes against them. However, a big challenge is the considerably low concentration of circulating miRNAs in the blood or plasma, ranging from 100pM to 10fM. Several methods have been developed to detect such low copy number of miRNAs, including quantitative reverse transcription PCR and miRNA microarray.[3,5,11] However, these methods are fairly expensive and hard to implement outside the laboratories. Therefore, a novel detection method is necessary to provide point-of-care cancer diagnosis. The point-of-care portable-devices often require a single-step process in isothermal environments (e.g. room temperature). The PCR based approaches requires multi-step chemical reactions and thermal cycles of amplification as well as separate readout systems. A major advantage of single-molecule based detection method is that it

allows detecting trace amount of miRNAs directly without the need of amplification as well as that a simple readout system could be implemented. [16,18,19]

Laser-induced fluorescence technique is widely adopted for single-molecular observations in biological cell owing to its ultrahigh sensitivity and capabilities of direct imaging without any chemical amplification.[16-24] However, in applying this technique to point-of-care diagnosis, progress is often hampered by sophisticated optical designs and expensive detection equipments. It is because the detrimental photophysical properties of fluorescent probes, such as small absorption cross-section, photobleaching and blinking, inevitably restrict their applications for observations by simple and portable optical devices. Plasmonic nanoantennas such as gold nanoparticles, in contrast, are free of this limitation because of their huge absorption and scattering cross-sections.[8-10,12,13] Recently, there has been a resurgence of interest in leveraging Plasmonic nanoantennas for various biomedical sensing. Gold nanoparticles are finding increased utility as stable and visible materials important in biomedical diagnosis, including nucleic acid detections.[8-10,12,13]

In our study, we demonstrated that GNPs with a nominal size of ~ 40 nm are flexible and stable probes. The surface of GNP is easy to be functionalized and the size generates high enough scattering to detect single miRNA molecule without any amplification. In out study, we tested with a biomarker of early stage lung cancer, miRNA-1254.[2-5,25] Lung cancer is the leading cause of cancer mortality in humans. There is an urgent need to develop a simple and inexpensive platform to identify miRNA cancer markers in blood samples.

Here we demonstrated a novel concept of detecting miRNA-1254 at single molecule level with a probe conjugated to GNPs (Fig. 4.1b and 4.1c). We first performed an off-chip in bulk test of our detection concept. Our results clearly showed that the target miRNAs could be quantified at a wide range of concentration by dark-field imaging of single GNPs. Different from using fluorescence probes, our method is based on the Plasmon-enhanced light scattering of metallic nanoparticles. The GNP acts as superior antenna and generates much brighter scattering comparing to the fluorescence emission according to the calculation based on their photophysical property. Because of the substantially large cross-section and superb chemical stability of the GNPs, the scattering intensity generated by a single GNP is five-order of magnitude higher than the fluorescence intensity generated by a dye molecule.[10] The result illustrated that GNP-mediated detection provides high signal-to-noise ratio imaging without photobleaching and blinking issues, major concerns for using fluorescent probes.[10]

Second, for a point-of-care of miRNA detection design, we developed a portable total internal reflection plasmonic microscopy (TIRPM) system by coupling a LED white light source into PDMS/glass chips.[15-17,19] Similar to the total internal reflection fluorescence microscopy (TIRFM), TIRPM allows us to generate evanescent waves to illuminate plasmonic nanoparticles.[15-17,19] The localized excitation in substrate-sample surface shows the potential in improving the image quality as well as the sensitivity of detection. The capability of imaging at single-particle level was demonstrated where neither blinking nor photobleaching was detected. Our design innovatively combined the plasmonics and fluidics technologies for medical diagnosis and molecular detection. Furthermore, we integrated the microfluidics technology to reduce the

requirement of sample volume (few micro-litter) and lower the detection limit by the precise spatial-temporal control of the microenvironment of the device.

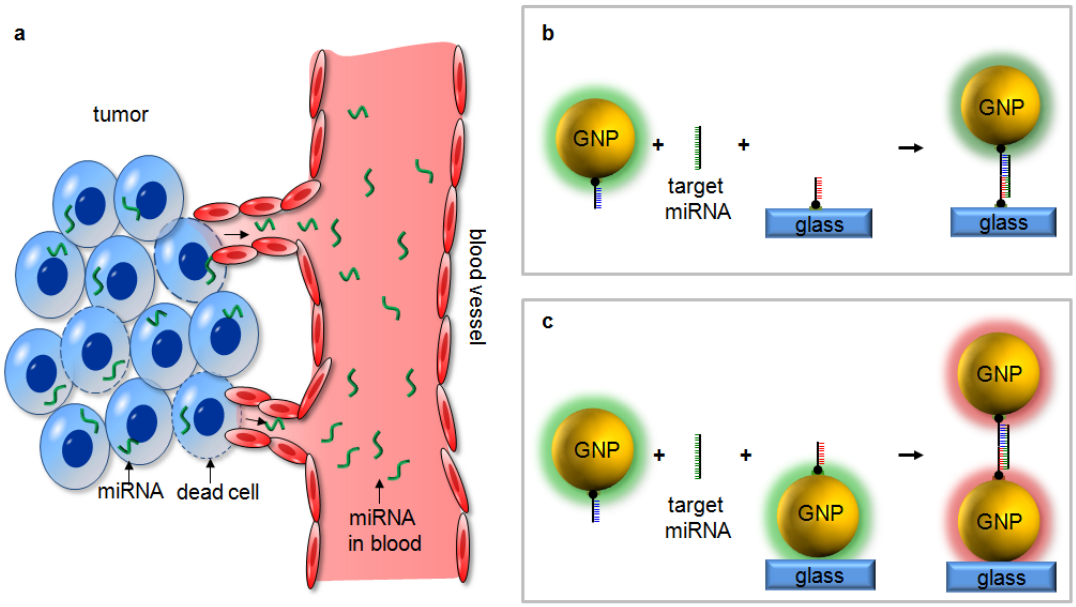

Figure 4.1, The schematic illustration of cancer diagnosis by detecting miRNA biomarkers in the blood. **a,** miRNA molecules (green) are released from dead tumor cells (blue cells with dash line contour) and circulate in the blood.[3,4,7] **b,** A schematic drawing of detecting single target miRNA (green) with a probe (blue) conjugated to GNPs and a probe immobilized on a glass slide. **c,** A schematic drawing of single target miRNA detection by GNP-GNP dimer formation. Note that the formation of dimers produces a remarkable red-shift in their far-field scattering.

4.2 Single GNPs-based miRNA Detection for Early Stage Lung Cancer Diagnosis

To diagnose early stage lung cancer, two DNA probes (blue and red, Fig. 4.2a) are designed and synthesized to hybridize with miRNA-1254 (a maker for early stage lung cancer). Briefly, one biotinylated DNA probe (blue) was labeled on a streptavidin conjugated GNP; the other biotinylated DNA probe (red) was immobilized on a glass slide coated with biotin-BSA and neutravidin. In the presence of target miRNA-1254 molecules (green), we observed the formation of GNP/miRNA complexes tethered to the glass slide. After washing away unbound GNPs, the specimen was imaged by a dark-field scattering microscopy (Fig. 4.2b). In the specimen that incubates with 1μM of the target miRNA-1254, we observed high density of single GNPs tethered on the glass slide. Most of the particles have strong green light scattering spots with the size of the diffraction limit, indicating that the signals come from individual GNP/miRNA complexes instead of aggregates (Fig. 4.2c and 4.2d). The density of the scattering spots was dependent on the concentration of miRNA-1254, as shown in the plot of the captured

GNPs density versus the miRNA concentration. The method could detect 1μM to 1 pM miRNAs (Fig. 4.3). At the concentration below 1pM, the non-specific binding of GNPs to the substrate surface becomes dominant as shown in the negative control without target miRNAs.

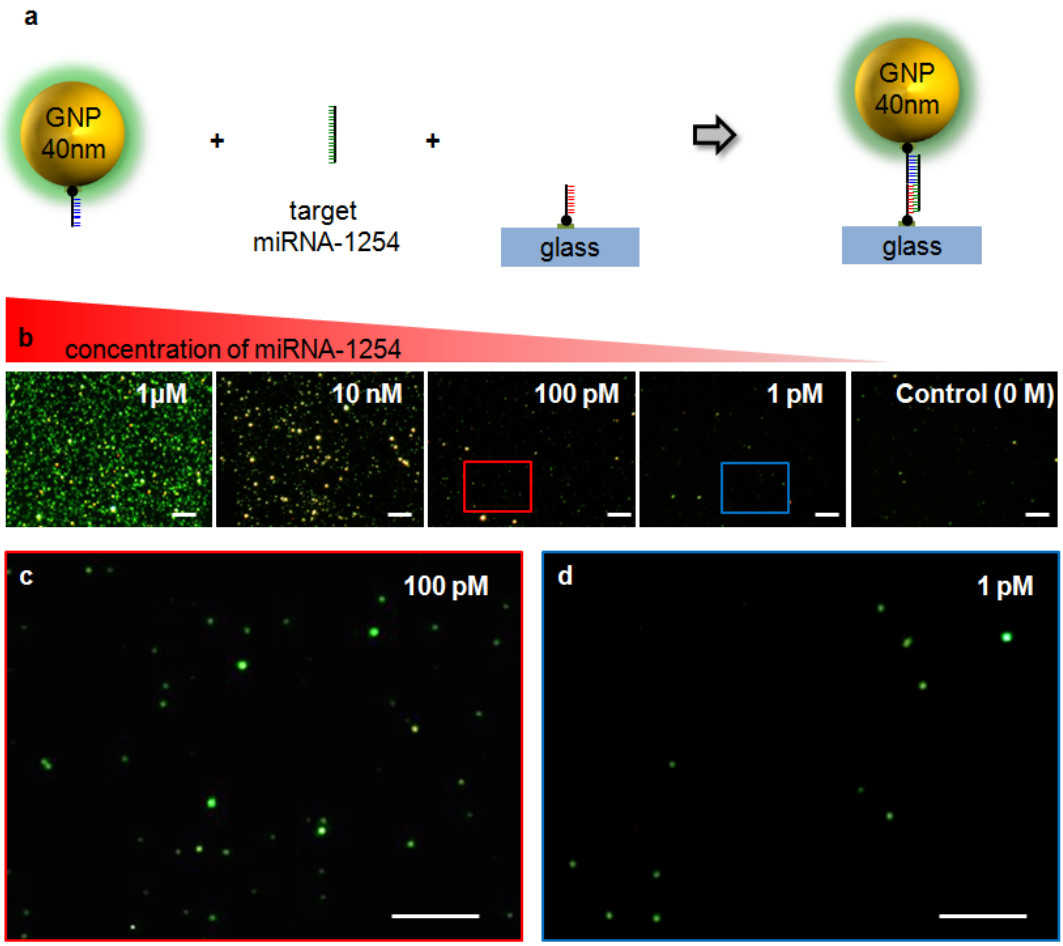

Figure 4.2. a, A schematic drawing of DNA-conjugated GNPs / miRNA-1254 hybridization on a glass slide. **b,** The dark-field scattering images of GNPs tethered on the glass substrate in the presence of a concentration gradient of target miRNA-1254. **c** and **d,** The enlarged views of the area outlined in red and blue respectively. Scale bars, 10 μm.

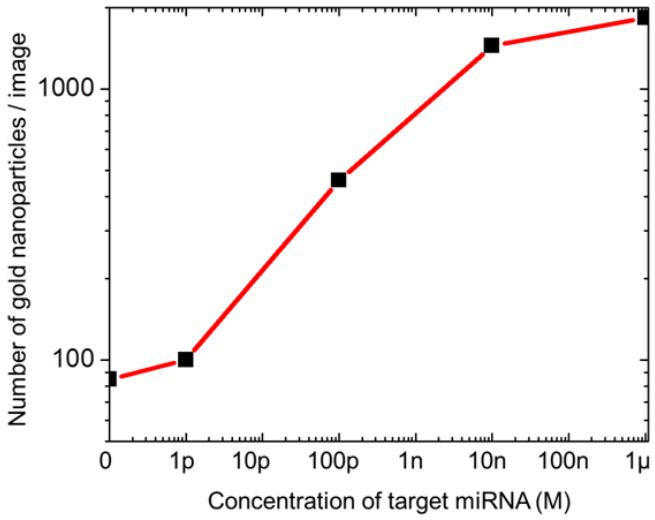

Figure 4.3. A plot of the density of captured GNPs versus miRNA concentration. The data indicated the ability to detect miRNA at a concentration range of 1μM to 1 pM.

4.3 Single-miRNA Detection Based on GNP-GNP Dimer Formation

Another miRNA detection scheme was developed based on the formation of GNP-GNP dimer (Fig. 4.1c).[9,26,27] GNPs were functionalized with streptavidin molecules, which were linked to a single stranded DNA probes labeled with biotin (Fig. 4.4a and 4.4b shown in blue). Another single stranded DNA probes were conjugated to the GNPs immobilized on the glass slides. The hybridization of the target miRNA to both single stranded DNA probes brings two GNPs in close proximity and causes a red shift in the scattering. In the negative control (without target miRNA-1254), about 91% of the GPN particles were monomeric indicating by the green scattering. About ~9% of GNPs formed dimer through non-specific binding as shown by the orange color (Fig. 4.4 a and 4.4c). When adding target miRNA-1254, the population of orange spots (indicated by the arrows in Fig. 4.4b) increased up to 39% (Fig. 4.4d), suggesting the desired formation of GNP/miRNA-1254/GNP complexes. The target miRNA mediated sandwich hybridization between two probes conjugated to GNPs and induced surface Plasmon resonance effect.

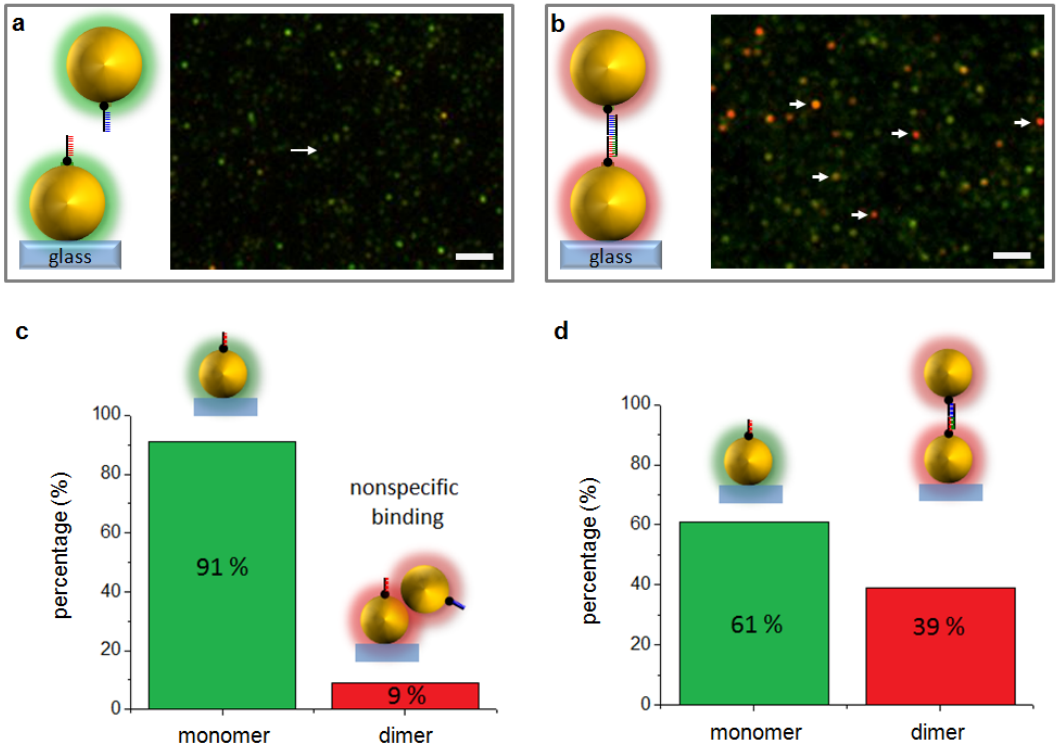

Fig. 4.4. Detecting miRNA-1254 by GNP-GNP dimer formation. a, Left, a schematic drawing of single GNPs in the absence of target miRNA. Right, the corresponding dark-field image of single GNPs. b, Left, a schematic drawing of a GNP-GNP dimer in the presence of target miRNAs. Right, the corresponding dark-filed image of GNPs, including dimers and momoners. The arrows in a and b indicate the position of the dimers. c, The percentage of monomers and dimers without target miRNA. d, The percentage of monomers and dimers in the presence of target miRNAs. Scale bars, 10 μm.

4.4 Total Internal Reflection Chips for Portable miRNA Detection

We built a miniaturized total internal reflection plasmonic microscopy (TIRPM) for point-of-care miRNA diagnosis chips.[15-17,19] The TIRPM system was designed for sensitive detection of light scattering of GNPs resulting from miRNAs binding (Fig. 4.1 b and 4.1c) in a hand-hold-size device. A total internal reflection was used to generate the evanescent wave for illuminating plasmonic nanoparticles (Fig. 4.5a and 4.5b). It consists of a fiber LED white light source equipped with a collimator, a moldable PDMS prism, a standard glass slide with or without microfluidic chambers (Fig. 4.5c and 4.5d). The coupling of fiber-guided photons to the surface plasmons and to the readout scattering signals was achieved through a prism-glass-sample multilayer. The optical path starts with a broadband warm white LED source, positioned at the right angle to the PDMS prism. The traveling waves are formed inside the prism-glass at carefully chosen refraction angles (θ_{prism} and θ_{inc}), related to the refractive

indices of the materials (n_{PDMS}, n_{glass} and n_{sample}) through the successive applications of Snell's Law. A simple calculation gives a critical angle $\theta_C = 61°$, $\theta_{prism} = 75°$ and $\theta_{inc} = 68°$, based on $n_{PDMS} = 1.46$, $n_{glass} = 1.52, n_{water} = 1.33$. Note that the sample is assumed to be in the water. An attenuated total reflection occurs if the incident angle θ_{inc} is larger than the critical angle θ_C. An evanescent wave is generated and attenuated in the interface exponentially. Inside the sample area, the evanescent decaying field $E(z)$ has an intensity $I(z) = |E(z)|^2$ given by $I(z) = I_0 e^{-z/\delta}$. Where δ is the evanescent penetration length (the length when the intensity is dropped by a factor of $1/e$) and I_0 is the peak intensity. The length of evanescence is calculated as short as $\delta \sim$ 99nm in our design. The intensity at the glass-sample interface $I_0 = I(0)$ is related to the Fresnel reflection and transmission coefficients for light polarization s (perpendicular to the plane of incidence) and p (parallel to the plane of incidence).

As related to the GNP sensing probe, the evanescent near-field is then converted to the scattered propagative fields through scattering events by GNP-field coupling. Plasmonic nanoparticles function as light collecting antennae, which enhance the near-fields and modify the far-field scattering signals. Fig. 4.6a shows a large field-of-view of a GNP-scattering image obtained by our TIRPM system. A large and uniform excitation field was generated on the glass-sample interface. The green dots indicated that the scattering signals resulted from single GNPs instead of GNP aggregates. An enlarged view of the scattering image demonstrated high S/N of single GNPs detection (Fig. 4.6b).

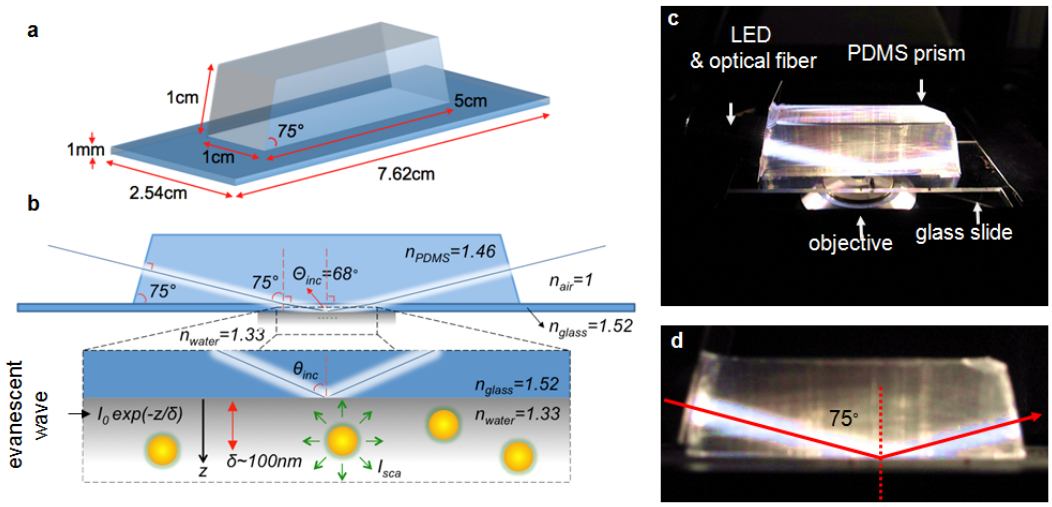

Figure 4.5. a, The overall design of TIRPM chip to create an evanescent wave to excite GNPs. **b,** The calculations based on the reflective index of the materials of the actual device in creating an evanescent wave. **c,** A photograph of the actual device at an angled view. **d,** A sideview of the TIRP device indicates that the angle between the incident LED light beam and the glass slide is ~75° .

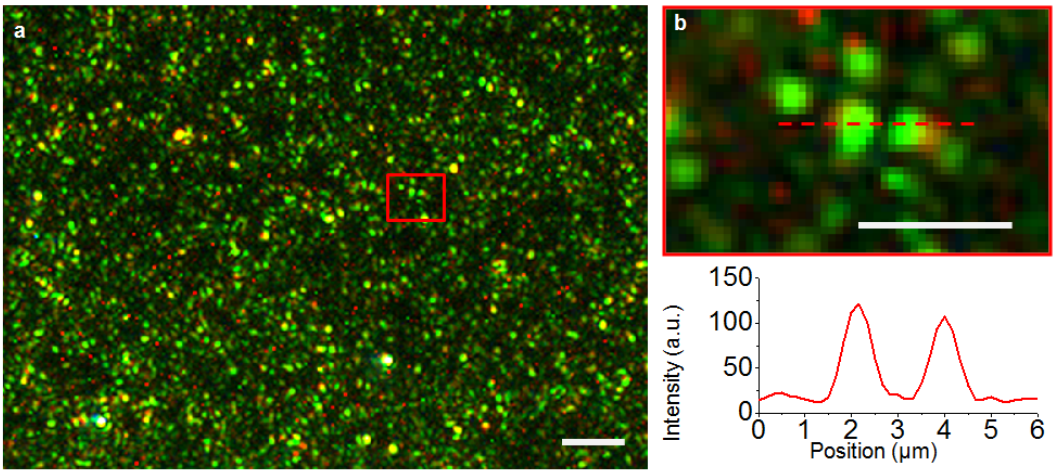

Figure 4.6 a, A wide-field scattering image of GNPs excited by the total internal reflection system. **b,** An enlarged view of the area outlined in (a), together with the intensity profile along the dash line (bottom). Scale bars in (a) and (b) are 10μm and 5 μm, respectively.

4.5 Conclusion and Outlook

In summary, our approach could detect miRNAs at 1μM to 1 pM concentration, which covers the majority of the concentration range present in the clinical specimens (ranging from 100pM to 10fM). In order to further improve the dynamic range of the detection to cover the whole clinical relevant concentrations and reduce false negative diagnosis, we are working to minimize the non-specific binding of GNPs to the subtract surface by coating the surface with proteins or polymers. Furthermore, besides the application in point-of-care portable device, GNP-medicated detection could be used in the laboratory as an alternative to PCR and microarray based detection. Our study demonstrated that the scattered signal from single GNPs is at five orders of magnitude higher than the fluorescence signals.[10] In addition, inexpensive low numerical aperture objective lens and low cost sensors could detect the scattering profile of GNP. The sensitivity of the detection further enhanced in the design where the hybridization with target-miRNAs induces GNP-GNP dimer formation and results in significant color change as a sensitive readout. Therefore, the GNP-medicated detection provides robust and rapid one-step detection and reduces the cost significantly comparing to traditional PCR and microarray based methods.

In terms of fabrication, using PDMS as an integrated optical component has a great advantage in integrating with micro- and nanofluidics technologies.[28-30] A chip with fluidic channels can be bonded to cover the sample area, which allows confining fluid and achieving spatial and temporal controls of local viscoelastic or thermal property. The short penetration of evanescence energy (~100nm) is suitable for nanofluidics integration. The fluidity of the sample near the glass-sample surface allows dynamic and rapid tuning of the refractive index. The nanoscale confinement of the optical energy and the fluid volume not only reduces reagent waste but also allows for nanoplasmonics functioning on chip. Last but not least, using fan-out optical fibers or patterned fluidic channels, a parallel multiplexed readout can be devised based on our system.

On the specimen side of the glass substrate, PDMS could also be used to create the fluidic channels by standard soft-lithography. For the future optical design, the overall size of our TIRPM device is expected to be smaller. A SU-8 or a Si wafer master will be used to mold the PDMS into geometries that yield optical functions. Overall, a significant enhancement of scattering intensity, together with the high throughput and portable imaging readout with lab-on-chip technology make the GNP-medicated detection a promising low-cost platform for ultrasensitive and ultrafast cancer diagnosis on a chip.[3,4,30]

Methods

Preparation of DNA-conjugated GNPs stock solution. 10 μL of streptavidin-coated GNP stock solution (~ 0.6 nM in water, SPR peak at ~530 nm; Sigma) was resuspended in 80 μL of T50 buffer (10mM Tris-HCl, 50mM NaCl, pH 8.0) and then mixed with 10μL of biotin-labelled probe DNA stock solution (10μM, sequence: 5- biotin-AAA AAA CTG CAG GCT CC -3). The binding between streptavidin and biotin was achieved by mixing them together at room temperature for 10 min. The solution of BSA (900μL, 0.5mg/ml) was added to the sample to prevent non-specific binding and aggregation in the stock. After centrifugation at 5000 rpm for 10 min (206D; Deville), the pellet was transferred and resuspended in T50 buffer to a final concentration of GNPs ~ 60pM.

Preparation of DNA-conjugated glass slides with or without GNPs pre-coating. For single GNP-based detection, standard glass slides (75 x 25 x1 mm, VWR) were cleaned by immersing them in a concentrated H_2SO_4-HNO_3 (vol/vol, 3:1) solution for 20 min, followed by extensive rinse with deionized water. The solution of biotin-labeled BSA (1 mg/ml, Sigma) in T50 buffer was then dropped on clean glass slides with PDMS chambers. After incubating at room temperature for 15 min, the unbound molecules were removed by washing with T50 buffer. Neutravidin solution (0.2 mg/ml) was introduced into the chambers and incubated for 5 min. To remove excess neutravidin, the chambers were washed with T50 buffer. Finally, 50μL of DNA probe solution (100 nM in T50 buffer with 0.5mg/ml BSA, sequence: 5- AGCTTC CAG GCT AAA AA- biotin-3) were added to the chambers and incubated for 5 min, followed by extensive rinsing with T50 buffer. This protocol allows stepwise coating of single layer of molecules to immobilizing DNA. For GNP-GNP dimer experiments, the surface was treated following the same protocols instead of replacing neutravidin molecules by streptavidin-coated GNPs (~ 60pM in T50 buffer).

Detection of miRNA-1254. 10 μL single-stranded miRNA-1254 mimic DNA molecules (5-AGC CTG GAA GCT GGA GCCTGC AGT -3) were dissolved in 80 μL T50 buffer and mixed with 10 μL DNA-conjugated GNPs stock solution to final concentrations of 1 μM – 1pM. After mixing at room temperature for 10 min, the samples were added to the DNA-conjugated glass slides with or without GNPs pre-coating to make the hybridization. Note that glass slides with and without pre-coated GNPs were used for dimer- and single- GNP based detection, respectively. After incubation for 15 min, free oligonucleotides and GNPs were removed by washing with T50 buffer.

Darkfield imaging of single and dimer GNPs. Our microscopy system is based on an inverted microscope (Carl Zeiss Axiovert 200). Excitation of the sample was made through a water-immersion darkfield condenser (Zeiss) by using a white light illumination (a 100W halogen lamp). The scattering images of GNPs were collected and recorded by a 40X objective lens (Zeiss) with a true-color digital camera (CoolSNAP cf; Roper Scientific, NJ).

Total internal reflection plasmonic microscopy. The prism was made by PDMS in a glass mold with well-defined angle. The PDMS prism was then attached to a standard glass slide (75 x 25 x1 mm, VWR). The glass plate coated with GNPs was mounted on a modified darkfield microscopy (Carl Zeiss Axiovert 200) for inspection. Excitation of the sample was made through a fiber LED white light source equipped with a collimator (Thorlabs). The scattering images of GNPs were collected and recorded by a 40X objective lens (Zeiss) with a true-color digital camera (CoolSNAP cf; Roper Scientific, NJ).

References

1. Mitchell, P.S., *et al.* Circulating microRNAs as stable blood-based markers for cancer detection. *Proc Natl Acad Sci U S A* **105**, 10513-10518 (2008).

2. Pritchard, C.C., Cheng, H.H. & Tewari, M. MicroRNA profiling: approaches and considerations. *Nature reviews. Genetics* **13**, 358-369 (2012).

3. Garzon, R., Marcucci, G. & Croce, C.M. Targeting microRNAs in cancer: rationale, strategies and challenges. *Nature reviews. Drug discovery* **9**, 775-789 (2010).

4. Schwarzenbach, H., Hoon, D.S. & Pantel, K. Cell-free nucleic acids as biomarkers in cancer patients. *Nature reviews. Cancer* **11**, 426-437 (2011).

5. Zhang, J., Zhao, H.D., Gao, Y. & Zhang, W. Secretory miRNAs as novel cancer biomarkers. *Biochim. Biophys. Acta-Rev. Cancer* **1826**, 32-43 (2012).

6. van't Veer, L.J., *et al.* Gene expression profiling predicts clinical outcome of breast cancer. *Nature* **415**, 530-536 (2002).

7. Lujambio, A. & Lowe, S.W. The microcosmos of cancer. *Nature* **482**, 347-355 (2012).

8. Zheng, D., Seferos, D.S., Giljohann, D.A., Patel, P.C. & Mirkin, C.A. Aptamer nano-flares for molecular detection in living cells. *Nano letters* **9**, 3258-3261 (2009).

9. Busson, M.P., *et al.* Optical and topological characterization of gold nanoparticle dimers linked by a single DNA double strand. *Nano letters* **11**, 5060-5065 (2011).

10. Saha, K., Agasti, S.S., Kim, C., Li, X. & Rotello, V.M. Gold nanoparticles in chemical and biological sensing. *Chemical reviews* **112**, 2739-2779 (2012).

11. de Planell-Saguer, M. & Rodicio, M.C. Analytical aspects of microRNA in diagnostics: a review. *Analytica chimica acta* **699**, 134-152 (2011).

12. Prigodich, A.E., *et al.* Multiplexed nanoflares: mRNA detection in live cells. *Analytical chemistry* **84**, 2062-2066 (2012).

13. Hurst, S.J., Lytton-Jean, A.K. & Mirkin, C.A. Maximizing DNA loading on a range of gold nanoparticle sizes. *Analytical chemistry* **78**, 8313-8318 (2006).

14. Xing, H., *et al.* DNA-directed assembly of asymmetric nanoclusters using Janus nanoparticles. *ACS nano* **6**, 802-809 (2012).

15. Axelrod, D. Total internal reflection fluorescence microscopy in cell biology. *Traffic* **2**, 764-774 (2001).

16. Moerner, W.E. & Fromm, D.P. Methods of single-molecule fluorescence spectroscopy

and microscopy. *Rev. Sci. Instrum.* **74**, 3597-3619 (2003).

17. Betzig, E., *et al.* Imaging intracellular fluorescent proteins at nanometer resolution. *Science* **313**, 1642-1645 (2006).

18. Li, G.W. & Xie, X.S. Central dogma at the single-molecule level in living cells. *Nature* **475**, 308-315 (2011).

19. Michalet, X., Weiss, S. & Jager, M. Single-molecule fluorescence studies of protein folding and conformational dynamics. *Chemical reviews* **106**, 1785-1813 (2006).

20. Shav-Tal, Y., *et al.* Dynamics of single mRNPs in nuclei of living cells. *Science* **304**, 1797-1800 (2004).

21. Bratu, D.P., Cha, B.J., Mhlanga, M.M., Kramer, F.R. & Tyagi, S. Visualizing the distribution and transport of mRNAs in living cells. *Proceedings of the National Academy of Sciences of the United States of America* **100**, 13308-13313 (2003).

22. Tyagi, S. Imaging intracellular RNA distribution and dynamics in living cells. *Nat. Methods* **6**, 331-338 (2009).

23. Raj, A., van den Bogaard, P., Rifkin, S.A., van Oudenaarden, A. & Tyagi, S. Imaging individual mRNA molecules using multiple singly labeled probes. *Nat. Methods* **5**, 877-879 (2008).

24. Itzkovitz, S. & van Oudenaarden, A. Validating transcripts with probes and imaging technology. *Nat. Methods* **8**, S12-S19 (2011).

25. Foss, K.M., *et al.* miR-1254 and miR-574-5p Serum-Based microRNA Biomarkers for Early-Stage Non-small Cell Lung Cancer. *J. Thorac. Oncol.* **6**, 482-488 (2011).

26. Chen, J.I., Chen, Y. & Ginger, D.S. Plasmonic nanoparticle dimers for optical sensing of DNA in complex media. *Journal of the American Chemical Society* **132**, 9600-9601 (2010).

27. Chen, J.I., Durkee, H., Traxler, B. & Ginger, D.S. Optical detection of protein in complex media with plasmonic nanoparticle dimers. *Small* **7**, 1993-1997 (2011).

28. Eftekhari, F., *et al.* Nanoholes As Nanochannels: Flow-through Plasmonic Sensing. *Analytical Chemistry* **81**, 4308-4311 (2009).

29. Oh, Y.J., *et al.* Beyond the SERS: Raman Enhancement of Small Molecules Using Nanofluidic Channels with Localized Surface Plasmon Resonance. *Small* **7**, 184-188 (2011).

30. Liu, G.L. & Lee, L.P. Nanowell surface enhanced Raman scattering arrays fabricated by soft-lithography for label-free biomolecular detections in integrated microfluidics.

Applied Physics Letters **87**(2005).

CHAPTER 5

Future Work and Conclusions

5.1 Introduction

In the end of this thesis, I conclude with the outlook of *in vivo* nanoplasmonic manipulation of genetic circuits and nanoplasmonic integrated nanofluidics for medical diagnostics. Applications of multiple plasmonic nanomaterial-controlled deliveries are promising for reconstruction of gene circuit in live cells.[1,2] Through inspirations from optogenetics,[3-10] nanoplasmonic gene regulation mediated by photothermal effects might provide multiple manipulations with high spatial and temporal resolution. Studying nanoplasmonic-mediated sensing and gene regulation could provide new avenues for understanding how biological systems function at the molecular level. On the other hand, nanoplasmonic integrated nanofluidic devices are potential platforms for the precise control of nano-scaled environments and high throughput analysis.[11-17] As relevant to DNA sequencing and analysis, plasmonic antenna-integrated nanopore devices that creatively utilize the unique plasmonic enhanced optical trapping could bring new ways to refine molecular transport in nanoscale.

5.2 Multiplex Gene Manipulation by Tunable Optical Antennae

Researchers have long been fascinated by remotely and non- invasively switching genes on and off.[3,5-10] Flexible manipulation of genetic circuits has been studied using Escherichia coli and bacteria based on genetically encoded light sensors.[3,7] Recently, there has been a resurgence of interest in leveraging light for gene regulation from bacteria to animals.[6,9] Genetic modifications are finding increased utility as multichromatic control of gene expression. The concept of multichromatic control of gene circuits is that different combinations of irradiation (i.e. shining different color of light) could result in different patterns of gene expression with high temporal resolution.[7]

However, one concern with respect to optogenetic methods is that making genetic-modified animals or cells is sophisticated and might cause cancer formation. This limits the scope of their applications. Our study demonstrated that nanoplasmonic-mediated transfection is capable of control gene expression by light-induced siRNA delivery. Such safety and flexibility hold a number of advantages over traditional optogenetic methods.[1,2] Without gene modification, it is possible to perform deconstruction of genetic circuits by spatial and temporal control of multiple deliveries of genetic materials. For further studies on genetic circuits, nanoplasmonic-mediated gene regulation makes it possible to expend target genes or pathways to more than three by addressing different vectors (i.e. gold nanorods with various absorption peaks).[1,2,4,18,19] In addition, gold nanoparticles can be multi-function materials (e.g. acting as vectors and probes, simultaneously). The long-range photothermal triggering, together with noncytotoxicity and easiness of surface functionalization, makes nano-sized plasmonic antennae promising vectors for tissue-specific gene regulation and potential probes for real-time monitoring the responses as

well.

5.3 Light-modulated Molecular transport by Nanoplasmonic Antennae-integrated Nanopores

In nanopore-based DNA sequencing and analysis, one of current challenges is to improve the sensitivity and resolution by controlling DNA translocation velocity.[14,17] The ideal velocity range is 1 to 100 nt/ms (Fig. 5.1a).[17] Biological nanopores (red dots) have demonstrated that they can control the velocities below this range via biomolecule-DNA interactions. However, biological nanopores are not stable in general, compared with solidstate ones. To improve the sensitivity of solidstate nanopores, researchers are seeking new device architectures or methods to slow down DNA translocation.[17]

In addition to the plasmonic-enhanced fluorescent ability, there is another key aspect of our nanopore devices. It is that DNA translocation velocity should be able to slow down by localized plasmonic trapping of integrated antennae (Fig. 5.1b).[15,16,20,21] Such unique capabilities will be tested by monitoring of single DNA translocation events. Under antennae-mediated plasmonic trapping, the speed of DNA translocation should be slower than 100 nt/ms. Note that the best recorded in solid-state nanopore is ~400 nt/ms (Fig. 5.1a).[16] To further demonstrate the uniqueness of our integrated optical antenna, we will investigate modulation of the translocation velocity by tuning the level of plasmonic trapping effect. We will use the 488-nm laser (matched well with the surface plasmon resonance of our gold antennas) to modulate plasmonic trapping by switching the laser on and off. The dye-labeled DNA molecules will be excited by the other 561-nm laser. With this dual laser setup, we should be able to observe optical modulation of DNA translocation.[16] This experimental design will clearly demonstrate that optical trapping is enhanced when the nanoantenna is in plasmon resonance.

Although the fields of plasmonics and nanopore-fluidics have developed independently, some forms of convergence have been observed recently. Indeed, in plasmonic nanofluidic systems, metallic nanostructures are promising candidates for the achievement of seamless integration of subwavelength miniaturization of biophotonic manipulation and detection functions, whereas nanofluidic control at the small scale seeks to automate and optimize biochemical and biomedical analyses. Such capabilities open up future opportunities to slow-down the translocation events to enable a single nucleotide level detection.[17]

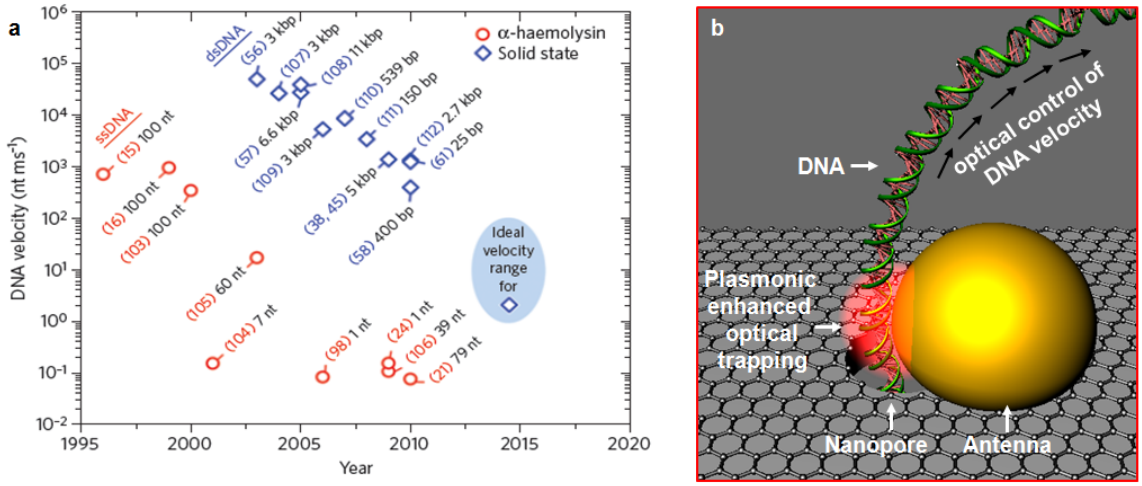

Figure 5.1 a, Development of DNA translocation velocity on nanopore techniques.[17] Note that the ideal velocity range is labeled by the blue area (in the range 1–100 nt / ms). **b**, Modulation of DNA translocation velocity by plasmonic optical trapping.

References

1. Anikeeva, P. & Deisseroth, K. Photothermal genetic engineering. *ACS nano* **6**, 7548-7552 (2012).

2. Lee, S.E., *et al.* Photonic Gene Circuits by Optically Addressable siRNA-Au Nanoantennas. *ACS Nano* **6**, 7770-7780 (2012).

3. Levskaya, A., *et al.* Engineering Escherichia coli to see light - These smart bacteria 'photograph' a light pattern as a high-definition chemical image. *Nature* **438**, 441-442 (2005).

4. Braun, G.B., *et al.* Laser-Activated Gene Silencing via Gold Nanoshell-siRNA Conjugates. *ACS Nano* **3**, 2007-2015 (2009).

5. Levskaya, A., Weiner, O.D., Lim, W.A. & Voigt, C.A. Spatiotemporal control of cell signalling using a light-switchable protein interaction. *Nature* **461**, 997-1001 (2009).

6. Jenkins, M.W., *et al.* Optical pacing of the embryonic heart. *Nature Photonics* **4**, 623-626 (2010).

7. Camsund, D., Lindblad, P. & Jaramillo, A. Genetically engineered light sensors for control of bacterial gene expression. *Biotechnology Journal* **6**, 826-836 (2011).

8. Tabor, J.J., Levskaya, A. & Voigt, C.A. Multichromatic Control of Gene Expression in Escherichia coli. *Journal of Molecular Biology* **405**, 315-324 (2011).

9. Yanik, M.F., Rohde, C.B. & Pardo-Martin, C. Technologies for Micromanipulating, Imaging, and Phenotyping Small Invertebrates and Vertebrates. in *Annual Review of Biomedical Engineering, Vol 13*, Vol. 13 (eds. Yarmush, M.L., Duncan, J.S. & Gray, M.L.) 185-217 (2011).

10. Yizhar, O., Fenno, L.E., Davidson, T.J., Mogri, M. & Deisseroth, K. Optogenetics in Neural Systems. *Neuron* **71**, 9-34 (2011).

11. Eftekhari, F., *et al.* Nanoholes As Nanochannels: Flow-through Plasmonic Sensing. *Analytical Chemistry* **81**, 4308-4311 (2009).

12. Kang, T., Hong, S., Choi, Y. & Lee, L.P. The Effect of Thermal Gradients in SERS Spectroscopy. *Small* **6**, 2649-2652 (2010).

13. Oh, Y.J., *et al.* Beyond the SERS: Raman Enhancement of Small Molecules Using Nanofluidic Channels with Localized Surface Plasmon Resonance. *Small* **7**, 184-188 (2011).

14. Branton, D., *et al.* The potential and challenges of nanopore sequencing. *Nature Biotechnology* **26**, 1146-1153 (2008).

15. Juan, M.L., Righini, M. & Quidant, R. Plasmon nano-optical tweezers. *Nature Photonics* **5**, 349-356 (2011).

16. Pang, Y.J. & Gordon, R. Optical Trapping of a Single Protein. *Nano Letters* **12**, 402-406 (2012).

17. Venkatesan, B.M. & Bashir, R. Nanopore sensors for nucleic acid analysis. *Nature Nanotechnology* **6**, 615-624 (2011).

18. Svoboda, K. & Yasuda, R. Principles of two-photon excitation microscopy and its applications to neuroscience. *Neuron* **50**, 823-839 (2006).

19. Melancon, M.P., Zhou, M. & Li, C. Cancer Theranostics with Near-Infrared Light-Activatable Multimodal Nanoparticles. *Accounts of Chemical Research* **44**, 947-956 (2011).

20. Grigorenko, A.N., Roberts, N.W., Dickinson, M.R. & Zhang, Y. Nanometric optical tweezers based on nanostructured substrates. *Nature Photonics* **2**, 365-370 (2008).

21. Righini, M., *et al.* Nano-optical Trapping of Rayleigh Particles and Escherichia coli Bacteria with Resonant Optical Antennas. *Nano Letters* **9**, 3387-3391 (2009).